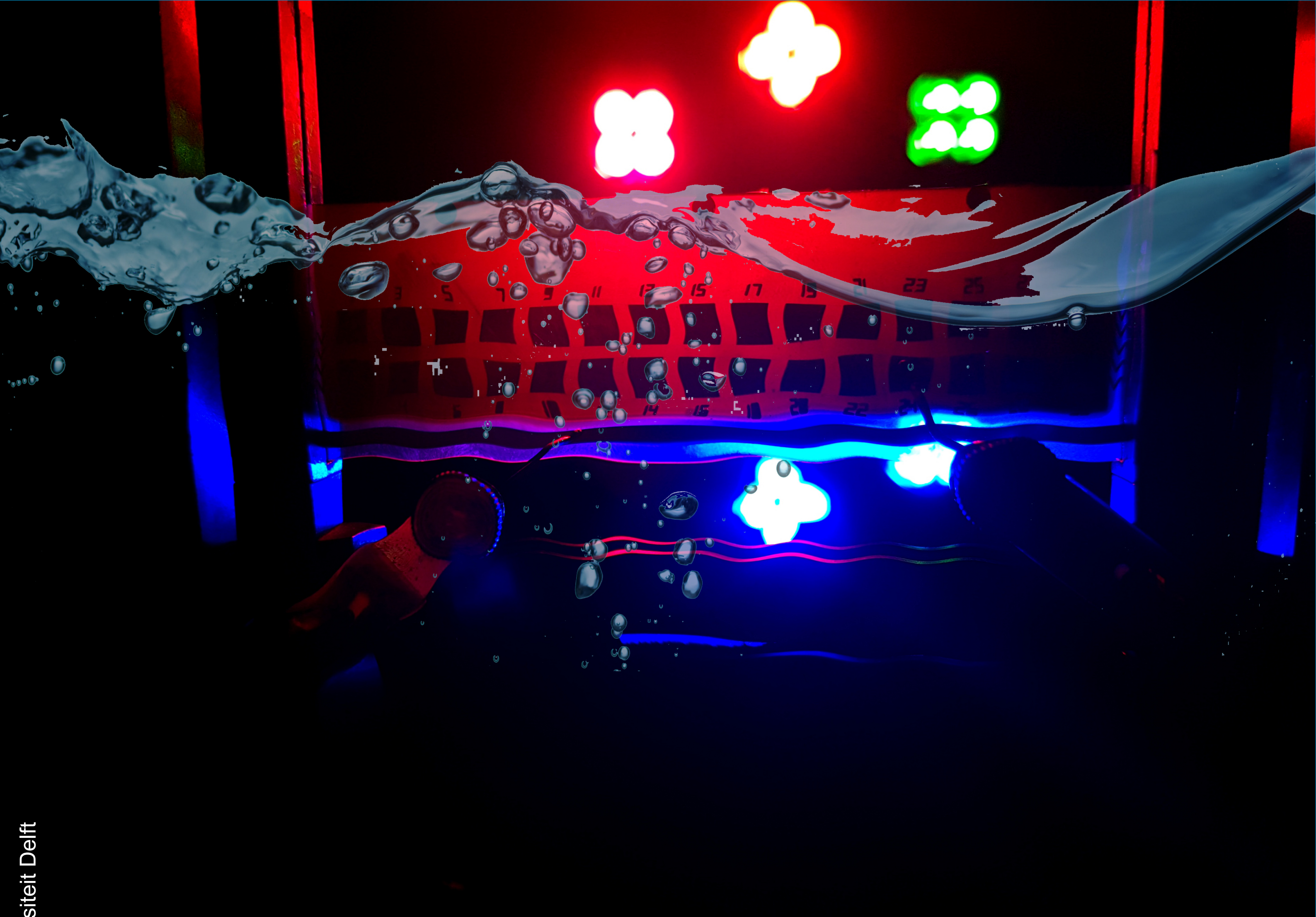

Technische Universiteit Delft

Thin-film silicon triple junction solar cell for solar fuels

V. C. S. Hamoen

TU Delft

Thin-film silicon triple junction solar cell for solar fuels

by

V. C. S. Hamoen

to obtain the degree of Master of Science
at the Delft University of Technology,
to be defended publicly on Thursday December 21, 2017 at 14:00.

Student number:	4052692	
Project duration:	February 1, 2017 – December 21, 2017	
Thesis committee:	Prof. Dr. Arno. H. M. Smets,	Supervisor, PVMD
	Ir. Paula Perez Rodriguez	Daily supervisor, PVMD
	Dr. Olindo Isabella,	PVMD
	Dr. Mohamad Ghaffarian Niasar	ESE

An electronic version of this thesis is available at http://repository.tudelft.nl/.

TU Delft

Preface

I have chosen the Sustainable Energy Technologies Master's programme because of the wide scope regarding renewable energy sources as well as the possibility to go in-depth into one of them. I chose to pursue a thesis project in solar energy at the Photovoltaic Materials and Devices (PVMD) group, because I find the technology is very elegant and interesting. Additionally, I firmly believe that solar energy is key towards a sustainable future powered by clean energy.

During this thesis project I've had the opportunity and pleasure to work with great facilities and even better people. I would like to thank Prof. Arno Smets for granting me the opportunity to join the PVMD group and for his contagious optimism and motivation. I would also like to thank Paula Perez Rodriguez, as my daily supervisor, for her instructions, her patience, our discussions and to keep me focused on the bigger picture.

Furthermore, I would like to thank our technicians, Stefaan Heirman and Martijn Tijssen, for their willingness to share their expertise and for their time and effort to keep all the equipment up to spec.

Then I would like to thank the rest of the staff of the PVMD group. In particular Paul Procel Moya for helping me get a better understanding of the workings of tunnel recombination junctions and greatly assisting me for simulating the band diagrams for the triple junction device; I now also make mental pictures of band diagrams and waving my hands in the air; Fai Tong Si for helping me get started with the amorphous silicon germanium material, Engin Özkol for adjusting his own time management for experiments, so that I could be more efficient with mine. And I would like to thank Johan Blanker for his instructions, discussions and feedback and for the company in the weekend experiments and measurements.

Not just the staff have been an inspiration and help to me. I am also thankful for my fellow Master's students who have provides useful discussions as well as welcome distractions. Among which are, Aditya Chaudhary, Yvar de Groot, Guillaume d'Hérouville, Camilla Massacesi and Simone Regondi.

I would also like to thank my family and friends that have made me who I am today and that have had to listen to me give an in-depth explanation of my work during this thesis. Special thanks go out to my girlfriend, who was, and is always there for me, even when I was not, like during the final part of my thesis. Lastly, I would like to thank my son for giving me the perspective of what matters in life. I hope this work contributes to making a brighter future for you and your sibling.

V. C. S. Hamoen
Delft, December 2017

Abstract

The ever increasing installed capacity of renewable, sustainable energy is essential in order to keep the earth habitable. However, the intermittent nature of solar and wind energy do not strictly follow human energy demands. Therefore an energy of sufficient magnitude buffer is essential to provide a constant supply of energy that matches the demand as closely as possible. Chemical energy shows high potential in terms of clean, long-term energy storage with efficient conversion to electricity.

The DEMO project intends on manufacturing a monolithic photovoltaic device for the production of hydrogen gas and hydrocarbon products by the electrochemical splitting of water and carbon dioxide. an a-Si:H/a-SiGe:H/nc-Si:H triple junction device is proposed to generate a combination of voltage and current to drive the electrochemical reactions efficiently, while simultaneously addressing scalability by using earth-abundant materials.

In this thesis, efforts were made to optimise the a-SiGe:H subcell as well as finding the optimal combination of materials to use as tunnel recombination junctions as intermediate layers between subcells of the multi-junction device.

The best performing a-SiGe:H p-i-n single-junction device achieved a V_{OC}= 719 mV, J_{SC}=17.2 mA/cm^2, FF = 0.63 and η = 7.85% as processed on an Asahi VU superstrate. This performance was observed show a strong decline with increasing intrinsic layer thickness and increasing deposition rate. Although a conclusive optimal device structure was not obtained, it is believed that bandgap profiling by adjusting the germanium content in the intrinsic layer as well as applying buffer layers can substantially improve the performance of the a-SiGe:H single-junction solar cell.

To assess long-term stability, an a-SiGe:H single-junction device was subdued to 1000h light soaking. Meta-stable defects induced by recombination of photo-generated charge carriers resulted is a strong degradation in FF of 20% relative. V_{OC} and J_{SC} showed similar relative decreases in performance with 9.0% and 8.6%, respectively. The resulting relative drop in conversion efficiency for the degraded solar cell is observed to be 34%.

The best tunnel recombination junction for an a-Si:H/a-SiGe:H double junction consists of a 5 nm highly doped n$^+$-type nc-SiO$_x$:H layer with a 2 nm nc-Si:H p-layer, placed between 25 nm nc-SiO$_x$:H n-layer and a 16 nm nc-SiO$_x$:H p-layer that resulted in good combination of FF, V_{OC} and J_{SC} by improved tunnelling, charge separation and better light management.

The best tunnel recombination junction for an a-SiGe:H/nc-Si:H double-junction consists of a highly doped n$^+$ nc-SiO$_x$:H layer with a 2 nm nc-Si:H p-layer. These layers are sandwiched between an 50 nm nc-SiO$_x$:H n-layer, of which the first half has linearly increasing oxygen content, and a 16 nm nc-SiO$_x$:H p-layer of the a-SiGe:H subcell and nc-Si:H subcell, respectively.

These tunnel recombination junctions were used to further develop a p-i-n a-Si:H/a-SiGe:H/nc-Si:H triple-junction solar cell on a wet-etched glass superstrate with ZnO:Al as both sacrificial layer for texturing and as transparent conductive oxide. The best performing triple-junction device achieved a V_{OC} = 1.96 V, J_{SC}= 6.21 mA/cm^2, FF = 0.63 and η = 7.63% with respective intrinsic layer thicknesses of 175 nm/120 nm/3000 nm. The conversion efficiency of this current mismatched device is throttled by the current limiting a-SiGe:H middle cell. Enhancing the a-SiGe:H material quality allows for thicker absorber layer to increase current generation without compromising the electrical performance, which can significantly improve the performance the triple-junction device.

This device is able to achieve an estimated solar-to-fuels efficiency of 4.9% for producing hydrogen with a high performance electrode and an an IrO$_x$ counter electrode. Assuming similar electrode performance, the solar-to-fuels efficiency for producing both hydrogen and methane is expected to be 2.4%. Hydrocarbons with higher electrochemical potential are not likely to be produced with such a device due to the higher electrochemical potentials.

Using the measured degraded performance of the a-SiGe:H subcell, a relative decrease in water splitting efficiency of 21% is expected for the triple-junction device.

Contents

Abstract v

List of Figures ix

List of Tables xi

1 Introduction 1

2 Theoretical Background 5
- 2.1 Solar Energy . . . 5
- 2.2 Semiconductor properties . . . 6
- 2.3 Recombination and other loss mechanisms. . . . 8
- 2.4 p-i-n junction . . . 9
- 2.5 Photovoltaic technologies. . . . 11
- 2.6 Multi-junction solar cells . . . 12
- 2.7 Optics . . . 14
- 2.8 Solar cell performance . . . 15
- 2.9 Long-term stability of solar cells . . . 16
- 2.10 Photoelectrochemistry . . . 17

3 Methodology 21
- 3.1 Processing techniques and equipment . . . 21
  - 3.1.1 Substrate preparation . . . 21
  - 3.1.2 Plasma enhanced chemical vapour deposition. . . . 22
  - 3.1.3 Sputtering . . . 23
  - 3.1.4 Thermal- and electron beam evaporation . . . 24
- 3.2 Characterization of solar cell performance . . . 24
  - 3.2.1 External quantum efficiency . . . 25
  - 3.2.2 $J-V$ curve measurement . . . 26
  - 3.2.3 Spectrometry . . . 26
  - 3.2.4 Spectroscopic ellipsometry . . . 27
  - 3.2.5 Light soaking. . . . 27

4 Results and Discussion 29
- 4.1 a-SiGe:H single-junction device. . . . 29
  - 4.1.1 a-SiGe:H intrinsic layer thickness . . . 30
  - 4.1.2 Buffer layers and grading. . . . 32
- 4.2 Light induced degradation . . . 34
- 4.3 Single-junction performance on an AZO superstrate . . . 36
- 4.4 Tandem devices. . . . 37
  - 4.4.1 a-Si:H/a-SiGe:H top tandem device . . . 38
  - 4.4.2 a-SiGe:H/nc-Si:H bottom tandem device . . . 41
- 4.5 Triple junction device . . . 44
  - 4.5.1 Solar-to-fuels efficiency . . . 48

5 Conclusion and recommendations 51
- 5.1 Conclusion . . . 51
- 5.2 Recommendations . . . 52

A P-type window layer 55

Bibliography 57

List of Figures

1.1 A typical Australian single home load profile (blue bars) with solar insolation (line) and the mismatch that is fed back into the grid (red bars) [3] 1
1.2 A double logarithmic plot of the energy density by weight (x-axis) and volume (y-axis) of various fuels or energy storage solutions [10] 2
1.3 A schematic of the device structure as proposed in the DEMO project. It incorporates a solar cell to directly produce high energy fuels from water and CO_2 [15] 3

2.1 The solar AM1.5 and AM0 spectra along with that of a ideal blackbody with T =6000 K according to Planck's law [17] 6
2.2 Energy band diagram of metals (left), semiconductors (middle) and insulators (right) 7
2.3 Doping of phosphorous or boron in a silicon lattice using the bonding model. An adaptation of [18] 8
2.4 Position of E_F as well as the introduction of energy states close to the band edges in n- and p-type semiconductors. An adaptation of [18] 8
2.5 The Shockley-Queisser limit for solar cells illuminated by the AM1.5 spectrum as function of bandgap [18] 10
2.6 A p-i-n junction for an a-Si:H solar cell with nc-SiO_x:H as p- and n-layers. An adaptation of [18] 10
2.7 From left to right: a monocrystalline, polycrystalline and thin-film silicon solar cell [21] 11
2.8 The phase transition from crystalline (left) to amorphous (right) [23] 12
2.9 Spectral utilisation of a single-junction solar cell (left) and a multi-junction solar cell which consists of three junctions with different bandgaps (right) [18] 12
2.10 A simulated energy band diagram of a TRJ in a p-i-n/p-i-n double-junction solar cell at equilibrium. The Fermi level is the reference at 0 eV 13
2.11 The J-V curve of a solar cell showing its MPP and corresponding J_{mpp} and V_{mpp} as well as its J_{SC} and V_{OC} 16
2.12 The electric equivalent circuit of a non-ideal solar cell in accordance to the two-diode model . . 16
2.13 The effect of R_s and R_{sh} on the $J-V$ curve and thus, FF [31] 17
2.14 The J-V characteristic of a water splitting IrO_x electrode 18

3.1 Surface morphology of the Asahi (left) and AZO (right) textured substrates as imaged by atomic force microscopy [39] 21
3.2 Defective filaments indicated with yellow arrows in nc-Si:H for textures with different rms roughness. All figures are at the same scale [48] 22
3.3 An illustration showing the working principle of PECVD (a) and sputtering (b) [51] 23
3.4 The Amigo PECVD cluster tool by Elettrorava S.p.A. with the control software running in front . 23
3.5 A schematic representation of a) thermal evaporation and b) e-beam evaporation [52] 24
3.6 The EQE set-up with its components as placed in an obscuring enclosure 25
3.7 The spectral output of the eight LED's used to allow the measurement of the spectral response of individual subcells in multi-junction solar cells 26
3.8 The Wacom solar simulator with visible light output. The inlay shows a front view of the measurement chuck used for the thin-film solar cell stripes with 30 individual dots 27
3.9 The LID set-up with mirrored wall. Left: Three samples are subdued to light soaking. Right: The six halogen lamps 28

4.1 A schematic bandgap profile (left) and the baseline structure (right) of the a-SiGe:H single-junction device 30
4.2 EQE and 1-R of a-SiGe:H SJs with increasing intrinsic layer thickness of 80-200 nm in 40 nm increments 31

4.3 a-SiGe:H SJ external parameters as function of intrinsic layer thickness. Different colors and markers indicate different batches. The given error bars are the standard error; Values for J_{SC} are based on a single EQE measurement . . . 32
4.4 The change in external parameters in time due to LID of an a-SiGe:H cell without (blue □) and with buffer layer (red ▷) . . . 34
4.5 $J-V$ curves of the a-SiGe:H solar cell with buffer layer after annealing and after 1000h of light soaking . . . 35
4.6 Schematic structure of the a-Si:H (left) and nc-Si:H (right) single-junction solar cells on an textured glass superstrate with AZO as TCO . . . 36
4.7 The EQE and 1-R of the a-Si:H, a-SiGe:H and nc-Si:H SJ devices on an AZO superstrate . . . 37
4.8 The $J-V$ curves of the a-Si:H, a-SiGe:H and nc-Si:H SJ devices on an AZO superstrate . . . 38
4.9 Schematic structure of the a-Si:H/a-SiGe:H top tandem device. The doped layers in between the intrinsic layers are indicated with TRJ and vary in structure . . . 38
4.10 An simulated energy band diagram of a TRJ in an a-Si:H/a-SiGe:H tandem device with high and lower doping levels. The Fermi level is the reference at 0 eV . . . 40
4.11 The EQE and 1-R graphs of a-Si:H/a-SiGe:H tandem solar cells with 50 nm nc-SiO_x:H n-layer (A+B), 25 nm nc-SiO_x:H n-layer (Thin n) and 50 nm nc-SiO_x:H n-layer plus and added 5 nm nc-SiO_x:H n^+-layer (n^+) . . . 41
4.12 The EQE's and 1-R of the a-Si:H/a-SiGe:H tandem solar with 15 nm, 25 nm and 35 nm as thickness of the nc-SiO_x:H n-layer . . . 42
4.13 Schematic structure of the a-SiGe:H/nc-Si:H bottom tandem device. The doped layers in between the intrinsic layers are indicated with TRJ and vary in structure . . . 43
4.14 The EQE and 1-R of the a-SiGe:H/nc-Si:H tandem device with n-type nc-Si:H and n^+-type nc-SiO_x:H as TRJ from the second batch . . . 44
4.15 Schematic structure of the most common used configuration of the a-Si:H/a-SiGe:H/nc-Si:H triple junction device . . . 45
4.16 Triple junction performance as function of absorber layer thickness. The default thickness of the a-Si:H, a-SiGe:H and nc-Si:H subcells are 200 nm, 120 nm, 3000 nm, respectively. The asterisk (*) denotes that a cell was processed in a different batch with respect to those in the same series. . . . 46
4.17 EQE of an a-Si:H/a-SiGe:H/nc-Si:H 3J device with intrinsic layer thicknesses of 200 nm/120 nm/3000 nm, respectively. . . . 47
4.18 The measured 1-R graphs of 3J devices with 50 nm, 100 nm and 125 nm n-type nc-SiO_x:H layer thickness . . . 48
4.19 EQE of an a-Si:H/a-SiGe:H/nc-Si:H 3J device on an Asahi VU superstrate with a p-type nc-Si:H intermediate reflective layer between the middle and bottom subcells . . . 49
4.20 The $J-V$ characteristics of the best three 3J devices and that of an IrO_x counter electrode for the hydrogen evolution reaction with- and without 0.1 V overpotential. The inlay gives a zoomed view of the operational points of the 3J devices . . . 50

A.1 The EQE of four different p-layer structures along with their respective 1-R . . . 56

List of Tables

4.1 The external parameters of a reference a-SiGe:H solar cells and one with an added 5 nm a-Si:H buffer at the p/i interface . . . 29

4.2 The external parameters of a-SiGe:H solar cells with different intrinsic layer thickness. The sample marked with * was processed in a separate batch. T . . . 31

4.3 External parameters of U-profiled a-SiGe:H single-junction solar cells with different thickness of graded layers, as well as different a-Si:H buffer layers at the p/i and i/n interfaces. The change in layer thickness relative to the reference is indicated in brackets. Dots are considered working with performance ≥75% of the average of the best 5 dots in terms of efficiency. Best values are highlighted with a bold typeface . . . 33

4.4 The absolute and relative drop in external parameters of two a-SiGe:H SJ solar cells after 1000 hours of light soaking . . . 35

4.5 The external parameters of the a-Si:H, a-SiGe:H and nc-Si:H SJ subcells on an AZO superstrate compared to SJs used in a similar structure with a 3J device efficiency of 16.1% . . . 36

4.6 The thicknesses of various layers used as TRJ in the a-Si:H/a-SiGe:H tandem device and their respective performance.
Unique variations are indicated with a bold typeface. . . . 39

4.7 The external parameters of a-Si:H/a-SiGe:H tandem devices with varying top cell n-type SiO_x:H layer and constant 5 nm n^+-type SiO_x:H layer as TRJ. This cell was processed in a different batch with a 200 nm, instead of 120 nm, intrinsic a-SiGe:H layer. . . . 40

4.8 The thicknesses of various layers used as TRJ in the a-SiGe:H/nc-Si:H tandem device and their performance. Two right-most solar cells were processed in a separate batch. Notable deviations in structure are indicated with a bold typeface as a guide to the eye . . . 43

4.9 The external parameters and current generated in each separate subcell for 3J devices with various reflective layers . . . 46

4.10 The external parameters, operational current density and solar-to-fuel efficiency of the best performing 3J devices including 0.1 V overpotential. The thickness of the a-Si:H subcell is indicated in brackets. The respective thickness of the a-SiGe:H and nc-Si:H intrinsic layers are 120 nm and 3μm for all samples . . . 49

A.1 The external parameters of an a-SiGe:H single-junction solar cell with different configuration of double p-layer. The top p-layer makes contact with the TCO and is kept at 4 nm thickness. The bottom p-layer is adjacent to the intrinsic layer and kept at 8 nm thickness. The letter in brackets denotes high (H) or low (L) bandgap . . . 55

Nomenclature

η	Conversion efficiency
η_{STF}	Solar-to-fuels efficiency
λ	Wavelength
Φ	Spectral photon flux
$\Phi_{ph,\lambda}^{\text{AM1.5}}$	Wavelength dependant spectral photon flux for the AM1.5 spectrum
σ	Standard deviation
A	Absorptance
c	Speed of light in a vacuum inertial frame
E^0	Electrochemical ponential
E_a	Activation energy
E_c	Conduction band edge energy
E_F	Fermi energy
E_g	Bandgap energy
E_v	Valence band edge energy
E_{ph}	Photon energy
F	Faraday constant
FF	Fill factor
G	Gibbs energy of formation
h	Planck constant
I	Electric current
I_d	Diode current
I_{ph}	Photocurrent
I_{ph}^{ref}	Reference photocurrent
J_0	Saturation current
J_{mpp}	Maximum power point current density
J_{SC}	Short circuit current
k_B	Boltzmann constant
L	Atmospheric path length
L_0	Atmospheric path length at normal incidence
mu_n/p	Electron/Hole mobility

n Electron concentration/Refractive index/ Diode ideality factor

n_e Stiochiometric coefficient of electrons

P Spectral power

p Hole concentration

P_{max} Maximum power density

q Elementary charge

R_s Series resistance

R_{sh} Shunt resistance

T Temperature/Transmittance

V_{OC} Open circuit voltage

V_{vmpp} Maximum power point voltage

3J Triple-junction

4J Quadruple-junction

a-Si:H Hydrogenated amorphous silicon

a-SiGe:H Hydrogenated amorphous silicon germanium

a-SiO$_x$:H Hydrogenated amorphous silicon oxide

AM Air mass

AZO Aluminium doped zinc oxide, ZnO:Al

c-Si crystalline silicon

d Thickness

EQE External quantum efficiency

EQE^{ref} Reference external quantum efficiency

eV Electron volt

FTO Fluorine doped tin oxide, SnO_2:F

i intrinsic

IPA Isopropylalcohol

IR Infrared

LED Light emitting diode

LID Light-induced degradation

LS Light soaking

MPP Maximum power point

n n-type

n$^+$ Highly doped n-type

nc-Si:H Hydrogenated nanocrystalline silicon

nc-SiO_x:H Hydrogenated nanocrystalline silicon oxide

p p-type

p^+ Highly doped p-type

PECVD Plasma enhanced chemical vapor deposition

RF Radio frequency

RHE Reversible hydrogen electrode

SE Spectroscopic Ellipsometry

SHJ Silicon heterojunction

SJ Single-junction

SQ Schockley-Queisser

SRH Schockley-Read-Hall

STC Standard test conditions

SW Staebler-Wronski

TCO Transparant conductive oxide

UV Ultra violet

VHF Very high frequency

vis Visible

z Angle of solar incidence relative to the surface normal

1

Introduction

Over the last centuries, the global energy need has shifted from luxury to necessity. As the number of applications has grown exponentially, so has the total energy demand. With the aid of compact, high energy density energy storage, the penetration of personal electronics has reached an unsurpassed level. This has enabled the advancements that bring the world closer through automation and the information age, but has also created a dependency for a stable, constant supply of energy. Currently, the vast majority of electricity is generated through burning fossil fuels. Although the reserves of coal and oil have served humanity well over these last centuries, they are limited and depleting at an increasing rate [1]. Besides the limited supply, burning the fuels expels huge amounts of hydrocarbons into the atmosphere. These hydrocarbons enhance earth's natural greenhouse effect by absorbing infrared light emitted by the earth, preventing it from leaving the atmosphere and therefore acting as an insulating blanket that preventing the earth from cooling down. This warming effect has numerous consequences that behave like a positive feedback loop, where the consequence increases the initial condition that caused the effect. Positive feedback loops lead to runaway effects if no active effort is taken to contain it. Deforestation, desertification, decline in coral reefs, melting of both the permafrost and the icecaps are a few examples that are amplified by climate change and enhance further warming of the planet. In 2015, the Paris climate agreement was signed to set the goal as to keep the average temperature rise well below 2°C, while striving to limit this to 1.5°C with respect to pre-industrial levels [2].

There can be debated about whether global average temperature is the only and/or best quantity in which to express the state of the environment, it is clear that technological development has provided tools to tap into earth's natural resources more effectively [4]. This has inflicted large damage to the ecosystem [5]. The intrinsic drive that most humans have for personal gain often neglects harm for third parties and is narrow-sighted, only accounting for potential harm in the near-future [4, 6]. This is reflected in a cost-analysis for a certain product or service. Only the direct costs are calculated and long-lasting, indirect costs are ignored because of lack of sense of responsibility. It is therefore suggested that the price of goods and services is to reflect the actual cost of making and/or providing them and not just the direct monetary costs [7].

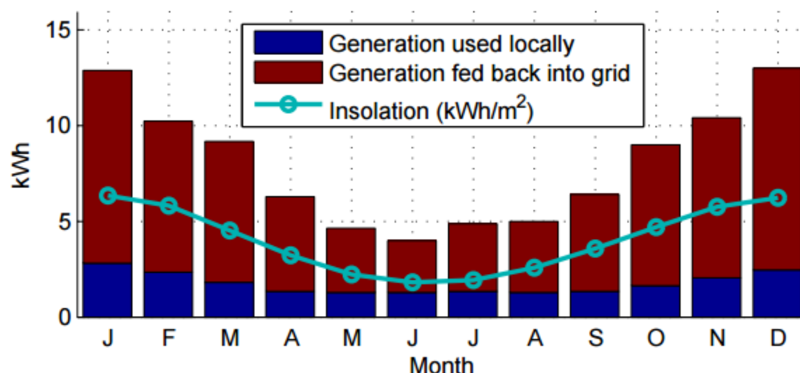

Figure1.1: A typical Australian single home load profile (blue bars) with solar insolation (line) and the mismatch that is fed back into the grid (red bars) [3]

However, we can not depend on the hope that the global economic model changes in the near future to compensate for what we take out of nature. People and their countries can either be non-willing or non-capable to take these indirect costs in consideration. Western countries have the means to pay for clean energy or fair-trade products, but it can not be expected from developing countries that struggle to accommodate their people with the most basic requirements to spend more on anything than necessary. To make a global short-term impact it is therefore crucial that renewable energy becomes the most economical form of energy.

For several projects, the price per kilowatt-hour (kWh) of renewable energy sources dropped to values below that of fossil fuel power generation. For instance, a 2016, 350 MW Abu Dhabi solar energy project will be constructed that offers energy at 2.42 $-cents/kWh [8], which is nearly half the price of conventional coal-fired power plants and sets a trend that is expected to become increasingly more common [9].

A large disadvantage of renewable energy sources is its intermittent supply. This means that the supply of energy is not constant and can be predicted only up to a certain degree. The demand in energy is also not constant but follows a fairly well defined pattern. Figure 1.1 illustrates Energy production of a small system in Australia. It shows a relatively small mismatch in winter, but a large mismatch in summer. Systems that are designed provide a minimum base load in winter are oversized for the summer months. Long-term storage of excess energy production in summer can be used in winter, which will cause less strain on the grid in summer, when most residences are overproducing.

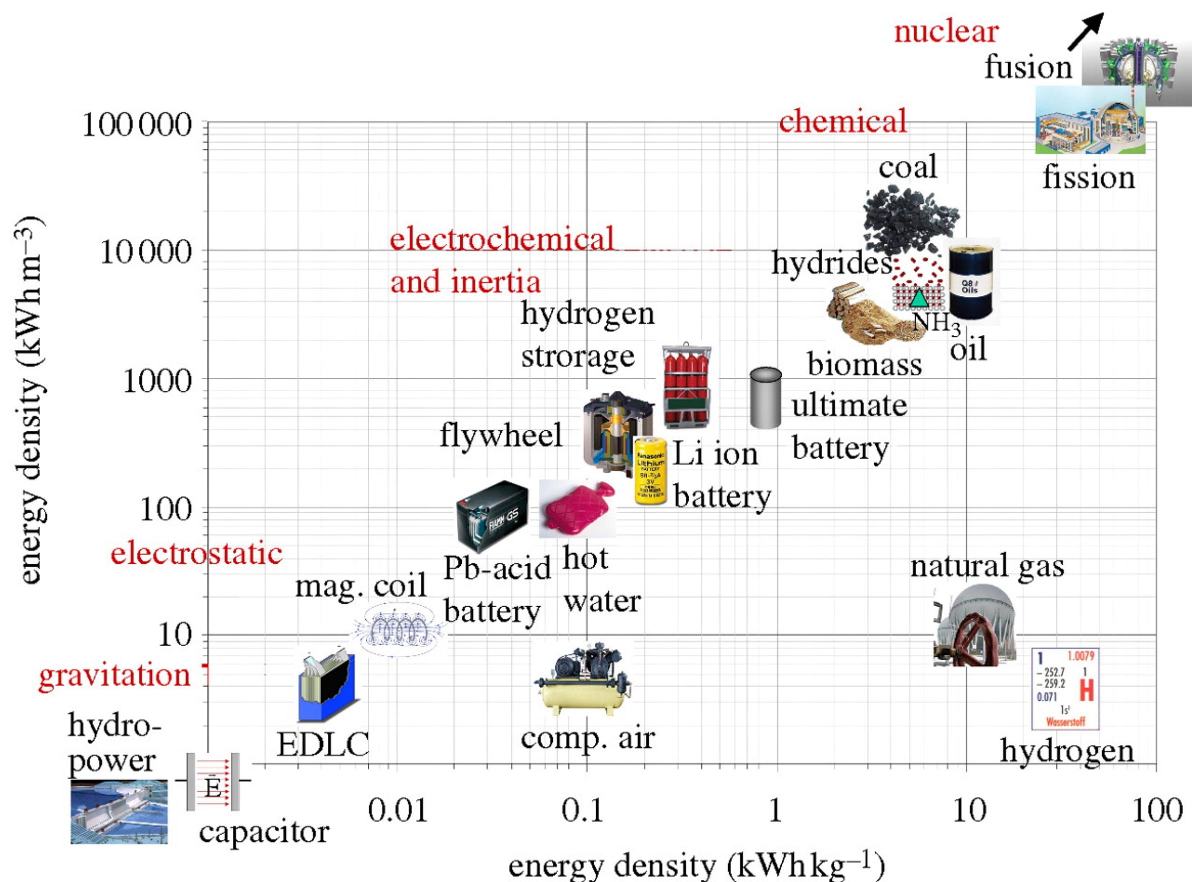

Figure1.2: A double logarithmic plot of the energy density by weight (x-axis) and volume (y-axis) of various fuels or energy storage solutions [10]

Figure 1.2 shows how much energy is contained per kilogram of weight and per volume for fuels or energy storage technologies. A good energy storage technology has high storage and release efficiency and is able to store much energy in a small volume and weight. Of the energy storage technologies in figure 1.2, hydropower, batteries and chemical energy are potential renewable energy storage solutions. Hydroelectric requires large area's and specific geographical conditions to operate, which has a very low energy density. Batteries can store much energy per volume and weight and have good charging and discharging efficiencies, but can dissipate charge over time and have limited cycle lives [11]. Compressed hydrogen has similar en-

ergy density as batteries and has negligible dissipation of energy by leakage. The discharging of compressed hydrogen is limited by the efficiency of heat-engines used to extract heat from combusted hydrogen. Fuel cells use electrochemical processes to generate electricity from chemical energy and do not have the same limitations, which allows for a much higher efficiency at lower temperatures. Fuel cells can also operate with various carbon-based chemical compounds that have a higher volumetric energy density than hydrogen and can be manufactured from the CO_2 that is produced as byproduct by many industrial processes. Currently, hydrogen is mostly produced by steam reforming of fossil fuels [12]. While CO_2 produced by fossil fuelled power plants is either expelled into the atmosphere or sequestrated in geological formations [13].

Electrolysers operate as reverse fuel cells and to add energy to specific compounds, like water or CO_2, to generate high energetic fuels like hydrogen or other hydrocarbons. Combining an electrolyser with renewable energy generation provides a clean, efficient and long-term energy storage solution. Integrating both devices in a monolithic photoelectrochemical device can omit component losses that arise from having separate devices. To be able to drive the electrolysis reaction, a voltage needs to be applied that exceeds that of conventional solar cells. To increase the voltage of a single solar cell, multiple solar cells can be stacked and incorporated in a monolithic, multi-junction structure that enhances the generated voltage and can make more efficient use of the solar spectrum.

The current state-of-the-art in photovoltaic (PV) technologies in terms of multi-junction devices with high voltage and conversion efficiency use expensive rare-earth materials, which are best suited for extra-terrestrial applications. The DEMO project aims at manufacturing a practical photoelectrochemical water splitting, CO_2 reduction device, as shown in figure 1.3. The goal of this thesis is to verify whether an a-Si:H/a-SiGe:H/nc-Si:H triple junction solar cell, processed within the facilities available to the PVMD research group can achieve the performance required by the context of this project. Record quality a-Si:H and nc-Si:H solar cells have been developed in this research group [14], which gravitates the focus of this thesis in optimising the a-SiGe:H subcell, the tunnel recombination interface layers between subcells and light management in the final triple junction device.

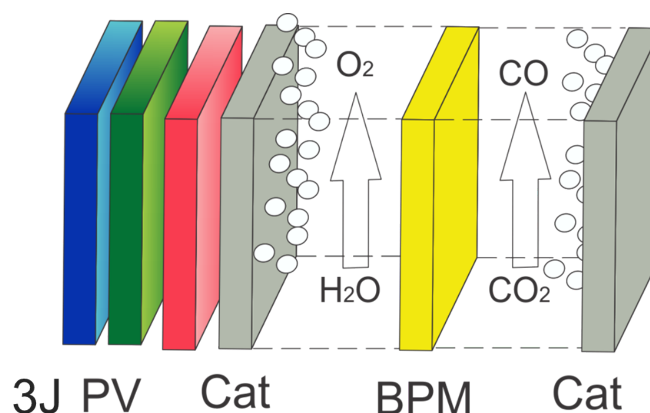

Figure1.3: A schematic of the device structure as proposed in the DEMO project. It incorporates a solar cell to directly produce high energy fuels from water and CO_2 [15]

In this thesis, the theoretical background required to interpret the results is laid out in chapter 2. The equipment used to process the materials and devices and the methods to characterise their performance are discussed in chapter 3. Chapter 4 presents the obtained results which is followed by the conclusions and recommendations based on the findings in this work in chapter 5.

2

Theoretical Background

This chapter provides the theoretical context required to understand the operation and the restrictions of the intended triple junction solar cell. It also provides tools to properly interpret the obtained results during this thesis. First, the energy provided by the sun is discussed. Next, basic semiconductor operation is explained, followed by the loss mechanisms and constraints that result from the combination of solar spectrum and semiconductor properties. Solar cell operation is discussed next along with the most common technologies within photovoltaic research. Then, optics and the characteristics to determine short, and long term solar cell performance are laid out. This chapters closes with photoelectrochemistry and its possibilities and limitations.

2.1. Solar Energy

The sun outputs incredible amounts of energy by the nuclear fusion of mainly hydrogen and helium in its core. The matter that comprises the sun heats up and releases thermal energy in the form of a spectrum of electromagnetic radiation. Idealised, this spectrum is represented by a "black-body" and depends on temperature alone. In this case, the object is required to absorb all incoming light and reflect none. No object behaves like this and therefore causes us to measure a different spectrum just outside of Earth's atmosphere in comparison to the black-body radiation. The solar spectrum, as measured just beyond earth's atmosphere, is known as AM0. The AM stands for "air mass" and denotes the amount of air the light has passed through before reaching Earth's surface. Light incident perpendicular on the surface of Earth, is denoted with AM1. Because this incidence is fairly rare, a more convenient AM1.5 is chosen as standard incidence. The air mass value for any incidence is calculated by [16]:

$$\mathrm{AM} = \frac{L}{L_0} \approx \frac{1}{cos(z)}, \tag{2.1}$$

where L is the path length through the atmosphere, L_0 is the path length at normal incidence and z is the incidence angle relative to normal incidence, the AM1.5 spectrum corresponds to an incident angle of approximately 42° relative to the surface. Figure 2.1 shows the spectral irradiance, which is the incident energy per square meter per second, as a function of wavelength of the ideal black-body radiation as well as the AM0 and AM1.5 spectra.

We see that the spectral irradiance has a sharp increase from 250-500 nm, which corresponds to UV and blue light. The peak is around 500 nm, which we perceive as green light. After which, the spectral irradiance gradually falls off into the deep infrared wavelengths. Because the atmosphere is not perfectly transparent, light will be absorbed in increasing measure when passing through more air. The elements and constituents that make up the atmosphere absorb specific wavelengths of light, which explains the harsh drops in spectral intensity of sunlight at AM1.5. Integrated over the wavelength range, the solar intensity is $I = 1000\ \mathrm{W\,m^{-2}}$. The electromagnetic radiation from the sun is quantised and photons with different wavelengths have different energy according to

$$E_{ph} = \frac{hc}{\lambda}. \tag{2.2}$$

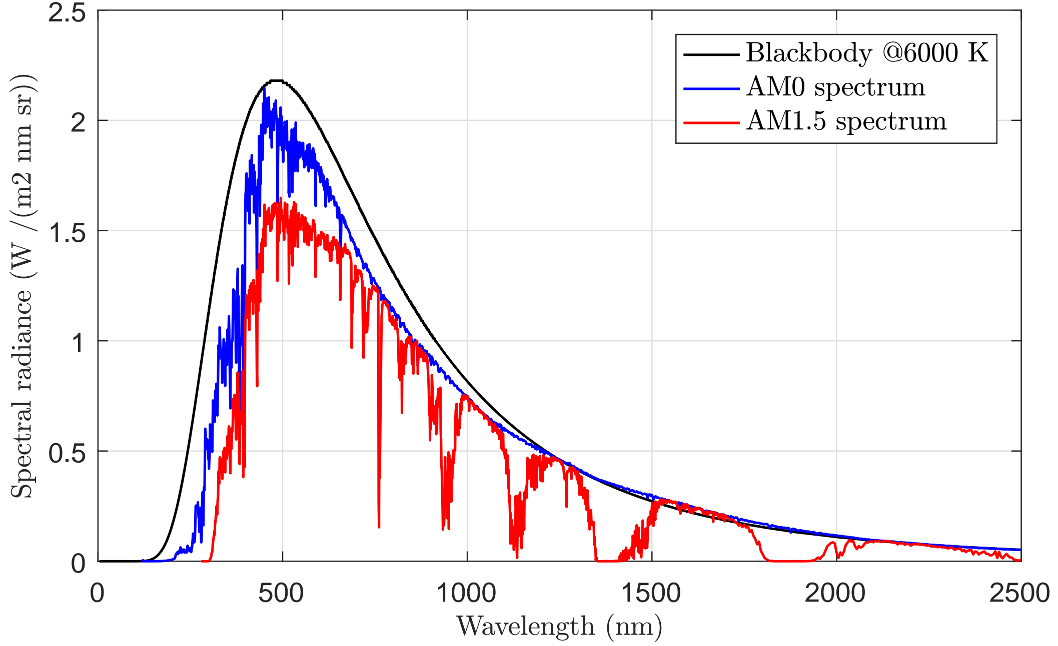

Figure2.1: The solar AM1.5 and AM0 spectra along with that of a ideal blackbody with T =6000 K according to Planck's law [17]

In this equation, the photon energy in Joule is denoted with E_{ph}, h is Planck's constant, c is the speed of light in vacuum and λ is the wavelength of the photon. Because λ is in the denominator, the energy of a photon decreases with increasing wavelength. Because the energy per photon is wavelength dependant, the amount of photons required to meet the spectral irradiance of the solar spectrum also varies for different wavelengths. The spectral photon flux, or the amount of photons per unit area per second as function of wavelength is given by

$$\Phi(\lambda) = P(\lambda)\frac{\lambda}{hc}, \tag{2.3}$$

where $\Phi(\lambda)$ is the spectral photon flux in photons m^{-2} nm^{-1} and $P(\lambda)$ is the spectral power per wavelength. The spectral photon flux is useful as the current generated in solar cells depends on the number of photons incident on a solar cell and their energy. The total photon flux over a wavelength range can be calculated by integrating over that wavelength range.

$$\Phi = \frac{1}{hc}\int_0^{\lambda} P(\lambda)\lambda \, d\lambda. \tag{2.4}$$

2.2. Semiconductor properties

In a single atom, electrons may possess only a few discrete energy levels. Intermediate energy levels are impossible for electrons to obtain and the corresponding energy states are aptly named "forbidden states". In the lower, allowed, energy states, the electron is considered bound to the nucleus. In the higher energy states, the electron may have sufficient energy to free itself from the nucleus. When atoms form covalent bonds and are combined to form a larger, periodic structure, more energy states are possible which fill in some of the gaps between energy states. This forms energy bands. Two different types of energy bands are distinguished. The energy band of allowed states for valence electrons, the outermost electrons of an atom that participate in covalent bonds, is the valence band. The conduction band consists of the unbound energy states. Here, electrons carriers are able to freely move in a crystal lattice.

In conductors, these bands overlap, which means that for many bound states, there are unbound states which require only a small difference in energy level, some of which require a release of energy. This enables easy access for the electrons into the conduction band, which is reflected in the materials good electric conductive properties. Insulators and semiconductors have a band of forbidden states in between the con-

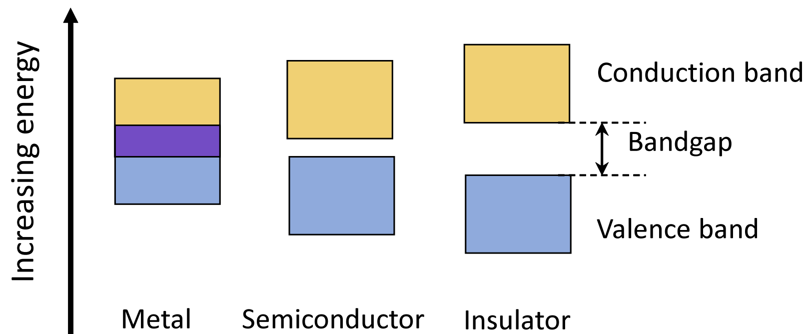

Figure2.2: Energy band diagram of metals (left), semiconductors (middle) and insulators (right)

duction and valence bands, which is also known as the band gap. For semiconductors this gap is relatively small and electrons may be promoted to the conduction band when provided with sufficient energy. The bandgap of a material can be calculated by

$$E_g = E_c - E_v, \tag{2.5}$$

where E_G is the bandgap energy, usually denoted in electron volt (eV). E_C is the conduction band edge, or the lowest possible unbound energy state and E_V is the highest possible bound state. Semiconductors with large bandgap are called insulators. Figure 2.2 illustrates the energy bands and their overlap, for metals, or band gaps, for semiconductors and insulators.

The working principle of solar cells is that the photons emitted from the sun have larger energy than the material's bandgap, which means a valence electron absorbing the energy can break its bond and be promoted to the conduction band. External influences are not always required for this process. In semiconductors at room temperature, a small fraction of covalent bonds are broken that promotes electrons to the conduction band, due to thermal energy which can exceed the bandgap. This is an example of the generation process. The electrons can then move freely through the lattice and leave behind a vacancy, or also referred to as "hole". This vacancy may be filled by another valence electron, which will effectively result in movement of the hole, as the valence electrons leaves behind a vacancy of its own. Holes can be viewed as positively charged particles with properties similar to electrons. Generation always creates an electron-hole pair because an electron cannot be liberated without leaving a vacancy. Vacancies can also be filled by electrons from the conduction band, which is the opposite effect of generation and is known as recombination. The energy of the electron will decrease from the conduction band to the valence band which can be dissipated in several manners. Various recombination processes are discussed in the next section, 2.3. Without other external influence, the rates of generation and recombination even out and the material is said to be in thermal equilibrium. The Fermi-Dirac distribution is a probability density function and describes the probability of a specific energy state being occupied by holes or electrons. A semiconductor material at thermal equilibrium, the likeliness of finding a hole in the valence band is equal to that of finding an electron in the conduction band, which means that the corresponding energy of the average occupied state is halfway the valence and conduction band. This energy level is called the Fermi level (E_F).

In pure, or intrinsic material, every liberated electron leaves a hole and every hole that annihilates does so with an electron. This gives equal concentrations of electrons, n and holes, p. These concentrations can be altered by doping. Doping introduces impurities in a lattice. In a silicon lattice, silicon atoms can be replaced by either boron or phosphorous atoms. Because silicon has four valence electrons it can make four covalent bonds. Boron and phosphorous have three and five valence electrons, respectively. when a silicon atom is replaced by a phosphorous atom, it uses four of its five valence electrons to form bonds with the neighbouring silicon. Due to the absence of other valence electrons, phosphorous' fifth valence electron is usually promoted by thermal energy. Similarly, boron can only bind to three silicon atoms, which introduces a hole in the lattice. Phosphorous provides an extra electron in the lattice, while boron can obtain an electron from a Si-Si bond. These dopants are therefore called electron donors and acceptors, respectively. Semiconductor materials doped with electron donors are referred to as n-type material. Conversely, doping intrinsic material with electron acceptors will give p-type material. The dopants do not affect the net charge of the bulk as the charge of the nucleus matches that of their respective electrons. The dopant atoms do ionise as they donate

or accept an electron from the lattice as depicted in figure 2.3.

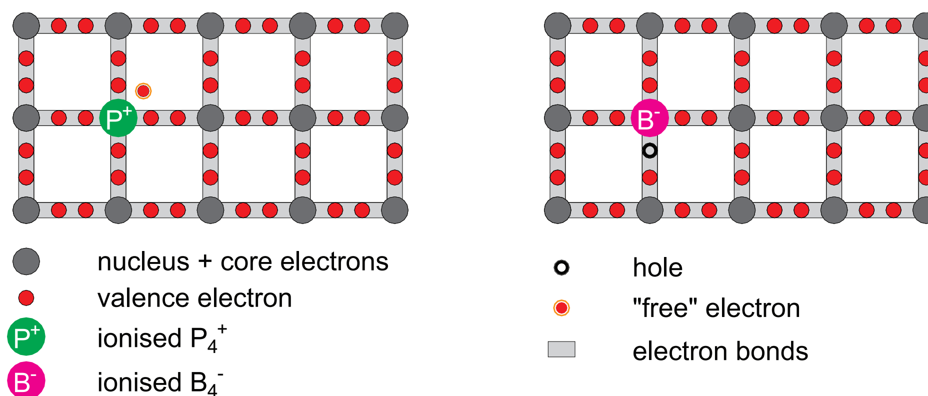

Figure2.3: Doping of phosphorous or boron in a silicon lattice using the bonding model. An adaptation of [18]

The introduction of impurities by doping alters the concentration of charge carriers compared to intrinsic material. This will result in a shift in probability of finding a charge carrier in a certain state. For instance, in phosphorous doped n-type material, the probability of finding an electron in the conduction band is higher than with respect to intrinsic silicon by the introduction of excess electrons by the phosphorous atoms. This is represented by an shift in E_F from half way the bandgap towards the conduction band edge. Similarly, p-type material will exhibit a shift in E_F towards the valence band edge. Moreover, the introduction of the impurities provides energy states within the bandgap close to the band edges. This is because, for n-type, an electron can be weakly bound to the phosphorous, which indicates a "new" energy state close to the conduction band as shown in figure 2.4.

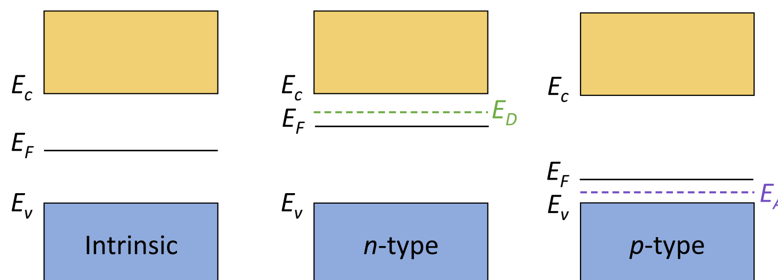

Figure2.4: Position of E_F as well as the introduction of energy states close to the band edges in n- and p-type semiconductors. An adaptation of [18]

2.3. Recombination and other loss mechanisms

Solar cell operation requires three sequential steps: Generation, separation and collection. Generation can occur when photons with sufficient energy transfer that energy to an electron, thus liberating it from its lattice. This creates an electron-hole pair. If both particles are separated, which is discussed more extensively in the next section, and allowed to recombine after passing through an electric circuit, the attained energy may be harvested. If recombination occurs elsewhere, the energy is lost. Three distinct recombination mechanisms are identified: Radiative, Shockley-Read-Hall, and Auger recombination. Radiative recombination, or direct recombination, is a band-to-band process where an excited electron encounters a vacancy in the valence band. The difference in energy between both states, typically the bandgap energy, is dissipated by ejecting a photon with that wavelength or multiple phonons. Similar to the discrete photons, phonons are quantised lattice vibrations that are associated with thermal energy. Radiative recombination is more pronounced in direct bandgap materials, like gallium arsenide and indium phosphide, than for those with an indirect bandgap like crystalline silicon.

The conduction, or valence band edge can vary as function of momentum. For direct bandgap materials, the lowest energy in the conduction band and the highest energy in the valence band have the same corresponding momentum. This means that only the bandgap energy is required to acquire an energy state in the

opposite energy band. For indirect bandgap materials the top of the valence band and bottom of the conduction band do not allign in terms of momentum and an extra phonon interaction is required. This additional criterion lowers the absorption in the material, but in the same way also suppresses radiative recombination.

Shockley-Read-Hall (SRH) recombination is also known as trap-assisted recombination. Section 2.2 mentions how doping a semiconductor device induces trap states near the band edges. Voids in the lattice or unbound valence electrons at a layers' surface due to the absence of a neighbouring atom also provide additional possible energy states in the forbidden band. This type of recombination is usually the most dominant, especially in indirect bandgap materials. Because charge carriers are more likely to make smaller jumps in terms of energy, trap states halfway both band edges therefore results in the highest recombination rate as this provides the combination of the smallest energy differences. Doped layers are essential for solar cell operation, but have a large defect density and have a high rate of SRH recombination. In the bulk material, SRH recombination can be limited by having high material quality with low defects. The surface recombination by the absence of neighbouring atoms can be limited by passivating the dangling bonds with hydrogen. Silicon dangling bonds are well passivated by hydrogen due to its single valence electron, meaning that when it bonds to silicon, it will not leave a dangling bond itself.

Auger recombination, finally, is a recombination process that involves three particles. An electron and hole recombine, but rather that the energy is dissipated in terms of heat or a photon, a third particle absorbs the energy and is excited deeper into the conduction, or valence band for electrons or holes, respectively. The excited particle relaxes to the band edge and dissipates its energy and momentum to the lattice as vibrations which relax by emission of heat. Auger recombination becomes more prominent when there are more charge carriers that recombine and to absorb and dissipate the energy when recombination occurs. High charge carrier concentrations are achieved by high doping concentrations or concentrator photovoltaics, where light is focused onto a small area.

An important parameter in either recombination mechanism is charge carriers' lifetime. Which is the average time a charge carrier can move in the lattice before recombining by either of the aforementioned processes.

A loss mechanism other than recombination is thermalisation. When electrons absorb the energy of photons with $E > E_g$, they can be excited deep into the conduction band, or for the case of holes, deep into the valence band. The excess energy will be thermalised within a very short time, meaning that the energy state will relax to that of the lowest/highest energy state in the conduction/valence band by emission of phonons resulting in heat. Although all of the photon energy is absorbed, only the part that is the bandgap energy can be used to produce electrical work.

On the other hand, photons with energies lower than the bandgap are not able to excite electrons/holes to the conduction/valence band. This means that the energy they carry can not be utilised by the solar cell. Shockley and Queisser calculated a theoretical upper limit for solar cell conversion efficiency based mainly on thermalisation and non-absorption. They also included radiative recombination and its consequence for the open-circuit voltage and non-perfect FF [18]. The Shockley-Queisser (SQ) limit is shown in figure 2.5 as function of bandgap energy for the AM1.5 spectrum.

The SQ efficiency limit is shown to be approximately 33% at $E_g = 1.34$ eV.

2.4. p-i-n junction

For solar cell operation it is essential to separate the photo-generated electron-hole pairs to prevent recombination and thus, the dissipation of the absorbed energy. For this, thin-film technologies, which will be discussed more in-depth in section 2.5, rely on sandwiching intrinsic absorber material between a p- and n-layer. At the p/i interface, the thermally excited electrons move into the p-type acceptor material, where they participate in B-Si bonds. Similarly, Excess electrons from the n-layer diffuse into the intrinsic bulk, where they recombine with thermally excited holes. In both occasions the number of free charge carriers falls, which leaves ionised atoms in the lattice. The boron atoms, with an additional electrons are negatively charged and the phosphorous atoms are positively charged, and thus generate an electric field across the intrinsic bulk, if the intrinsic layer is thin and the dopant concentration is sufficient.

Transport of charge carriers can have two distinct driving forces. A concentration gradient will cause charge carriers to move from places with high particle concentration to low concentration due to random movements. This process is called diffusion and will cause particles to spread out homogeneously in a material. The other process uses an applied external electric field to transport charge carriers and is called drift. It is good to note that the movement of charge carriers produces an electric current. The drift current depends

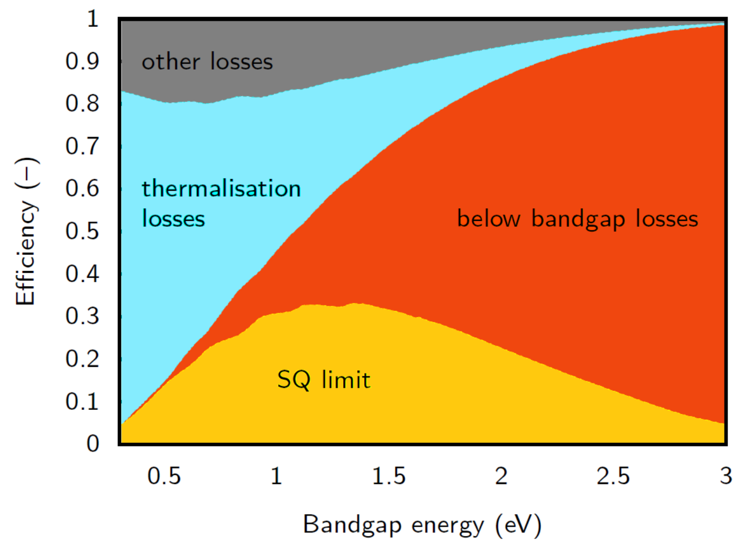

Figure2.5: The Shockley-Queisser limit for solar cells illuminated by the AM1.5 spectrum as function of bandgap [18]

on the strength of the electric field over the intrinsic material and the electron and hole mobility, $\mu_{n/p}$, which depends on material properties. Drift is the dominant transport mechanism in the intrinsic absorber layer in p-i-n junctions due to the electric field. Diffusion is suppressed by the short lifetimes, and thus small diffusion length of the charge carriers in the relatively defective intrinsic bulk. Because of the high charge carrier concentration in the doped layers, the diffusion mechanism dominates transport in the p- and n-layers.

Figure 2.6 shows a schematic band diagram of a p-i-n junction thin-film solar cell with nc-SiO$_x$:H p, and n-layers and an a-Si:H intrinsic absorber layer.

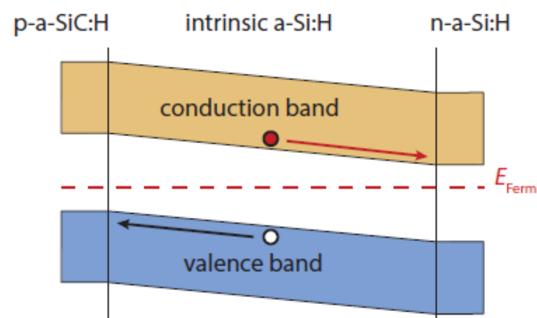

Figure2.6: A p-i-n junction for an a-Si:H solar cell with nc-SiO$_x$:H as p- and n-layers. An adaptation of [18]

The photo-generated charges are separated by the electric field across the intrinsic layer, the electrons drift to the n-layer, where they are collected by the back contact. In contrast to the substrate configuration of n-i-p solar cells, p-i-n type solar cells are superstrate devices because the light first passes through the material on which the device is deposited, which is often a type of glass. This also means that, for the holes to be collected from the p-layer, a conductive layer must be added in between the glass superstrate and the p-layer. Besides good conductive properties, this layer must also be very transparent, as any photons that are absorbed in this layer do not add to the photo-generated current. This layer is referred to as transparant conductive oxide (TCO). The front contact of the solar cell can be deposited anywhere on the superstrate, as long it is in contact with the TCO. Most TCO's consist of an metal-oxide that suppresses parasitic absorption due to a large optical bandgap. The conductive properties are obtained by doping, mostly this is also a metal. Some examples of TCO's are SnO_2:F (FTO), ZnO:Al (AZO), In_2O_3:H (IOH) and ITO, which is a mixture of approximately 90% In_2O_3 and 10% SnO_2. Different TCO's have different properties of light transmission and conduction. Another factor in choosing a TCO for a solar cell is ease of deposition and cost, as indium is a rare earth element and has numerous applications in other industries.

2.5. Photovoltaic technologies

First generation photovoltaic (PV) technologies was sparked by the development of high purity crystalline wafers. The high material quality and low defect density give the material good performance. The current world record for crystalline silicon (c-Si) solar cells is held by Kaneka and achieves 26.7% conversion efficiency [19], which is very close to the calculated theoretical maximum efficiency for c-Si of 29.43% [20]. The silicon wafers are produced in two distinct types. Monocrystalline and polycrystalline wafers as shown in figure 2.7. The crystal grains as seen in the polycrystalline wafer have boundaries which facilitate recombination. Processing steps can be added to grow silicon in a single crystal structure without grains or boundaries, which results in the monocrystalline wafers. This increased purity gives higher performance, but also requires more energy during processing, which suppresses the cost effectiveness.

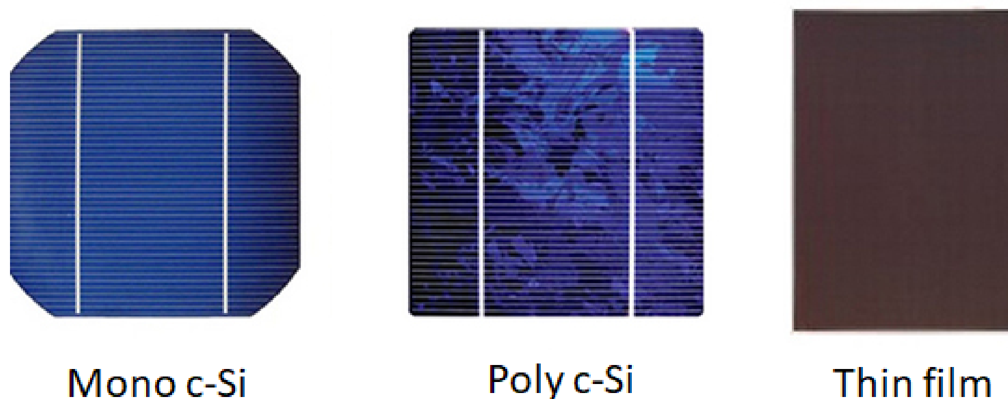

Figure2.7: From left to right: a monocrystalline, polycrystalline and thin-film silicon solar cell [21]

Second generation solar cells were initially aimed at achieving unprecedented cost effectiveness, making large scale implementation much more feasible, but due to the high amount of installed capacity of c-Si and the learning-by-doing curve, thin-film technologies have not made the breakthrough that was predicted. Thin-film solar cells bypass the c-Si wafers and are manufactured from gases that adhere to a sub- or superstrate by nucleation. These processes, some of which are further explained in section 3.1.2, allow for the growth of very thin films of nano-sized crystals or completely amorphous materials that exhibit high absorption of light due to their, mostly, direct bandgaps. Phase transitions with varying crystalline volume fraction is shown in figure 2.8. The high absorption of the materials can result in much thinner absorber layers, meaning that less material is required. Moreover, the precursor gases that are suitable for thin-film production can be very cheap, using abundant materials like silicon, hydrogen and oxygen. The films do not provide structural integrity for themselves and need a mechanical carrier. This can be a flexible material, allowing for curved and bent solar cells. Figure 2.7 also shows a thin-film module. There are various subcategories in thin-film technologies. Thin film silicon solar cells can be manufactured from, and among other materials, hydrogenated amorphous silicon (a-Si:H), hydrogenated nanocrystalline silicon (nc-Si:H), also known as μc-Si:H, hydrogenated nanocrystalline silicon oxide (nc-SiO$_x$:H) or hydrogenated amorphous silicon germanium alloys (a-SiGe:H). Currently the world record for a thin-film silicon based single-junction devices is approximately 11-12% [22].

Other thin-film technologies are chalcogenide and III-V solar cells. Chalcogenide solar cells are subdivided in CdTe, or cadmium telluride and CIGS solar cells. CIGS are based of a combination of various elements, the main of which are copper, indium, gallium and selenium, that also gave the technology its name. Other III-V technologies are produced from elements in the third and fifth group of the periodic table of elements like gallium, arsenic, indium and phosphorous. The aforementioned thin-film technologies constitute of materials with very good properties for solar cell operation. However, the common theme in these technologies is that they rely on scarce elements, mostly indium, gallium or arsenic, which prevents the production from being scaled up to meet global energy demands.

Finally, third generation concepts differentiate themselves from the other generations by overcoming the SQ limit. Some concepts are very exotic concepts like hot carriers absorption, which attempts to harvest the excess bandgap energy by collecting a charge carriers before they can thermalise, More mainstream method

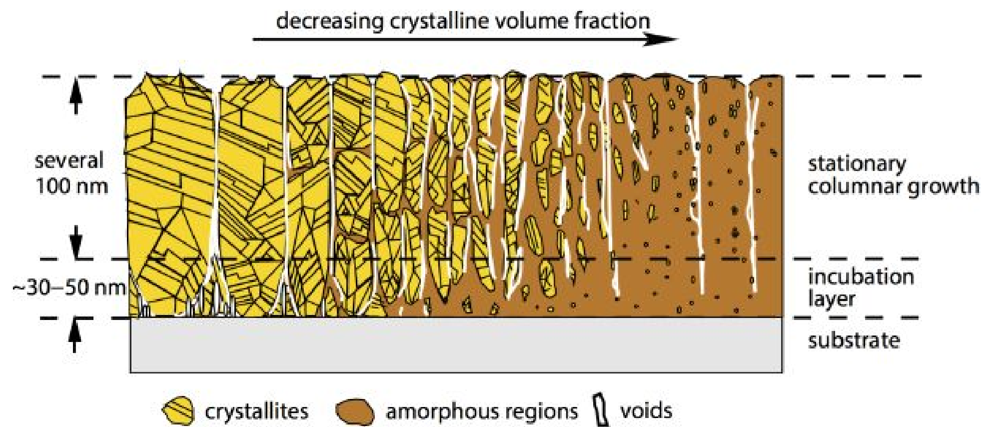

Figure2.8: The phase transition from crystalline (left) to amorphous (right) [23]

of exceeding the SQ limit is by creating multi-junction devices. Extremely high efficiencies have already been reported for multi-junction devices. The highest reported efficiency for terrestrial applications is 38.8% [22] which uses a quintuple junction based on III-V technology. The highest overall confirmed conversion efficiency is 46.0% which is achieved by a III-V quadruple junction [24]. The increased efficiency was obtained by concentrating the incident irradiance by a factor 508, that beneficially affects V_{OC} and FF.

2.6. Multi-junction solar cells

As mentioned in the previous section, thin-film multi-junction solar cells have the potential to reach both very high efficiencies and also low cost. The biggest loss mechanisms discussed in the SQ limit are non-absorption and thermalisation. Figure 2.9 shows multi-junction solar cells increase this spectral utilisation by stacking multiple solar cell with different bandgaps. The subcell with the highest bandgap is placed on top because it has the best utilisation for high energy photons and is transparent to those with energy lower than its bandgap, which leaves a part of the spectrum to be absorbed by the next subcell in the stack.

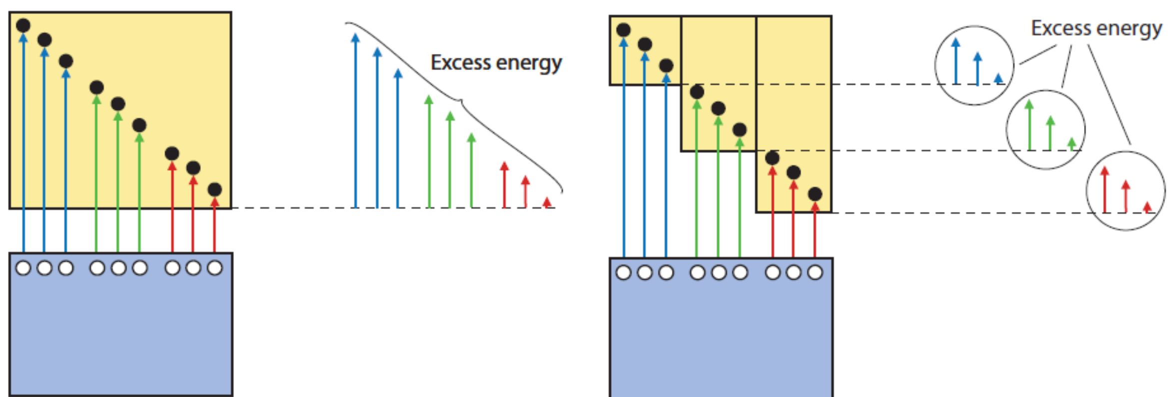

Figure2.9: Spectral utilisation of a single-junction solar cell (left) and a multi-junction solar cell which consists of three junctions with different bandgaps (right) [18]

Multi-junction solar cells behave electrically like single-junction solar cells that are electrically connected in series. The electrical potentials add up, while the current through the subcells is equal and limited by the solar cell producing the least amount of current. The generated electron-hole pairs of each junction's intrinsic absorber layer are separated by the internal electric fields generated by subcells respective p, and n-layers. In the p-i-n configuration, the front contact collects the holes generated in the top cell, while the back contact collects the electrons generated in the bottom cell. In the case of a double junction, or tandem, device, the electrons from the top cell are directed towards the n-layer of the top cell, while the the holes generated in the bottom cell are directed towards the p-layer of the bottom cell, which is adjacent to the n-

layer of the top cell. Although recombination is in general an undesired loss mechanism in solar cells, here, the recombination is essential for a well functioning device. A lack of recombination at this p-n interface will result in accumulation of charge carriers that can deteriorate the electric field over the intrinsic absorber layer, thus reducing the collection of photo-generated charge carriers.

The proposed 3J device structure is based on silicon thin-film technologies because they are much more likely to see large up-scaling than the expensive, but more efficient III-V multi-junction solar cells. The bottom cell of a silicon based 3J solar cell could be either c-Si or nc-Si:H which both have a bandgap of approximately 1.1 eV. With this bandgap as a constraint, the optimum bandgaps of the two other subcells was calculated to be 2.0 eV and 1.45 eV. A device of this structure could possibly reach 21.4% conversion efficiency [25]. The most popular candidates for the top and middle cells are a-Si:H, with E_g = 1.7 eV, and a-SiGe:H, with a tuneable bandgap between $E_g = 1.1 - 1.7$ eV by changing the germanium content [26]. An alternative for a-Si:H in the top cell can be a-SiO$_x$:H, which has an ideal bandgap of around 2 eV, but issues generating sufficient current [27]. A common alternative middle cell could be a second, but thinner, nc-Si:H cell which shows good current generation and stability, but lacks in voltage.

One of the most important design criteria is a good interconnection between neighbouring subcells. To close the electrical circuit, the electrons in the top cell n-layer must recombine with holes from the bottom cell p-layer. This is realised by a quantum-mechanical event called tunnelling. Tunnelling is a stochastic process where a particle transits from one combination of energy and position, or state, to another, without assuming an intermediate state. Large differences in energy/position lower the probability of a tunnelling event. Electrons and holes tunnel from the conduction band and valence band, respectively, to reach the state of the other particle. Figure 2.10 shows an simulated band diagram for a tunnelling recombination junction (TRJ) of a p-i-n/p-i-n configuration double-junction device. The photo-generated electrons in the intrinsic layer on the far left move further down the conduction band in towards the n/p junction. Conversely, holes generated in the intrinsic layer on the far right move up the valence band also towards the p/n interface. The tunnelling probability will increase when the conduction band edge of the n-layer, indicated in red, aligns with the valence band edge of the p-layer, indicated in blue.

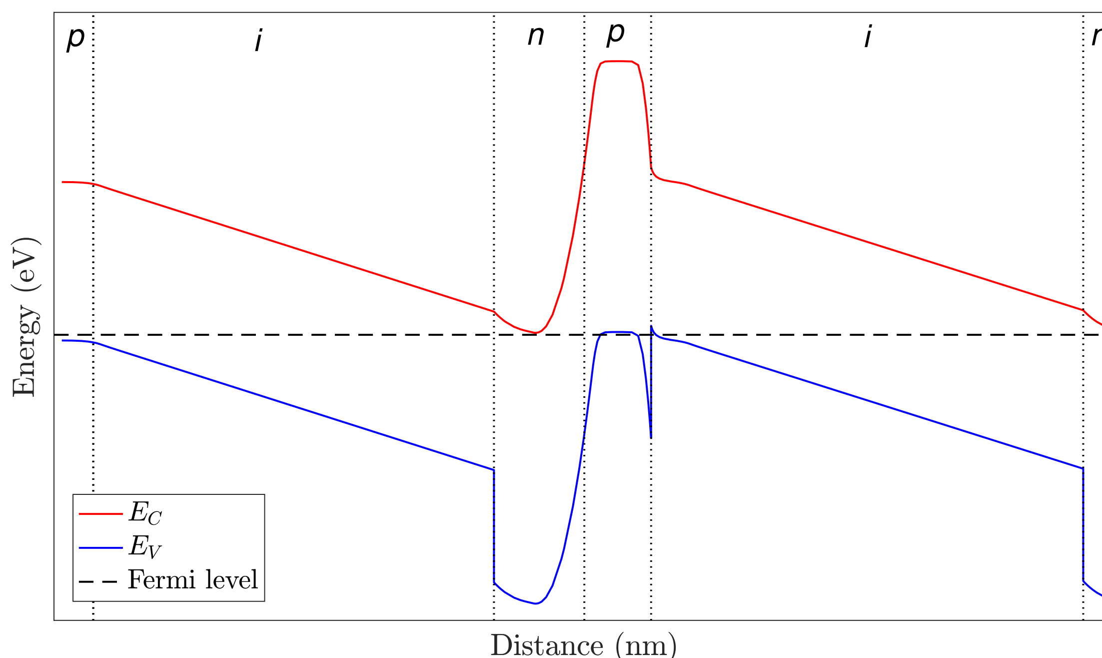

Figure2.10: A simulated energy band diagram of a TRJ in a p-i-n/p-i-n double-junction solar cell at equilibrium. The Fermi level is the reference at 0 eV

A junction between a p- and n-layer with both very small activation energy, which is the energy difference from the Fermi level to the closest band edge, will have better energy band alignment and requires a smaller jump in energy for the charge carriers. This can be achieved by high doping of the n, and p-layers. Adding

thin, highly doped layers between the n-layer and p-layer typically enhances tunnelling. In a $n/n^+/p^+/p$ structure, electrons and holes will be forced to drift close to the n^+/p^+ interface due to the electric field. This causes the locally higher doped regions to act as a trap for their respective charge carriers as well as providing very low values for activation energy.

The difference in bandgap energy and doping concentration is what causes the sharp band edges at the p/i interface in the middle. This also provides an energy barrier, which the holes have to tunnel across.

Keeping the highly doped layer thin ensures the charge carriers to be trapped in a small space region, which decreases the required tunnelling distance. Too thin highly doped layers will cause the depletion region width to encompass the layer thickness, increasing the activation energy and possibly undoing the increased doping. Another benefit for tunnelling is that higher doping introduces traps states in the forbidden band that reduce the tunnelling required in terms of energy when a charge carrier is trapped in one.

2.7. Optics

Light management is one of the main design parameters for solar cells. Disregarding light management can lead to unnecessary reflection of light away from, and out of the solar cell device, as well as heavily mismatched current generation in the subcells of multi-junction devices. Light incident on an object can result in three different outcomes. The light can be reflected of the on the surface, it can enter the material and get absorbed, or it can be transmitted, meaning it leaves the object.

$$1 = R + A + T \tag{2.6}$$

Equation 2.6 describes this mathematically where R, A and T are the reflectance, absorptance and transmittance of light, respectively. These unit-less quantities represent the fraction of light that undergoes the respective process and always sum to unity. Material properties that govern reflection and absorption are contained in the refractive index, n. For perpendicular incidence reflection occurs at the interface of two media with different refractive indices according to:

$$R = \left| \frac{n_1 - n_2}{n_1 + n_2} \right|^2, \tag{2.7}$$

where n_1 and n_2 are the refractive indices of the two respective media. It can be noticed from this equation that when two media have a large contrast in refractive index, the reflection is greater. One method to enhance light in-coupling in solar cells is using refractive index grading to limit reflection. This process is based on adding one or more layers between two media with a refractive index in-between the both, reducing the reflection at each interface and decreasing the total reflection substantially. Strong reflection also occurs when the phase of the incident light coincides with that of the reflected light. Whether this occurs for light of a specific wavelength depends on the thickness of a specific layer, d and its refractive index,

$$\lambda_B = 4dn, \tag{2.8}$$

in which, λ_B is the Bragg wavelength, for which, the layer shows high reflectance. The constant, 4, arises from the phase-shift light experiences when it reflects of a surface and the fact that the layer is traversed twice.

Another method to reduce light leaving a solar cell is texturing. When passing from one medium into the other, the non-reflected light is refracted. The angle of refraction depends on the angle of incidence and the ratios of the refractive indices of the two media according to Snell's law. The total traversed distance of non-absorbed light will be twice the thickness of the material. A textured surface will provide an angle of incidence and therefore also an angle of refraction. All texture features that provide a net angle of incidence will cause the light to refract and will provide a longer optical path length through the material. For thin-film technologies, the texture is provided by the TCO and the glass superstrate. Most thin-film technologies, with sufficiently thin absorber layers, can still show the same texture on the back side of the solar cell, albeit somewhat less rough, which will scatter photons that reach the back reflector which will add even more path length for the photons to be absorbed by the material. Various materials can have different measures of light absorption for different wavelength. The light intensity is attenuated exponentially and depends on the material's absorption coefficient.

For solar cell applications, T is usually assumed to be 0 due to the thick metal stack (0.5-1 μm) at the back, which either absorbs or reflects light back into the solar cell.

2.8. Solar cell performance

The performance of a solar cell is quantified by four parameters. The maximum produced power P_{max}, the short circuit current density J_{SC}, the open circuit voltage V_{OC} and the fill factor FF. These parameters are determined by illuminating the solar cell and can be used to calculate the conversion efficiency η, when the incident power is known. Consistency between measurements is crucial to be able to compare the performance of solar cells. The standard test conditions (STC) are determined to provide similar conditions that could affect solar cell performance. STC dictate that the light incident on a solar cell should agree to the AM1.5 spectrum and have a total integrated irradiance of 1000 W m^{-2} while being kept at 25°C.

Electric current, I, is given by the flow of charge per second (A = C/s), which is directly proportional to the electron flow rate by the elementary charge ($q \approx 1.602 \cdot 10^{-19}$ C). In the ideal case, where all photons generate an electron-hole pair and where all electrons are collected, the incident photon flux is equal to the electron flow rate. When extracting the generated electric current from a solar cell, any resistive components in the electric circuit diminish the flow of current according to Ohm's law,

$$V = I \cdot R, \tag{2.9}$$

where V is the electric potential or voltage produced in Volts (V), in this case, by the solar cell and R is the ohmic resistance in Ω of the external circuit. The largest current a solar cell can generate is in the limit case where $R \to 0$ and thus, $V = 0$. This is also known as short-circuit conditions and gives I_{SC}. To be able to compare solar cells with different active area's, the produced current and short circuit current are typically scaled down to current densities, J and J_{SC}, in A·m^{-2} or mA·cm^{-2}.

Similar to J_{SC}, there is a maximum electric potential a solar cell can generate, which occurs in the limit case of $R \to \infty$, which is the open circuit condition, where $J = 0$. The open circuit voltage V_{OC} is the condition at which the charge carriers are separated and accumulate at the contacts. Due to the mutual repulsion and limited carriers lifetimes, there is a limit to how much charge can be accumulated. Equation 2.10 is an approximation that is justified for the case that $J_{ph} \gg J_0$, where J_{ph} is the photo-generated current density and J_0 is the saturation current density. J_0 is an intricate quantity and also known as the recombination parameter and should be kept as low as possible [28].

$$V_{OC} = \frac{nk_BT}{q} \ln\left(\frac{J_{ph}}{J_0}\right) \tag{2.10}$$

The product $k_B \cdot T \cdot q^{-1}$ consists of the Boltzmann constant, temperature and elementary charge and is also known as the thermal voltage. Its value at 300 K is approximately 0.0259 V. The diode ideality factor, n, is equal to unity for an ideal diode and increases up to 3, depending on the device's major recombination mechanism [29]. Although a high ideality factor appears to be beneficial from equation 2.10, it is a complex factor that has adverse effects for FF, J_{ph} and is often accompanied by deterioration of solar cell characteristics, like J_0. For different solar cells measured at STC, J_{ph} does not vary much, but J_0 can vary substantially, thus impacting the V_{OC}. It shows that V_{OC} is therefore also a measure of recombination of a solar cell.

J_{SC} and V_{OC} are the respective maximum current density and voltage a solar cell can produce, but their conditions of infinite of no resistance conflict. There is a value for the resistive load, where the combination of maintained voltage and generated current density multiply to a maximum produced power density, P_{max},

$$P_{max} = J_{mpp} V_{mpp}, \tag{2.11}$$

where J_{mpp} and V_{mpp} are the associated values for current density and voltage at this maximum power point (MPP). The fill factor (FF) is a measure of how well the solar cell is able to maintain its J_{SC} and V_{OC} up to its maximum power point. The FF is the ratio of the maximum power produced by a solar cell relative to the maximum hypothetical power that the solar cell would produce if it did not suffer from a decline of J_{SC} and V_{OC}.

$$FF = \frac{J_{mpp} V_{mpp}}{J_{SC} V_{OC}} \tag{2.12}$$

Figure 2.11 shows graphically how the FF is the ratio of the surface area of the squares formed by P_{max} and multiplying J_{SC} and V_{OC}

The when the output power is known, the conversion efficiency can be calculated from the power incident on the solar cell per unit area, P_{in}, using

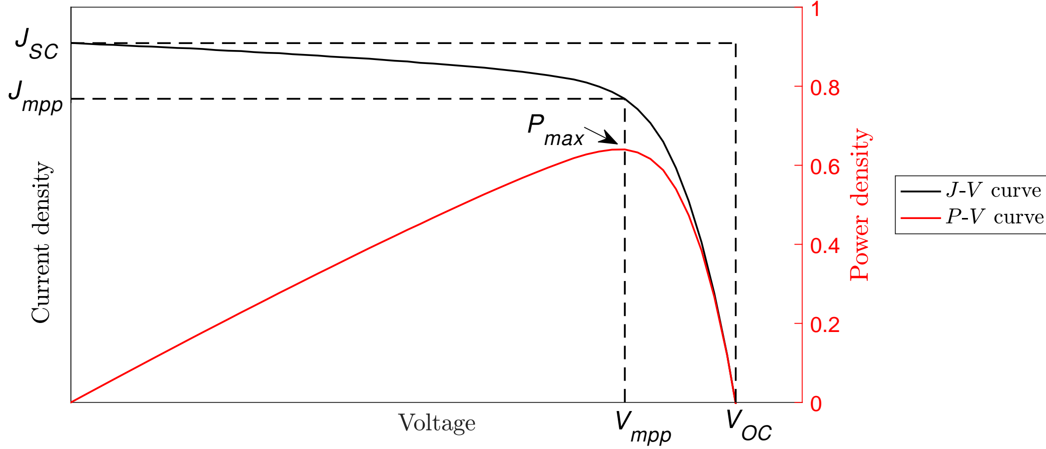

Figure2.11: The J-V curve of a solar cell showing its MPP and corresponding J_{mpp} and V_{mpp} as well as its J_{SC} and V_{OC}

$$\eta = \frac{P_{max}}{P_{in}} = \frac{J_{mpp}V_{mpp}}{P_{in}} = \frac{J_{SC}V_{OC}FF}{P_{in}}. \tag{2.13}$$

To understand operational losses in voltage and current, an electrical model, as seen in figure 2.12 can be used. The model describes a solar cell as a current source connected in parallel to a diode. To increase the model's accuracy, another diode is added along with two resistors to account for several losses. The second diode represents recombination in the p-n junction.

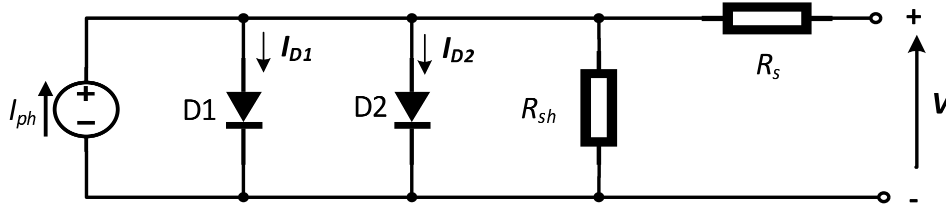

Figure2.12: The electric equivalent circuit of a non-ideal solar cell in accordance to the two-diode model

The series resistance, R_s, of actual solar cells is caused by the resistance of its constituent materials and is further influenced by the contact resistance between the semiconductor material and the metal contacts, and the resistance of those contacts. A higher series resistance leads to a greater potential drop over the solar cell which mainly affects the cells operational voltage according to equation 2.9. The parallel, or shunt, resistance, R_{sh}, represents the measure of isolation of the positive and negative terminals of the solar cell. A lower parallel resistance allows more current to leak from positive to negative terminal which prevents the current to be used in an external circuit, mostly affecting the operational current. The value of R_{sh} is mainly affected by quality of solar cell manufacturing and should be maximised. Figure 2.13 shows the impact of varying values for R_s and R_{sh} on the $J-V$ curve.

Multi-junction devices are represented by a series connection, where each subcell is represented by a circuit shown in figure 2.12 and where the negative terminal of once subcell is connected to the positive terminal of the adjacent subcell. This way, the voltages produces by the individual subcells add, while the current is the same and limited by the subcell generating the least current. The second diode can be considered the 'tunnel diode' and the voltage drop across it, is the voltage loss across the TRJ [30]. Preferably all current flows through this diode, while causing a negligible voltage drop.

2.9. Long-term stability of solar cells

It was noted in 1978 by Staebler and Wronski that amorphous materials exhibit behaviour where the recombination of photo-generated charge carriers emit phonons (heat) which generates meta-stable defects[32].

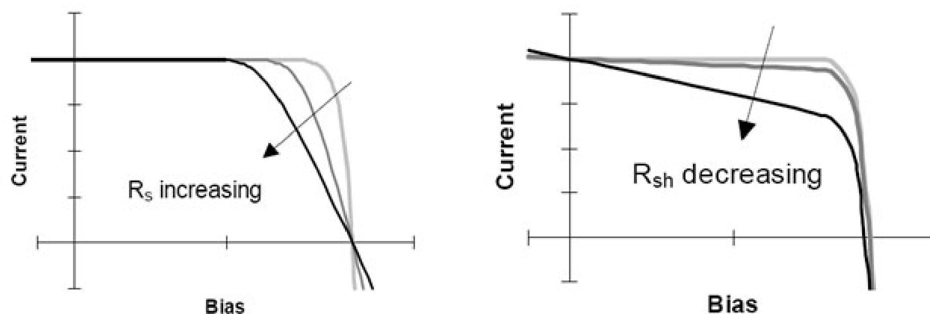

Figure2.13: The effect of R_s and R_{sh} on the $J-V$ curve and thus, FF [31]

Although the Staebler-Wronski (SW) effect is not yet fully understood, the hydrogen collision model appears to present analytic and numerical results that are most in agreement with experiment[33, 34]. This model explains that recombination of light-induced charge carriers breaks the Si-H bonds and releases the mobile hydrogen atoms, which is bound more weakly than in a normal Si-H bond, leaving two dangling bonds. The mobile hydrogen breaks Si-Si bonds to form Si-H bonds which reform when the hydrogen atom hops away. The reverse of these events can take place where the hydrogen retakes its place or that of another emitted mobile hydrogen atom, resulting in no net effect. The mobile hydrogen atoms can bind together in an exothermic reaction to form a meta-stable complex leaving two dangling bonds. The dangling bonds function as recombination centres. The deterioration stabilises around 1000h of AM1.5 illumination and can be reversed by thermal annealing at 150°C for several hours[32, 33] causing the reverse reaction to take place. Despite being associated with the presence of hydrogen atoms, the SW effect appears to be suppressed when the hydrogen to silane ratio is high (≈ 1). This is likely caused by the promoted formation of more dense crystal-like structures which do not show degradation in addition to a decrease in number of weak Si-H bonds by the abundance of H_2 [35].

The increased number of recombination centres and decreased conductivity in a degraded cell hamper J_{SC}, V_{OC} and FF. The degree of performance loss by light-induced degradation of a-Si:H solar cells is around 16% and between 30-40% for a-SiGe:H depending on material quality and germanium content [35, 36]. The proposed 3J device in this thesis incorporates an a-Si:H, as well as an a-SiGe:H subcell which both exhibit the SW effect. Although nc-Si:H consists of an amorphous matrix wherein nano crystals are locked, it barely shows degradation under light soaking[37]. Moreover, the SW effect appears to diminish for multi-junction solar cells. Reported stabilised efficiencies only show a relative drop of 18% in efficiency of an a-Si:H/a-SiGe:H/nc-Si:H 3J solar cell. A relative drop in efficiency as low as 7.8% was reported for an a-Si:H/a-SiGe:H/a-SiGe:H 3J device with heavy hydrogen dilution [38]. Less degraded conversion efficiencies can be attained by replacing the a-SiGe:H with yet another nc-Si:H subcell. A 3J with dual nc-Si:H layer structure was reported to have only a 4% relative drop in conversion efficiency [39]. A reason for this is that the photocurrent for multijunction solar cells is much lower than what the individual single-junctions can achieve, which limits shunt resistance losses.

2.10. Photoelectrochemistry

An efficient and straight-forward fashion of producing high energetic gases for large scale energy storage is by means of photoelectrolysis. This is an electrochemical process in which substances of choice are introduced to electrodes, to which, a voltage is applied. If this voltage is sufficient, a reduction reaction will take place at the cathode, where electrons will be consumed, and an oxidation reaction will take place at the anode, where electrons will be produced. This type of reaction of electron exchange are generally abbreviated to redox reactions.

The intended solar cell in this thesis will be designed for operation in photoelectrolysis. The target voltage is determined by the total electrochemical potential difference for the individual half-reactions at each electrode. The electrochemical potential, E^0, of such reactions is determined by the amount of energy required to form the reaction products and the total charge flow according to

$$E^0 = \frac{G}{n_e F}. \tag{2.14}$$

Where G is the Gibbs free energy in kJ/mol, n_e is the stoichiometric coefficient of electrons in the reaction and F is the Faraday constant, or the total charge for a mole of electrons (= 96,485 C/mol). In other words, the electrochemical potential is the amount of work one mole of electrons has to perform to form a certain substance. This depends on the energy required to form that specific substance and the amount of electrons over which the work is divided. For the water splitting, both half reactions depend on the environments pH for the production of either the H^+, or OH^- intermediate species. for an acidic environment the half reaction at both electrodes are given by

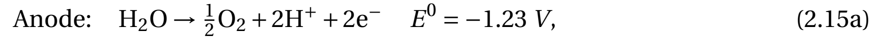

$$\text{Anode:} \quad H_2O \rightarrow \frac{1}{2}O_2 + 2H^+ + 2e^- \qquad E^0 = -1.23\ V, \tag{2.15a}$$

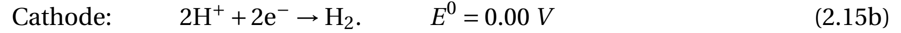

$$\text{Cathode:} \quad 2H^+ + 2e^- \rightarrow H_2. \qquad E^0 = 0.00\ V \tag{2.15b}$$

Which gives the total net reaction:

$$H_2O \rightarrow \frac{1}{2}O_2 + H_2 \tag{2.16}$$

The half-reactions potentials are determined with respect to that of hydrogen. Because hydrogen is set as reference, its electrochemical potential is zero. The anode potential can be calculated by using the required increase in Gibbs energy to split water in its constituent parts (G =237.2 kJ/mol) and number of moles of electrons transferred for every mole of water split (n_e = 2), which gives $E^0 = -1.23$ V, where the minus sign indicates that energy must be supplied to the reaction. The Gibbs energy of formation describes a reversible process; a lossless process in which no entropy is produced. However, the entropy of these reaction products is higher than that of starting material, which means energy is extracted from its surroundings. The more realistic thermoneutral potential incorporates the increase in entropy and gives a potential of E^0=1.48 V. Different electrodes require an additional overpotential to overcome an energy barrier, the activation energy, to start the reaction as illustrated by the $J-V$ curve of an iridium oxide electrode catalysing the oxygen evolution reaction in figure 2.14.

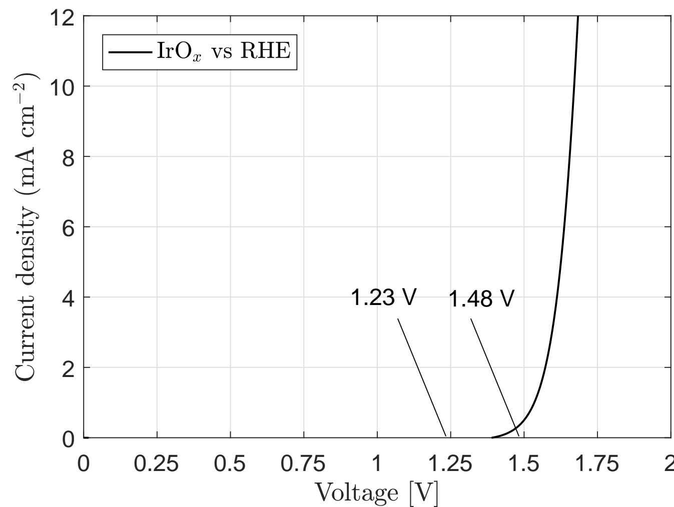

Figure2.14: The J-V characteristic of a water splitting IrO_x electrode

The graph shows the voltage-current density characteristic of a low activation energy IrO_x electrode relative to the reversible hydrogen electrode (RHE). To close the electrical circuit, another electrode, with its own overpotential, is required to catalyse the hydrogen evolution reaction. A solar cell connected to two electrodes behaves like an electrical series connection, where the operational point of the device lies at the intersection of the J-V curves of the eletrodes and the solar cell. The solar-to-fuel efficiency can directly calculated from the photocurrent as this is directly proportional to the amount of gas produced and already includes the solar cell efficiency.

$$\eta_{STF} = \frac{J_{ph} \cdot E^0}{P_{in}} \tag{2.17}$$

gives the solar-to-fuel efficiency, where J_{ph} is the operational current density and P_{in} =1000 W m^{-2} is the input power density for the AM1.5 spectrum. The energy to be extracted from the hydrogen gas is based on the reversible chemical potential $E^0 = -1.23$ V. Operation at a higher voltage, but at the same current density will only contribute to loss mechanisms. The electrochemical potential for splitting CO_2 for fuels or possibly sequestration can be calculated from equation 2.14 and the corresponding half reaction. The most common reactions and their respective electrochemical potentials are as follows and given at pH 7 for aqueous solutions at 1 atm, 298 K and 1 M for the other solutes [40]:

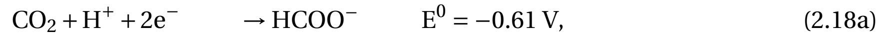

$$CO_2 + H^+ + 2e^- \rightarrow HCOO^- \quad E^0 = -0.61\ V, \tag{2.18a}$$

$$CO_2 + 2H^+ + 2e^- \rightarrow CO + H_2O \quad E^0 = -0.53\ V, \tag{2.18b}$$

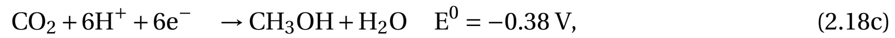

$$CO_2 + 6H^+ + 6e^- \rightarrow CH_3OH + H_2O \quad E^0 = -0.38\ V, \tag{2.18c}$$

$$CO_2 + 8H^+ + 8e^- \rightarrow CH_4 + 2H_2O \quad E^0 = -0.24\ V. \tag{2.18d}$$

Either of these half-reactions could replace the cathodic hydrogen formation reaction from equation 2.15b. This would increase the total electrochemical potential from 1.23 V to 1.47-1.84 V, depending on the reaction products. Because the electrochemical potential for the hydrogen is very similar to, and is kinetically more favourable than the CO_2 reduction reaction, there is a strong rivalry between both reactions. One of the main issues is product selectivity while maintaining electrode stability [41]. Accounting for overpotentials, the required voltage can be between 2.0-2.5 V, depending on the electrodes, solvents and electrolytes used [40].

Photovoltaic water splitting technologies have long struggled with high current densities and electrode stability. Monolithic water splitting devices have achieved η_{STF}= 18.3% for III-V multi-junction photovoltaics [42]. High efficiency silicon-based water splitting devices use three series connected silicon heterojunction solar cells which managed η_{STF}=14.2% [43]. Very recently, a III-V triple junction solar cell was used in combination with SNO_2 coated CuO nanowires as electrodes. This gave the electrodes high selectivity to CO (>80%) as well as stability for several hours [44]. Another work incorporated a four-terminal III-V/Si tandem device with a CuAg cathode and IrO_2 anode to produce more reduced fuels like ethylene, formate and ethanol with an η_{STH} of 5.6% which circumvents further lossy processing steps [45].

In previous work, an a-Si:H/nc-Si:H tandem was processed on a silicon heterojunction (SHJ) cell for the sole purpose of water splitting. SHJ solar cells are a c-Si based technology with thin intrinsic a-si:H layers for passivation. Doped a-Si:H layers in combination with a TCO collect the photo-generated charge carriers. Because of the good passivation quality of the i a-Si:H layers, the dominant surface recombination on an n-type c-Si wafer is reduced and values for V_{OC} > 700 mV are not uncommon for high efficiency single-junction HIT solar cells [22]. The 3J device initially attained a η_{STF} = 2.1%, which was recently improved to 6.2% with V_{OC} = 1.93 V and J_{SC} = 8.5 mA cm^{-2}[46, 47].

3
Methodology

3.1. Processing techniques and equipment

This first section describes the methods, techniques and equipment used to process solar cells. The second subsection will discuss the characterization of their performance. All solar cells processed during this master thesis project were fabricated in the Else Kooi lab of TU Delft. Among the facilities used are a chemical laboratory and a class 10000 clean room of class.

3.1.1. Substrate preparation

Substrates on which the solar cells are to be processed are first cleaned in ultrasonic acetone bath for 15 minutes, then dried with compressed nitrogen and cleaned further in an ultrasonic isopropylalcohol (IPA) bath for 15 minutes. The substrate holders, which are open on the bottom side, are manually cleaned with acetone and IPA to remove particles and possible contaminants.

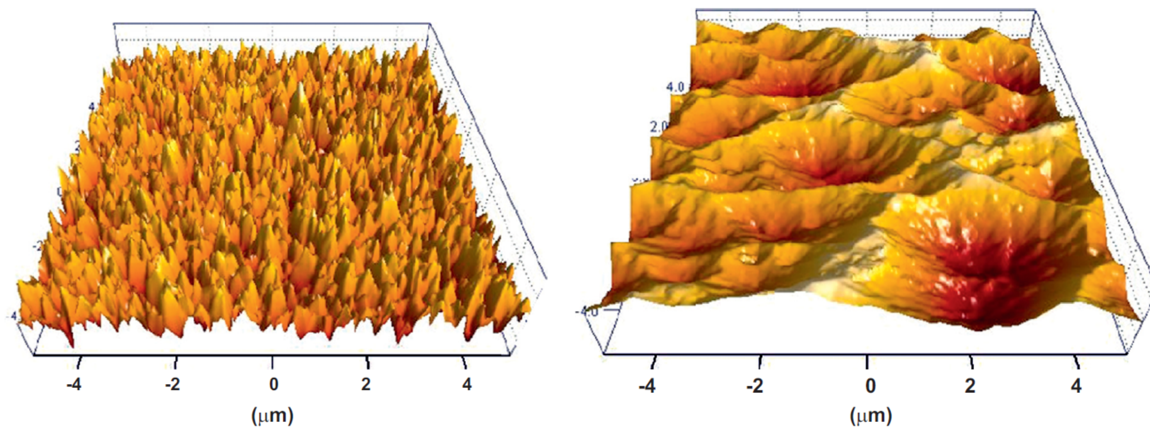

Figure3.1: Surface morphology of the Asahi (left) and AZO (right) textured substrates as imaged by atomic force microscopy [39]

A textured substrate can enhance the generated photocurrent in a solar cell by refracting the light and increasing its path length in the absorber layer(s). In this work, For solar cell manufacturing, two types of textured glass are used. One is commercial Asahi VU, a textured glass strip with SnO_2:F as TCO and a rms roughness of 34 nm. The other uses an in-house developed method of texturing Corning Eagle XG glass with an ZnO:Al (AZO) TCO, which has a rms roughness of 105 nm [49]. The topographies of both textures are shown in figure 3.1. The steep v-shaped features of the Asahi glass have good scattering properties and results in lower coherence of the light, but the features can cause voids in nc-Si:H because of cracks formed as growing crystals collide [39]. Figure 3.2 shows three different textures with however, is too steep and the feature size too small to for the nc-Si:H. The crystals do not follow the surface roughness which can result in voids between layers. Moreover, after the growth of several microns of nc-Si:H, the texture can be completely evened out, which results in loss of light trapping capabilities. Because the proposed 3j device structure

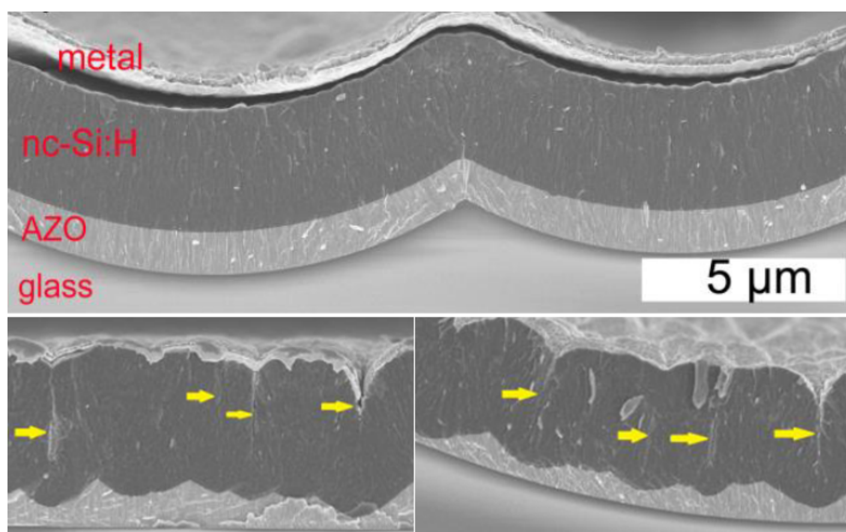

Figure3.2: Defective filaments indicated with yellow arrows in nc-Si:H for textures with different rms roughness. All figures are at the same scale [48]

includes nc-Si:H, solar cells with this absorber layer must use the AZO textured substrates. For quantative analysis of the a-Si:H and a-SiGe:H subcells, the Asahi glass is used since the performance is more consistent due to large scale production and the preparation is less time consuming.

The in-house texturing method uses Corning Eagle XG glass as substrate and an AZO sacrificial layer. The sacrificial AZO is sputtered, which will later be explained in detail, at 200°C, which makes it less dense and more granular than the AZO used as TCO, which has a deposition temperature of 400°C. The crystal grains grow on the glass and obtain a natural roughness. This AZO layer is completely etched off in bath of hydrofluoric acid (HF) (40%) and nitric acid (HNO_3 69.5%) which is mixed in a ratio of 1:3. The AZO dissolves heterogeneously and due to the natural roughness, exposes the glass underneath at different times. The acid further dissolves the glass albeit at a different rate, giving the surface of the glass a roughness [50]. After 50 seconds the AZO layer is completely dissolved, but its features are left embedded on the glass. The glass is then cleaned in demi water for 10 minutes to remove the etchants.

3.1.2. Plasma enhanced chemical vapour deposition

The p, i and n-layers are made using plasma enhanced chemical vapour deposition (PECVD). PECVD is a deposition technique that uses a plasma to provide energy to several precursor gases in a low pressure chamber which dissociate and adsorb to a nearby substrate, as shown in figure 3.3. An alternating current at either radio frequency (RF) of 13.56 MHz, or very high frequency (VHF) at 40 MHz is applied to an electrode while the substrate holder is kept grounded. After ignition of the plasma, electrons are accelerated by the applied electric field between the powered and the grounded electrode, which causes them to collide with the precursor gases which are thereby dissociated, leaving ionised radicals. Because the grounded electrode is kept at lower potential than the RF electrode, positively charged radicals and neutral particles only reach the substrate where they are adsorbed and form the layers on the substrate. Layer materials and properties can be adjusted by varying the precursor gases, their flow rates and thus relative composition, RF power density and the ambient pressure and temperature.

Figure 3.4 shows Amigo, the processing tool used for PECVD by Elettrorava S.p.A. Substrates are placed inside a load lock chamber from which, air can be evacuated. Once the chamber reaches a pressure of around 15-25 mbar, the substrate of choice is transported to one of six other heated vacuum chambers which harbour the electrodes and gas in- and outlets. Different chambers have different gas inlets and are conditioned for specific materials to minimise cross contamination in the chambers. Silane (SiH_4) and hydrogen gas are used for hydrogenated silicon layers (Si:H), where other parameters like, RF power, pressure and temperature govern the growth of an amorphous (a-Si:H) or nanocrystalline structures (nc-Si:H). The hydrogen passivates dangling bonds that remain after nucleation. Adding additional germane gas (GeH_4) produces a silicon-germanium alloy (SiGe:H). A combination of silane and carbon dioxide (CO_2) is used to produce silicon oxides (SiO_x). By varying the silane- germane and the silane-carbon dioxide ratios, certain material properties like

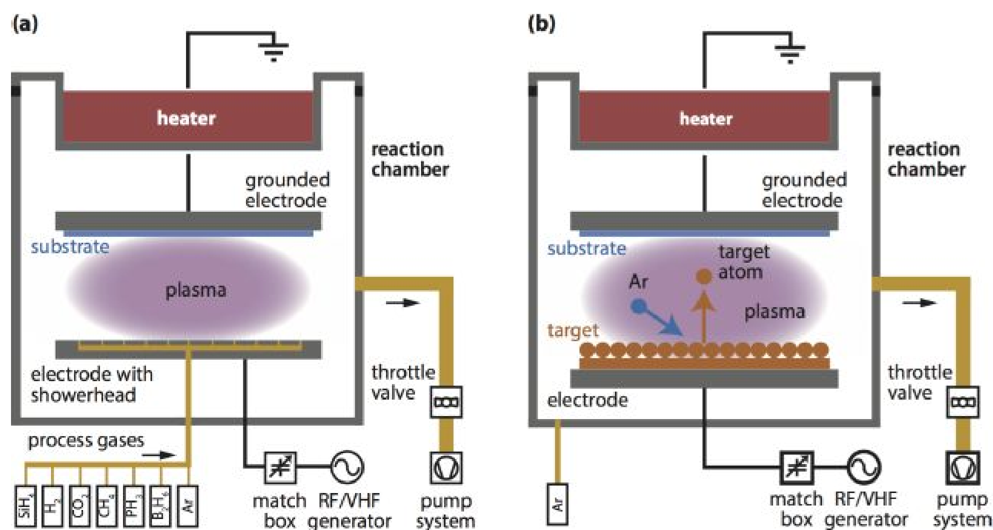

Figure3.3: An illustration showing the working principle of PECVD (a) and sputtering (b) [51]

optical band gap and refractive index can be tuned. Phosphine (PH_3) and diborane (B_2H_6) are used as n- and p-dopants, respectively.

Figure3.4: The Amigo PECVD cluster tool by Elettrorava S.p.A. with the control software running in front

3.1.3. Sputtering

Sputtering is a deposition technique that uses accelerated charged particles to bombard a solid target as shown schematically in figure 3.3. The kinetic energy of the charged particles is dissipated over multiple target atoms in a collision cascade. If the incoming charged particle has sufficient kinetic energy, some of the atoms in the target obtain energy in excess of that of the binding energy, thus ejecting them. The target atoms then diffuse into the vacuum chamber and diffuse towards the nearby substrate where it grows a film of target material.

Amigo has a deposition chamber dedicated to magnetron sputtering, which uses a 13.56 MHz alternating current supplied to the target electrode to produce a magnetic field inside the chamber. The charged par-

ticles are provided by argon gas that is ignited in a plasma. The heavy argon ions are accelerated towards a ceramic ZnO/AlO_3 target (98/2% by weight). The electrons are accelerated away towards the grounded electrode where the substrate is located and act mainly as an agent to ionise other argon atoms to maintain the plasma. In this research, sputtering is used to deposit AZO films that function as transparent conductive oxide and as glass texturing precursor.

3.1.4. Thermal- and electron beam evaporation

Before and after the deposition of the solar cell layers, the respective front and back metal contacts are evaporated onto the substrate. Thermal and electron beam (e-beam) evaporation are used which both rely on evaporating a metal under a low pressure, as illustrated in figure 3.5. The gaseous metal particles adhere to the inside of the chamber by solidifying upon contact. The low pressure ensures the metal vapour is spread throughout the inside of the chamber. Samples are placed in a holder with a shadow mask while facing the evaporating metal and being rotated at a low speed (20 rpm) to provide higher homogeneity of the deposition. E-beam evaporation is a technique that evaporates a target material using a high energy electron beam that is aimed at a target material inside a crucible by means of a magnetic field. Thermal evaporation uses a tungsten evaporation boat which hold the bulk metal. A high current is fed through the evaporation boat which heats up by dissipating some of the current due to its electrical resistance. One may choose one method of evaporation over the other because of high melting point (Cr), alloying behaviour with the tungsten boat (Al) or the emission of potentially harmful UV radiation due to the high energy e-beam (Al). Both evaporation techniques are available in the PROVAC machine by Kurt J. Lesker as available in the EKL laboratory.

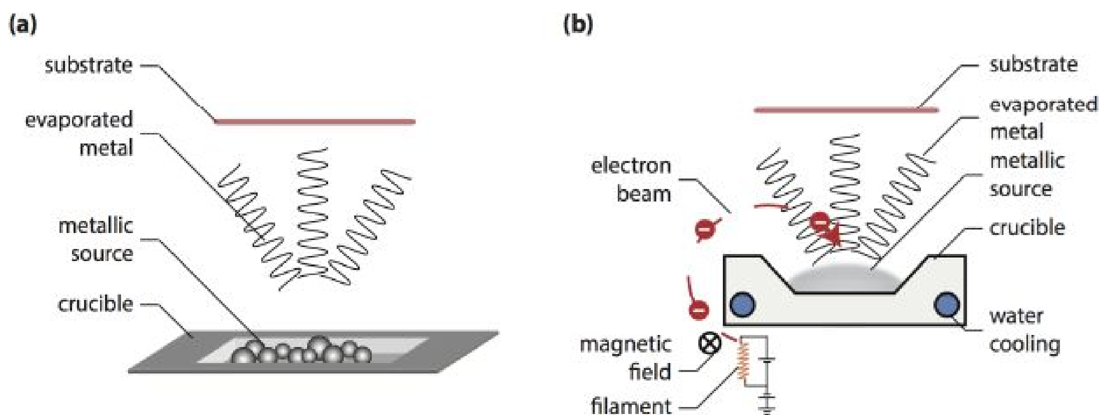

Figure3.5: A schematic representation of a) thermal evaporation and b) e-beam evaporation [52]

For the front contacts, 500 nm Al is used to collect the charge carriers that are transported via the TCO. A mask is used that results in the deposition of a thin stripe along the width of the substrate. The back contact consists of an Ag/Cr/Al stack with thicknesses of 200/30/500 nm, respectively. The Ag layer is thermally evaporated and acts as a back reflector and contact. E-beam evaporation is used for Cr, to increase adhesion between Ag and Al, and Al, which prevents the layers from separating. A mask with 30 4x4 mm^2 squares is used to define the solar cell area. Because the deposition of semiconductor layers is not perfectly homogeneous, the solar cell performance is not identical over the active cell area. By dividing the total area in 30 smaller cells, spots with higher, or lower, performance can be identified that would otherwise have been averaged out. Decreasing the cell active area does reduce the total collected current, but current density (mA cm^{-2}) already takes surface area into account, and the absolute current only has to be large enough to be accurately measured.

3.2. Characterization of solar cell performance

To assess the performance and characteristics of the processed layers or devices, various measurements can be carried out. The used measurement equipment and techniques are described in the sections below.

3.2.1. External quantum efficiency

The EQE set-up with all its components is shown in figure 3.6. The spectral response is determined by illuminating the solar cell with a broad band xenon lamp and selecting specific wavelengths using filters and a monochromator. The measurement beam is chopped at 123 Hz to provide a periodic measurement signal. A lock-in amplifier is used to lock onto the measurement signal and filter out the unchopped noise floor. The set-up measures the electrically generated signal and the actual measurement signal. The time delay between generating and measuring the signal is translated to a phase shift, which is expected to stay constant. Shifts in this phase are indicators for low signal-to-noise ratios which are caused by low spectral response of the solar cell or high intensity light from external sources (sunlight or too high intensity bias light), causing the lock-in amplifier to lock onto an incorrect signal.

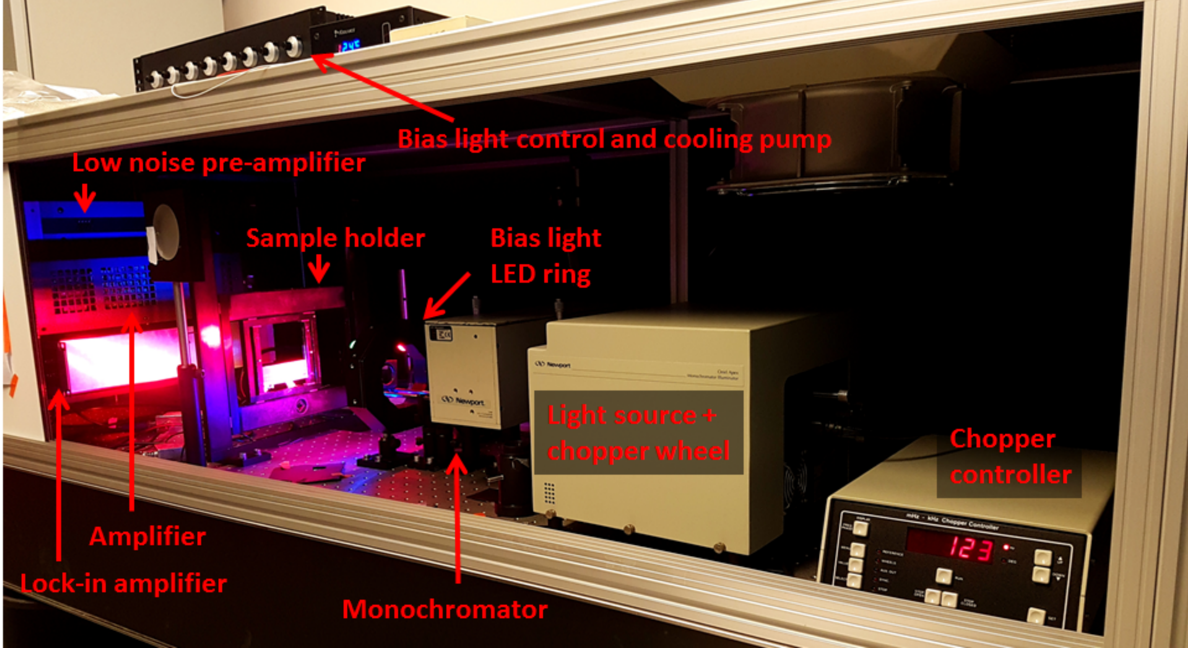

Figure3.6: The EQE set-up with its components as placed in an obscuring enclosure

A silicon calibration diode is used to determine the photon flux of the light source for each wavelength. For each wavelength, the ratio is determined between the generated current of the calibration diode and that of the solar cell. Because the EQE of the calibration diode is known, the EQE of the solar is determined by [18]

$$\mathrm{EQE}(\lambda) = \mathrm{EQE}^{ref}(\lambda) \cdot \frac{I_{ph}}{I_{ph}^{ref}}. \tag{3.1}$$

The software has AM 1.5 spectral data incorporated, which it uses to calculate the illuminated J_{SC} according to [18]:

$$J_{SC} = -q \int_{\lambda_1}^{\lambda_2} \mathrm{EQE}(\lambda) \Phi_{\mathrm{ph},\lambda}^{\mathrm{AM1.5}} d\lambda, \tag{3.2}$$

in which, $\Phi_{\mathrm{ph},\lambda}^{\mathrm{AM1.5}}$ is the wavelength dependent spectral photon flux for the AM1.5 spectrum. Using standardised data of the AM 1.5 spectrum is more accurate than the spectral match of the halogen and xenon lamps which are used in the Wacom set-up to calculate J_{SC}. The presented electrical data therefore uses the J_{SC} as given by the EQE set-up and the solar cell conversion efficiency is scaled accordingly.

Because monochromatic light is used, multi-junction cells only show a spectral response to wavelengths which are absorbed by all subcells, only giving the part of the EQE where the spectral responses of all subcells overlap. To measure the EQE of the individual subcells, bias light is introduced. The set-up features eight coloured LED's which have different spectral output ranging from UV to deep IR as can be seen in figure 3.7. The intensity of individual LED's can be adjusted continuously. One or more of these LED's can saturate a subcell to ensure that the current generated in one subcell by the light coming from the monochromator is

not limited by the lack of current generation in other subcells. This way, the spectral response of the individual subcells can be measured.

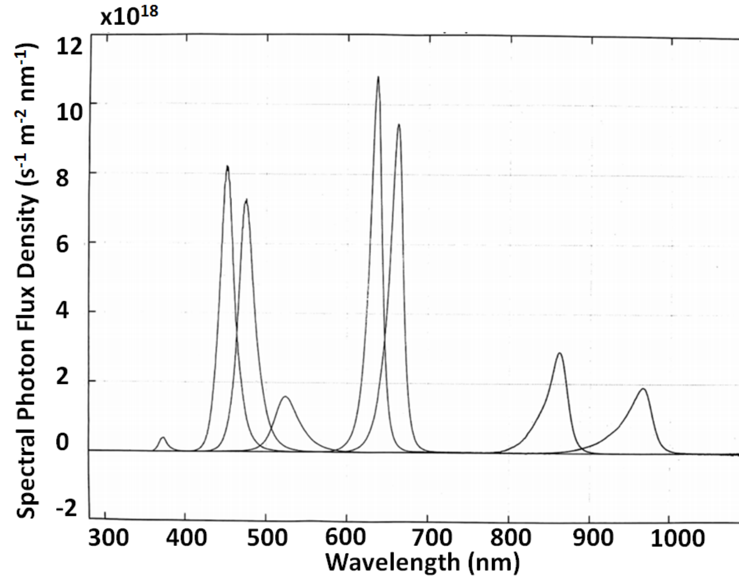

Figure3.7: The spectral output of the eight LED's used to allow the measurement of the spectral response of individual subcells in multi-junction solar cells

Besides bias light, the set-up also features the possibility for measuring under bias voltage. Zero bias voltage represents short-circuit conditions. Measuring under reverse bias increases the electric field across the p-i-n junction, and thus, the drift current and will result in the collection of electrons and holes that would otherwise been inhibited from collection by low carrier mobility. This way, electric bottlenecks become apparent.

3.2.2. $J-V$ curve measurement

The solar cell electrical performance is determined by measuring the cell's illuminated $J-V$ characteristics using a Wacom WXS-90S-L2, class AAA, dual-lamp solar simulator, which is visible in figure 3.8. To verify that measurements are performed under STC, the measurement stage is temperature controlled and the filtered spectral output is calibrated to output 1000 W m^{-2} by means of two mono-crystalline silicon reference cells, which are manufactured by and traceable to the Fraunhofer Institute for Solar Energy Systems. The set-up shines light with perpendicular incidence on a sample while automatically varying a resistive load to traverse the solar cell's J-V curve. From this curve, the J_{SC} and V_{OC} are measured directly at near zero and infinite load, respectively. The FF and conversion efficiency are calculated from the J_{SC}, V_{OC} and P_{max}. R_S and R_{SH} are calculated by extrapolating the trend of the $J-V$ curve near open- and short-circuit conditions, respectively.

3.2.3. Spectrometry

The EQE of a solar cell provides information about the collection of electrons for absorbed photons, but not all light incident on a solar cell is absorbed and not all light that is absorbed generates an electron that is collected. A spectrometer is a device that measures the transmission T and reflection R of light incident on a substrate, which leaves the absorption A to be calculated by equation 2.6. To measure the absorptance and reflectance, a Perkin Elmer Lambda 950 UV/vis spectrometer is used. It harbors a deuterium and a tungsten-halogen lamp for the UV and visible+IR spectral ranges. A monochromator is used in combination with filters to select wavelengths and filters remove high order noise. Measurements are performed in the wavelength range from 300 up to 1200 nm, which corresponds to the spectral response range of (μ)c-Si:H. A reference- and a measurement beam are guided to an integrating sphere, which is coated with a highly reflecting material. Substrates can be placed either before the measurement beam enters the sphere, or at the back of the sphere, from where it is scattered back into the sphere's cavity to measure transmittance and reflectance, respectively. Two photodiodes integrate the measurement signal from wavelength ranges of 300-800 nm and

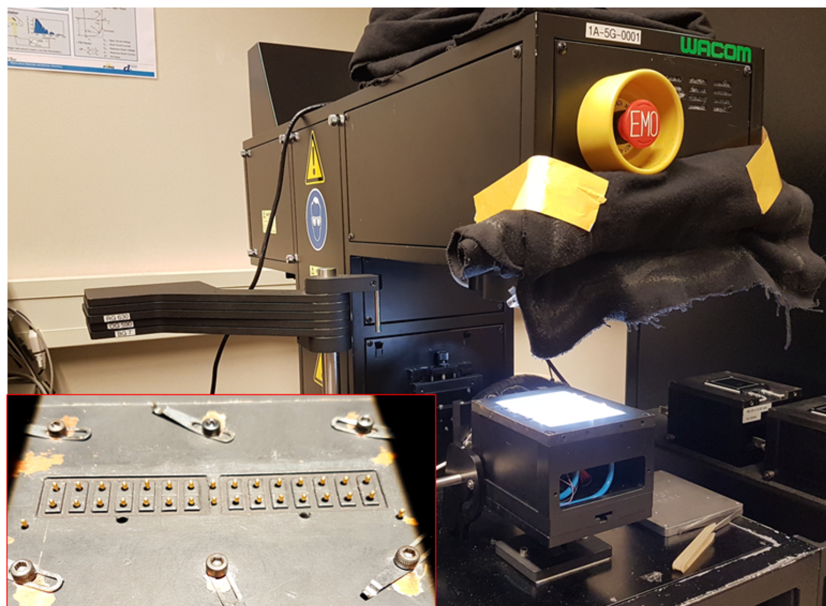

Figure3.8: The Wacom solar simulator with visible light output. The inlay shows a front view of the measurement chuck used for the thin-film solar cell stripes with 30 individual dots

800-1200 nm respectively. Throughout this thesis, the assumption of $T = 0$ is made for solar cell devices because of the 730 nm of metal for the backside. Although the absortances of the Asahi VU and Corning Eagle XG glass substrates are neglected, it is useful to note that the values for both substrates are constant throughout almost the entire relevant wavelength range and are roughly 1-2% [53].

3.2.4. Spectroscopic ellipsometry

Spectroscopic ellipsometry (SE) is a measurement technique that relies on measuring the phase and amplitude of the p- and s- polarizations (parallel and perpendicular) of light reflected of a sample. Samples are usually thin films deposited on a substrate. It then uses models to compare these parameters to obtain material properties such as, but not limited to: refractive index (n), extinction coefficient (k), film thickness, roughness and optical bandgap. The SE measurement equipment used during this thesis is an A M-2000 Ellipsometer manufactured by J.A. Woollam Co.

3.2.5. Light soaking

A widespread means of quantifying the SW effect is by exposing solar cells to light of STC intensity and spectrum for extended periods of time, also known as light soaking. The used light soaking set-up is shown in figure 3.9. It incorporates a chamber with mirrored walls and six halogen lamps in its ceiling. Solar cells are laid flat under the lamps and are illuminated for a period of 1000 hours. The cell degradation is measured by periodically taking the solar cells out from under the set-up and measuring the $J-V$ curve. To make sure the cells start with a representative baseline, they are first thermally annealed by putting them into a laboratory oven at 130°C for one hour to minimise the defect density of the material. Cells are measured twice at each time interval to improve reliability.

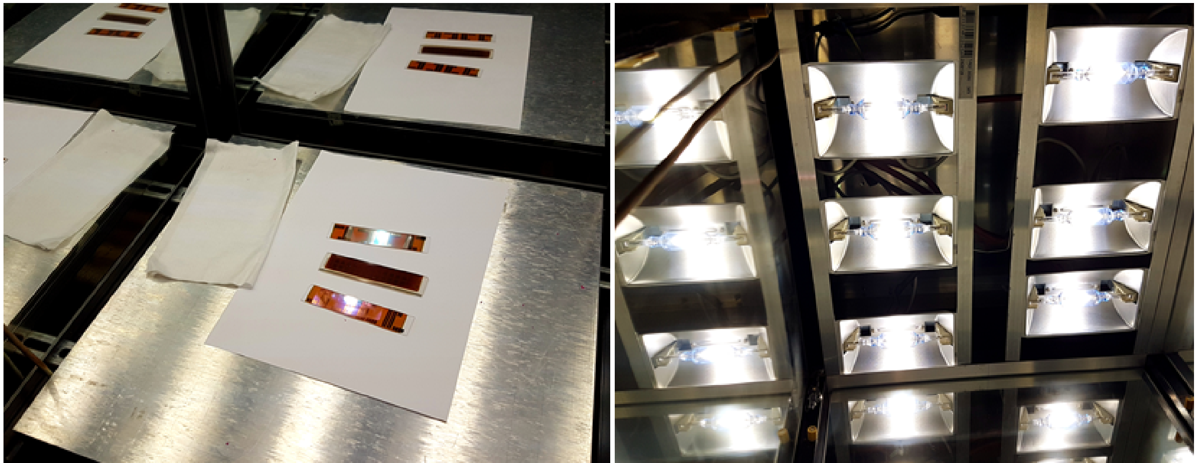

Figure3.9: The LID set-up with mirrored wall. Left: Three samples are subdued to light soaking. Right: The six halogen lamps

4

Results and Discussion

The performance of various (layers) and devices are presented in this chapter. First, the optimisation and characterization of the a-SiGe:H SJ device is presented. Afterwards a benchmark is laid out for the multi-junction devices by presenting the SJ performance on the relevant superstrate which is followed by the performance of the two tandem devices. Here, the focus will lie on finding the optimum interface layer between the top/middle and middle/bottom SJ devices. The findings in the previous sections will form the foundation of a high performance triple junction device presented afterwards. The final section of this chapter mentions the stability of the a-SiGe:H subcell and the expected long-term stability for a 3J device. It is good to note that all samples presented in this chapter were processed over the course of eight months. Within this time period, the processing tools went through several cleanings, calibrations, repairs and/or replacement parts, each of which affecting the deposition parameters. The processed devices (especially those using non-optimised materials, like a-SiGe:H), suffer from performance fluctuations because of these events. Certain devices and their performance are only compared with devices of similar structure processed over a short time span. That is, within several hours, up to several days, in which, the processing tools are assumed to perform identically.

All solar cells were processed on stripes where the back contacts define 30 individual cells, or dots. Reported performance of solar cells with different structures is based on the best 5 dots out of 30 per stripe based on efficiency, unless stated otherwise.

4.1. a-SiGe:H single-junction device

The development of the a-Si:H and nc-Si:H subcells is quite mature within this research group and have reached very impressive results with a so-called micromorph, a-Si:H/nc-Si:H tandem device with an initial efficiency of 14.8% [14]. The a-SiGe:H subcell is less extensively studied in our research group and it is therefore investigated most thoroughly in this work because the most gains are to be made in this subcell. Some investigated factors are buffer layers between the doped and intrinsic layer and the (graded) absorber layer(s) and the intrinsic layer thickness.

In order to obtain a baseline structure, a cell structure from previous work was reproduced, along with a small variation in structure that incorporated a 5 nm a-Si:H buffer layer between the p-layer and i-layer. The performance of these cells is presented in table 4.1. The added buffer layer showed an increase in performance and was therefore chosen as a baseline for most experiments. Its detailed cell structure is shown in figure 4.1.

Table4.1: The external parameters of a reference a-SiGe:H solar cells and one with an added 5 nm a-Si:H buffer at the p/i interface

Cell	V_{OC} (mV)	J_{SC} (mA cm^{-2})	FF (-)	η (%)
Reference	705	17.1	0.67	8.1
5 nm a-Si:H p/i buffer	709	17.4	0.67	8.2

The solar cell uses a p-i-n superstrate configuration deposited on the Asahi VU with FTO as TCO for single-junction experiments, or Corning Eagle XG glass with AZO as TCO when assessing multi-junction performance. To prevent reduction of the FTO TCO by the hydrogen rich plasma that is present during p-layer

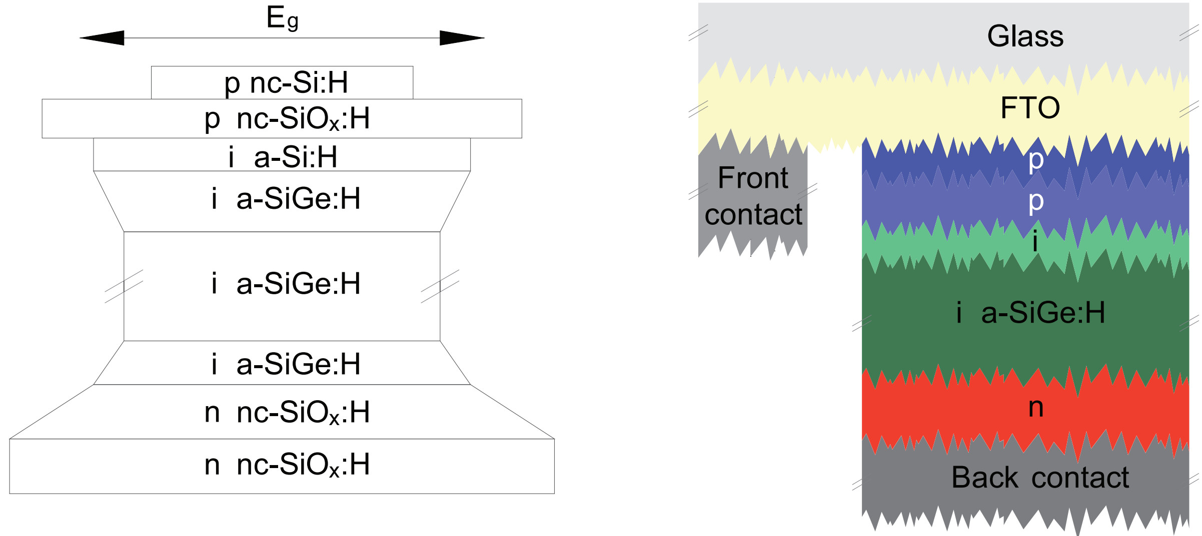

Figure4.1: A schematic bandgap profile (left) and the baseline structure (right) of the a-SiGe:H single-junction device

deposition, a thin AZO layer ($d \approx 30$ nm) is deposited on the TCO for protection [54]. The device harbors a thin (2 nm) p-type nc-Si:H layer that has low activation energy and produces a good ohmic contact with the front TCO, while acting as a seed for the nucleation for the thicker (16 nm) p-type nc-SiO_x:H layer. Parasitic absorption is minimised by the thin p-type nc-Si:H layer and high optical bandgap of the p-type nc-SiO_x:H layer.

To enhance charge collection, the bandgap of the intrinsic a-SiGe:H material has graded germanium content to create a U-profile [55]. The layer starts and ends as intrinsic a-Si:H and has germanium content, subsequently, increasing over 30 nm, constant over 30-90 nm and decreasing over 20 nm. When altering the intrinsic layer thickness, only the middle part with constant germanium content is varied in thickness. The solar cells presented in table 4.1 use a total intrinsic layer thickness of 80 nm. Furthermore, the device has a double nc-SiO_x:H n-layer with a thickness of 50 nm. The first half starts with oxygen grading that starts at zero and increases linearly to match that of the second half of the layer. The function of this graded n-layer is to provide a smooth bandgap transition without the need for an additional buffer layer [26]. Finally the back contact consists of the standard 200 nm/35 nm/500 nm Ag/Cr/Al metal stack as a back reflector and back contact. It is expected that a further gains are to be made by adjusting the thicknesses of the graded layers and buffer layers at the p/i and i/n interfaces. A more extensive study on the buffer and graded layers is presented in section 4.1.2.

The main advantage of using nc SiO_x:H for the doped layers is its wide bandgap (>1.85 eV) while maintaining low absorption. Moreover, the conducting nano-sized crystals grow perpendicular to the superstrate in an amorphous matrix, providing high tranversal and low lateral conductivity, both of which are advantageous for solar cell performance. Higher oxygen content in SiO_x increases the optical bandgap and lowers the refractive index. In an attempt to enhance the blue response of the a-SiGe:H solar cell, initial experiments were performed by adapting the p-type window layer. The progress so far is presented appendix A. One of the preliminary findings is that replacing the standard double p-layer with a high/low E_g p-type nc-SiO_x:H configuration can increase the blue response of an a-SiGe:H solar cell, but it did not result in a net benefit in terms electrical performance. Moreover, in a multi-junction configuration, enhanced blue response is more relevant for the a-Si:H top cell. .

4.1.1. a-SiGe:H intrinsic layer thickness

For usage in multi-junction purposes, increasing the absorber layer thickness usually increases the absorption of photons with longer wavelengths. For a-SiGe:H it is known that the cells performance is affected by the intrinsic layer thickness [26, 39]. This is mainly caused by the a large defect density that is associated with the a-SiGe:H material and adding more materials results in more defects.

A thickness series was performed with intrinsic layer thickness ranging from 80-200 nm in increments of 40 nm deposited at 28 mW cm^{-2} forward RF power. This includes the graded layers of increasing and decreasing Ge content. The results are presented in table 4.2.

Table4.2: The external parameters of a-SiGe:H solar cells with different intrinsic layer thickness. The sample marked with * was processed in a separate batch. T

Intrinsic layer thickness	V_{OC} (mV)	J_{SC} (mA cm^{-2})	FF (-)	η (%)
80 nm	719	17.2	0.63	7.85
120 nm	692	18.5	0.60	7.68
160 nm	684	18.8	0.59	7.62
200 nm*	672	17.9	0.49	5.93

An almost linear trend is observed in V_{OC} and FF of decreasing performance with increasing intrinsic layer thickness. The J_{SC} shows an optimum around 160 nm a-SiGe:H thickness. The EQE graphs of the 80/120/160 nm cells are presented in figure 4.2 and show decreasing the thickness of the intrinsic a-SiGe:H layer shows a shift in the peak of the EQE graph to lower wavelengths. Thicker layers give longer wavelength photons a higher probability of absorption.

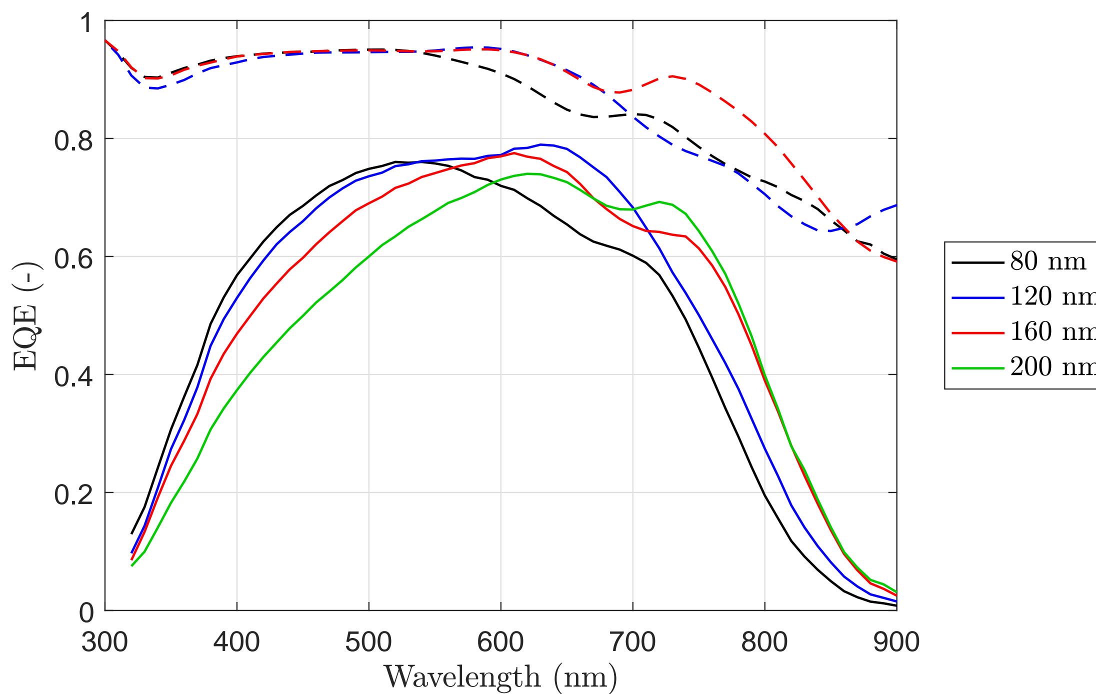

Figure4.2: EQE and 1-R of a-SiGe:H SJs with increasing intrinsic layer thickness of 80-200 nm in 40 nm increments

The reflectance of all devices are nearly identical for wavelengths up to approximately 550 nm. This shows that increase in blue light response with thinner absorber layers is not an optical, but by an electrical effect. Shorter wavelength light is, in fact, absorbed, but the charge carriers it generates are not collected with thicker absorber layers. The short wavelength photons enter through the p layer and are absorbed in the first nanometers of the absorber material. The generated hole is forced back to the p layer by the electric field where it will be collected by the TCO and front contact. The electron, on the other hand, has to traverse the absorber layer before being collected at the back metal contact. This effect occurs between layer thicknesses of 120 nm and 160 nm as there is nearly no loss of blue response in the 120 nm sample with respect to the 80 nm sample. The same effect also prevents holes generated in the additional thickness to be collected to an even larger extent, because of the lower mobility of holes with respect to electrons in the a-SiGe:H bulk. The observed increase in deep red absorption is because these photons are absorbed on the second pass after being reflected off the silver back contact, closer to the p-layer. The increase in infra-red absorption reaches a saturation point around the bandgap absorption edge, the wavelength range for which the absorption coefficient decreases dramatically. Increasing the electric field across the intrinsic layer has the potential to reduce

the non-collection of photo-generated carriers. This is most commonly achieved by increasing the dopant concentration in the doped layers or decreasing the intrinsic layer thickness. However, large doping concentration results in higher recombination and therefore, lower collection of charge carriers. A second batch was processed in an attempt to find the optimum thickness in terms of electrical performance and optical response regarding multi-junction operation. The Amigo PECVD cluster tool required maintenance and the accompanying re-calibration, which revealed the sub-optimised deposition parameters prior to the maintenance. The new parameters showed an almost doubled deposition rate, causing a more defective absorber layer with lower V_{OC} and J_{SC} as well as a shift in optical response. The trends in external parameters of the total thickness series are shown in figure 4.3.

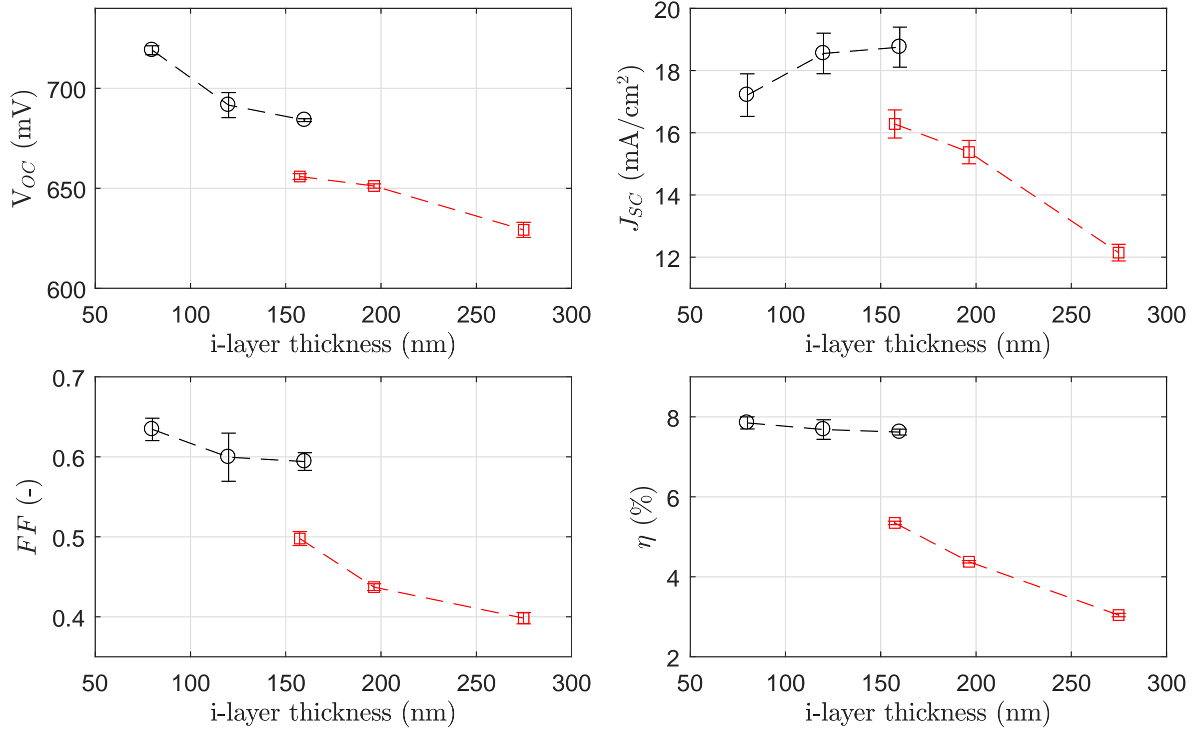

Figure4.3: a-SiGe:H SJ external parameters as function of intrinsic layer thickness. Different colors and markers indicate different batches. The given error bars are the standard error; Values for J_{SC} are based on a single EQE measurement

The intrinsic layer thicknesses of the second batch were determined in retrospect and show a jump in performance with respect to the initial batch. It is clear that without further adjustment of the deposition parameters, an increase in deposition rate has a detrimental effect on all external parameters. This is because the radicals have little time to form a stable and dense structure which leads to voids and lower conductivity of the material [56]. Additionally, High deposition rates by just increasing power density leads to more ion damage and increases polyhydrides (SiH_x) concentration in the bulk which has shown detrimental to the amorphous layer quality as less bonds are available for Si-Si or Si-Ge bonds [57]. The jump in performance is the manifestation of the decrease in material quality. Similar trends can be observed, but the

4.1.2. Buffer layers and grading

For a-SiGe:H solar cells, it is a common practice to grade the germanium content of the intrinsic layer and/or to include buffer layers between the intrinsic- and both doped layers. The main objective of these techniques is to smooth the bandgap energy transition between the narrow-gap absorber and wide-gap doped layers. This redistributes the space charges near the p/i and i/n interfaces which smooths the electric field and enhances the otherwise limited charge collection in the defective a-SiGe:H bulk material [29, 58].

Small variations were performed on the standard structure, which included a 5 nm a-Si:H p/i buffer, as presented at the start of this chapter to further improve on this device's performance. To achieve this, two distinct series of a-SiGe:H solar cells were processed. One where the thickness of the graded layers was increased and a second in which a constant bandgap a-Si:H buffer layer between either the p- and i-layer or i- and n-layer was added or made thicker. The thicknesses of the a-SiGe:H layers in the reference cell are 28 nm,

72 nm and 20 nm for the layers with increasing, constant and decreasing germanium content, respectively. The rest of the cell structure was kept the same. The performance of the different structures is shown in table 4.3, which includes the number of working dots out of 30 dots per stripe as reliability of subcells is an important parameter for more complex, multi-juntion structures. Here, a dot is considered working if it has at least 75% of the average performance of the best five dots on the stripe in terms of conversion efficiency. A minimum layer thickness increment of 5 nm was chosen to ensure reproducibility.

Table4.3: External parameters of U-profiled a-SiGe:H single-junction solar cells with different thickness of graded layers, as well as different a-Si:H buffer layers at the p/i and i/n interfaces. The change in layer thickness relative to the reference is indicated in brackets. Dots are considered working with performance ≥75% of the average of the best 5 dots in terms of efficiency. Best values are highlighted with a bold typeface

Cell	p/i grading	i/n grading	V_{OC} (mV)	J_{SC} (mA cm^{-2})	FF (-)	η (%)	# Working
Reference	28 nm	20 nm	645	**16.7**	0.50	5.4	**21**
G50	33 nm (+5)	20 nm (+0)	649	**16.7**	0.52	**5.7**	6
G05	28 nm (+0)	25 nm (+5)	**654**	16.4	**0.53**	**5.7**	15
G55	33 nm (+5)	25 nm (+5)	**654**	16.4	0.48	5.1	18
Cell	**p/i buffer**	**i/n buffer**	**V_{OC} (mV)**	**J_{SC} (mA cm^{-2})**	**FF (-)**	**η (%)**	**# Working**
Reference	5 nm	0 nm	645	**16.7**	0.50	5.4	21
B05	5 nm	5 nm	660	**16.7**	**0.56**	**6.2**	10
B50	10 nm	0 nm	**661**	16.5	0.51	5.6	**22**

Increased the thickness of the graded layer effectively decreases the slope of its bandgap energy. Increasing the p/i graded layer thickness shows improvement of all external parameters, but does show a high number of defective, shunted dots. Increased grading at the i/n interface shows similar performance gain, but this time in favour of V_{OC} and FF rather than J_{SC}. The tradeoff lead to the same conversion efficiency for either thicker graded layer. Increased non-absorption at the i/n interface due to the thicker, wider bandgap absorber material is unlikely to cause the decrease of J_{SC}. With a total intrinsic layer thickness of 125 nm, the absorption of above bandgap photons is not yet saturated. Enhanced recombination due to an addition of non-absorbing material would also be observed in FF and V_{OC}, which show the opposite. EQE measurements of various dots within the same cell show approximately the same deviation as the presented difference in J_{SC} of G50 and G05. Although G55 shows the same increase in V_{OC} as G05, the J_{SC} and especially FF keep its performance low.

The buffer layers appear to have a larger impact on performance. Adding a 5 nm a-Si:H buffer at the i/n interface provides the largest increase in performance, but also a large drop in working dots. Adding 5 nm to the p/i buffer improves the performance the most in therms of V_{OC}, but suffers a loss in J_{SC} that results in a slight increase of conversion efficiency.

Experimental and simulated results show that grading of the a-SiGe:H intrinsic layer is essential and that the thickness of the graded layer at the p/i interface should be as thin as possible, while that at the i/n interface should be as large as possible to enhance efficiency [59]. Despite this knowledge, the best performing a-SiGe:H solar cell structure developed in our group has thick p/i grading and thinner i/n grading. To examine a worst case scenario, one research group applied a reverse grading profile, with high germanium content at the p/i and i/n interface. It was found that given a certain buffer thickness, the profile appeared irrelevant [60]. The overall consensus seems to be that U-profile grading or slight adaptations thereof improve a-SiGe:H SJ performance [29, 61, 62]

Although effort was made to manufacture reproducible structures, it was observed that solar cells with identical structure processed within 48h of each other showed larger variation in performance than devices with different structures. This fluctuation in performance was noticed multiple times, which gives the impression that the scope of these experiments is too small to draw qualitative conclusions. Most a-SiGe:H solar cells produced in this series show that increased grading or buffer thickness improves performance. Of which, the a-Si:H buffer show the largest boost. Further experiments are need to conclusively determine what the ideal combination of buffer and graded layer thickness must be.

4.2. Light induced degradation

The solar cell conversion efficiencies reported in this work are the initial values. As time goes on, the materials that make up the solar cell deteriorate, diminishing its performance. Amorphous materials are notorious for a specific type of degradation, which is caused by absorbed light and is known as the SW effect, as discussed in section 2.9. The operational point for a chemical fuel producing solar cell with certain counter electrodes is at the intersection of their $J-V$ curves. For systems that produce one type of fuel at each electrode, this operational point is preferably as close as possible to the MPP of the solar cell. The voltage/current characteristic of both the solar cell and electrode are very steep in this region where a small change in operational voltage can have significant impact on η_{STH}. When manufacturing a practical device, the stability of the solar cells should be taken into account, especially with multiple amorphous intrinsic absorber layers.

To investigate the feasibility of the proposed 3J device in a long-term operating water splitting/CO_2 reduction prototype, two a-SiGe:H SJ devices were submitted for a light soaking test, where they are exposed to STC for approximately 1000 h. As a representative baseline, the cells were first annealed for one hour at 130°C, which is deemed sufficient as the cells have only been exposed to ambient light for several hours. Stabilised cells, which occurs after 1000 h of light soaking, need up to several hours of annealing at 200°C to fully reverse the SW effect [63].

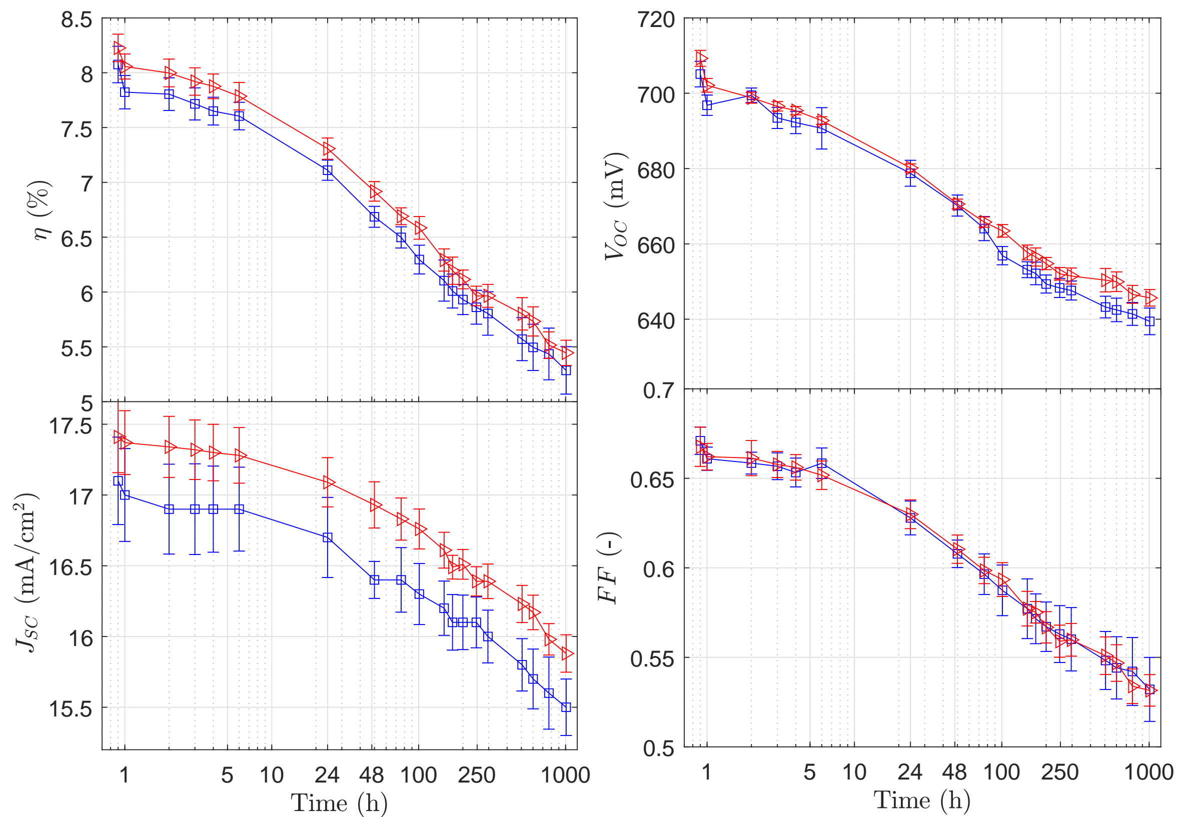

Figure4.4: The change in external parameters in time due to LID of an a-SiGe:H cell without (blue □) and with buffer layer (red ▷)

Figure 4.4 shows the external parameters of two a-SiGe:H SJ solar cells in time during the light soaking experiment. The solar cells used during this experiment are the same samples as presented in table 4.1, which determined the initial baseline at the beginning of the chapter. The structure of the reference is taken from previous work and the other cell includes a 5 nm a-Si:H buffer layer at the p/i interface. The results are obtained by periodically measuring the $J-V$ curves of both solar cells and averaging the performance of the consistently best performing 7-10 dots (out of 30). The results of two $J-V$ sweeps are averaged to obtain the data per time stamp as misalignment of the measurement chuck sometimes causes the measurement of certain dots to fail. The positive and negative error bars are positioned at $\pm 1\ \sigma$ from the average value.

Both cells show the same trends where the efficiency falls off rapidly in the first ten hours. After which, the efficiency declines at a lower rate. After 1000h of light soaking the deterioration stabilises and V_{OC} was

measured to show a relative degradation of only 0.01% per hour.

After 1000 hours of illumination, the relative drop in efficiency is 35% for the reference cell and 34% for the cell with buffer layer. The trade off between better charge collection, leading to less recombination events that cause LID, and the addition of more amorphous material seems to result in a slight benefit for the solar cell including the buffer layer. The results of the external parameters after 1000h of light soaking are summarised in table 4.4.

Table4.4: The absolute and relative drop in external parameters of two a-SiGe:H SJ solar cells after 1000 hours of light soaking

Cell	Measured	η (%)	V_{OC} (mV)	J_{SC} (mA cm^{-2})	FF (-)	R_s (Ω cm^2)	R_{sh} (Ω cm^2)
Reference	Initial	8.1	705	17.1	0.67	4.32	778
	Degraded	5.3	639	15.5	0.53	7.24	272
	Absolute change	-2.8	-66	-1.5	-0.14	-2.91	+506
	Relative change	-35 %	-9.3 %	-9.0 %	-21 %	-67%	+65%
p/i buffer	Initial	8.2	709	17.4	0.67	4.12	703
	Degraded	5.4	646	15.9	0.53	6.81	274
	Absolute change	-2.8	-63	-1.5	-0.14	-2.68	+429
	Relative change	-34 %	-9.0 %	-8.6 %	-20 %	-65%	+61%

Both cells show almost identical trends for each parameter. Where the relative degradation in V_{OC} and J_{SC} is around 9% for both cells, most degradation is seen in FF with over 20% relative decrease. Of which, the contribution of increase in series resistance is slightly larger than the decrease of shunt resistance. This results in a large shift of its MPP as the loss in FF is super imposed over the loss in V_{OC} and J_{SC}. The combined loss in the aforementioned parameters cause the efficiency to drop with approximately 35%, relatively. Figure 4.5 shows the initial and degraded $J-V$ curves of the p/i buffer a-SiGe:H solar cell based on a single dot, but with scaled current density.

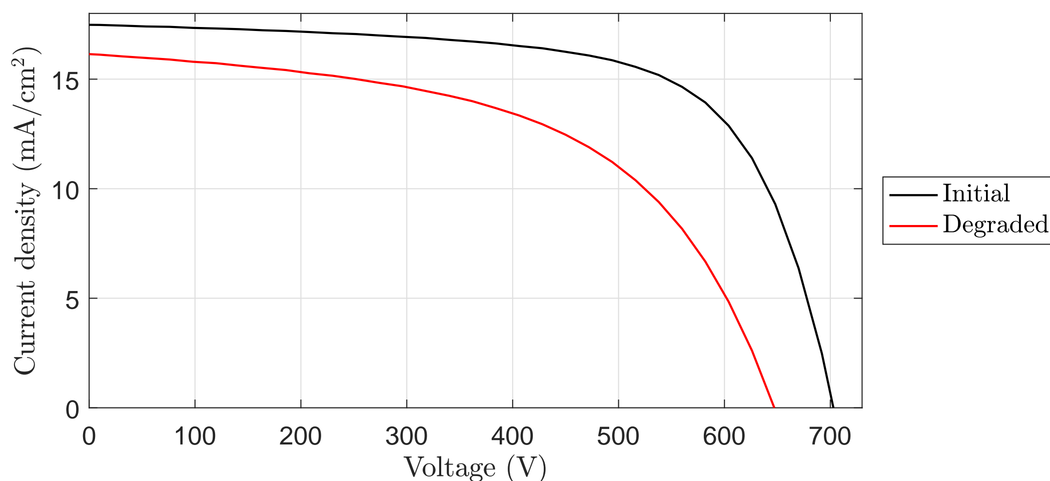

Figure4.5: $J-V$ curves of the a-SiGe:H solar cell with buffer layer after annealing and after 1000h of light soaking

Although the long-term degradation of the multi-junction devices was not measured, it is expected for the a-SiGe:H subcell to show less degradation in the multi-junction configuration as the a-Si:H top cell filters part the light. Not because high energy photons cause damage, as the SW effect was shown independent of photon energy in amorphous silicon [63], but because the total photon flux in the a-SiGe:H cell is reduced and therefore also recombination of photo-generated charge carriers.

4.3. Single-junction performance on an AZO superstrate

To put the multi-junction device performance in perspective, the single-junction devices are fabricated on the same AZO superstrate as the intended 3J device. The general structure of the a-Si:H and nc-Si:H subcells is very similar to the a-SiGe:H cell structure and is shown in figure 4.6.

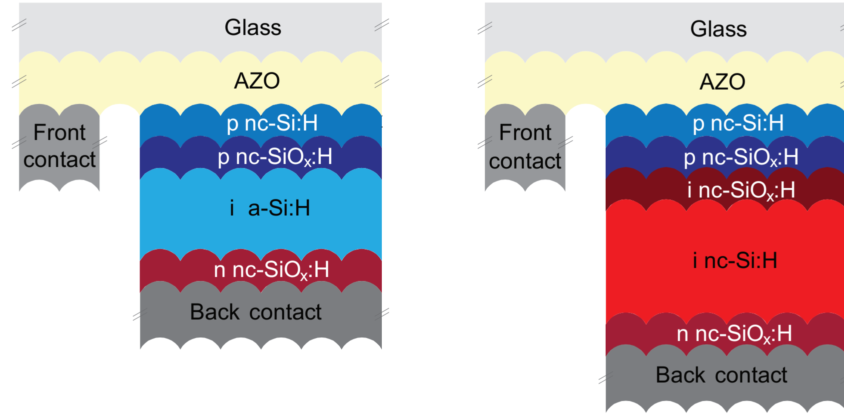

Figure4.6: Schematic structure of the a-Si:H (left) and nc-Si:H (right) single-junction solar cells on an textured glass superstrate with AZO as TCO

The double nc-Si:H/nc-SiO$_x$:H p-layer is identical for all SJs to that from the a-SiGe:H which provides good conductivity and transparency. The nc-Si:H SJ has an intrinsic SiO$_x$:H buffer layer to prevent diffusion from boron into the bulk. The total intrinsic layer thicknesses of the baseline SJ devices are 200 nm, 120 nm and 2800 nm for the respective a-Si:H, a-SiGe:H and nc-Si:H SJs, with corresponding optical bandgaps of 1.73 eV, 1.45 eV and 1.12. These bandgaps are determined by SE measurements and base their values of a Tauc plot. The a-Si:H and nc-Si:H SJs have the same 50 nm SiO$_x$ non-graded n-layer and all cells have the standard Ag/Cr/Al back contact with thicknesses of 200/30/500 nm respectively. The external parameters of the three SJ devices on the AZO superstrate are summarised in table 4.5. As reference, the SJ performance of similar structured solar cells deposited on textured glass with AZO, as manufactured by LG Electronics are given that. The resulting 3J structure of these SJ devices result in a near world record 3J initial conversion efficiency of 16.1% [39].

Table4.5: The external parameters of the a-Si:H, a-SiGe:H and nc-Si:H SJ subcells on an AZO superstrate compared to SJs used in a similar structure with a 3J device efficiency of 16.1%

Manufactured	Cell	V_{OC} (mV)	J_{SC} (mA cm^{-2})	FF (-)	η (%)
This work	a-Si:H	861	10.7	0.66	6.10
	a-SiGe:H	663	13.6	0.53	4.75
	nc-Si:H	497	24.0	0.65	7.69
LG [39]	a-Si:H	1021	15.3	0.73	11.4
	a-SiGe:H	746	22.9	0.66	11.2
	nc-Si:H	540	26.1	0.73	10.4

Despite being improvements with regards to recent previous work [46, 47], all SJs lack approximately 10% in performance on all fronts with respect to those reported by similar cell structures reported by LG electronics and United Solar [39, 64]. The most notable differences are in the V_{OC} and J_{SC} of the a-Si:H and a-SiGe:H subcells, with approximately 150 mV and 80 mV lower V_{OC}, respectively. Because of nearly identical optical bandgaps to the reported work, the difference in V_{OC} for the a-Si:H cell is attributed to sub-optimal deposition conditions, like RF power in-coupling and deposition rate. Moreover, less recent work within this research group has shown $V_{OC} > 1$ V for a-Si:H SJ devices [65]. Over the course of time, deposition conditions gradually change for a PECVD cluster tool by general usage and maintenance. Producing consistent high performing a-Si:H solar cells requires considerable effort to optimise the interplay of all deposition parameters, which has not been prioritised throughout the years, which has caused the performance to decline. The much lower J_{SC} of this subcell ($\approx$ 4 mA cm^{-2}) is mostly due to a thinner absorber layer (200 nm vs 300 nm).

The lower thickness of the a-Si:H intrinsic layer was chosen to get a more accurate estimation of the behaviour within the 3J device. With the listed SJ values, an upper limit for open circuit voltage is approximately V_{OC} =2.021 V.

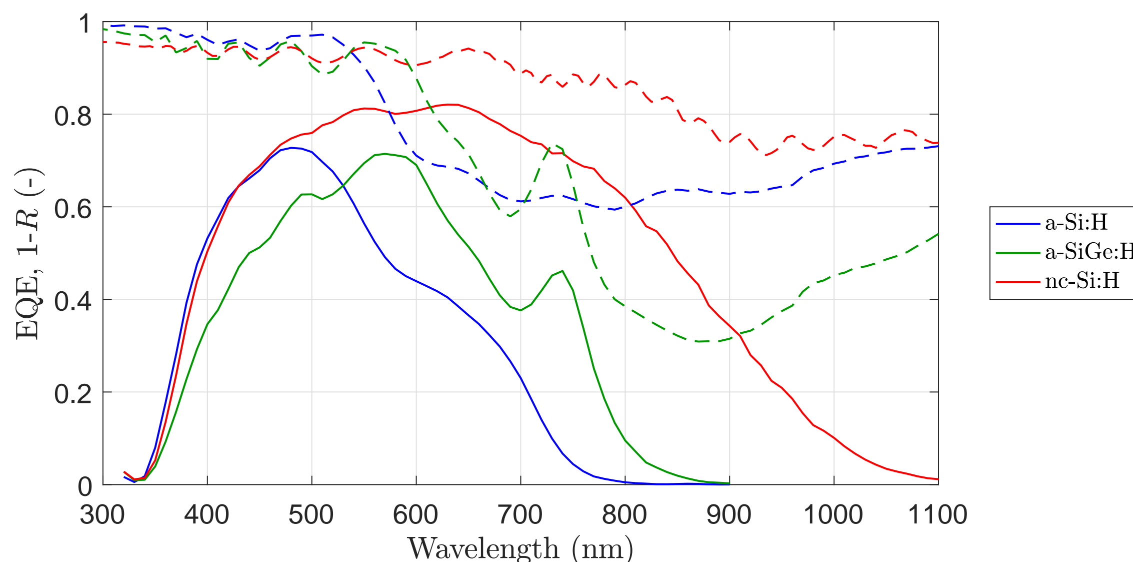

Figure4.7: The EQE and 1-R of the a-Si:H, a-SiGe:H and nc-Si:H SJ devices on an AZO superstrate

Lower performance of the a-SiGe:H subcell is partly because when developing this SJ device, its performance still left room for improvement, but it is mainly due to an unintentional increase in absorber layer thickness, which heavily affects SJ performance, as explained in section 4.1.1. This is caused by the aforementioned maintenance which led to dramatically increased deposition rate of the a-SiGe:H material.

The EQE of the three subcells as well as the corresponding 1-R values are shown in figure 4.7. The larger, smoother features of the AZO superstrate scatter light more coherently than the features of the Asahi superstrates, resulting in increased interference of light waves, especially in larger wavelength range [66]. This becomes especially apparent in the interference fringes from the a-SiGe:H EQE and the 1-R graph of the nc-Si:H. The a-SiGe:H EQE's reported in section 4.1 tend to show lower, but broader charge collection peaks. The thinner, narrow peaks of the AZO superstrate are desired for multi-junction cells because this reduces spectral overlap of subcells which is already large for the a-Si:H and a-SiGe:H SJ devices. It should be noted that the EQE of the a-SiGe:H SJ cell is artificially low due to the increased absorber layer thickness of approximately 200 nm. The expected J_{SC} of this is SJ cell on AZO is around 17 mA cm^{-2}, rather than 13.6 mA cm^{-2}.

The high reflection of the a-Si:H and a-SiGe:H cells of respective wavelength ranges in excess of 500 nm and 600 nm is caused by non-absorbed photons that scatter on the back reflector and leave the cell unabsorbed. The lower bandgap gives the nc-Si:H more response for the wavelength range of 700-1100 nm and less defective bulk material ensures better charge collection, which in total gives nc-Si:H a better charge collection for wavelengths over 450 nm. The $J-V$ curves of the three subcells are shown in figure 4.8 which illustrates the trade-off between J_{SC} and V_{OC} for both a-Si:H and nc-Si:H cells.

The slope of the $J-V$ curves near the V_{OC} show that all cells have relatively high series resistance and especially the a-SiGe:H cell shows a low shunt resistance which explains the low FF of this cell. High series resistance in amorphous solar cells are due to the low conductivity of the material. The better conductivity of the nc-Si:H bulk is counteracted by the increase in absorber thickness. Moverover, neither of the cells have undergone thermal annealing, which can improve adhesion of the metal contacts to the TCO and n-layer and, thus, improves the series resistance.

4.4. Tandem devices

This section describes the optimisation of the interface between the subcells of two different tandem devices. The focus lies on improving electrical performance of the TRJ, while some optical variations have been explored as preparation towards the current matching efforts for the 3J device presented in section 4.5.

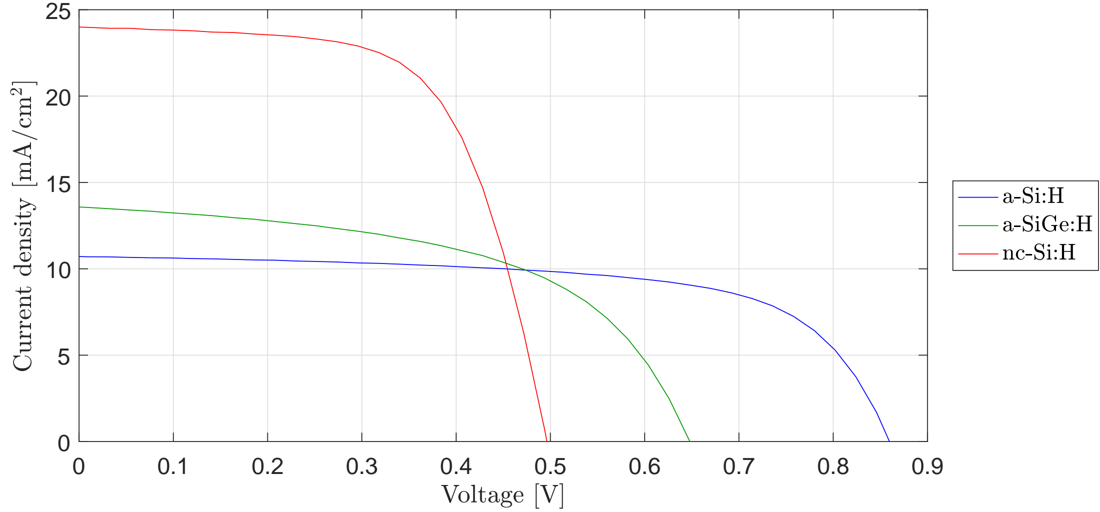

Figure4.8: The $J-V$ curves of the a-Si:H, a-SiGe:H and nc-Si:H SJ devices on an AZO superstrate

4.4.1. a-Si:H/a-SiGe:H top tandem device

The top tandem device consists of an a-Si:H top cell and an a-SiGe:H bottom cell which will function as respective top and middle cells in the final 3J device. The general structure of the SJ subcells is kept the same as presented in section 4.3, with absorber layer thicknesses of 200 nm and 120 nm for the top- and bottom cell, respectively. Figure 4.9 shows the general structure of the tandem device. Various combinations of layers have been processed to function as a TRJ. The nc-SiO$_x$:H n-layer of the top cell and the nc-Si:H p-layer from the bottom cell are considered to be the TRJ and are varied. The thicker nc-SiO$_x$:H p-layer from the bottom cell is kept the same because this layer is less easily manipulated while still maintaining performance. Adjusting dopant concentration and oxygen content of p-layers is typically more difficult than for n-layers because the presence of boron in the plasma affects the layers crystallinity, film growth and other properties [51]. Changing the n-layers is therefore chosen as a starting point to develop high performance TRJs.

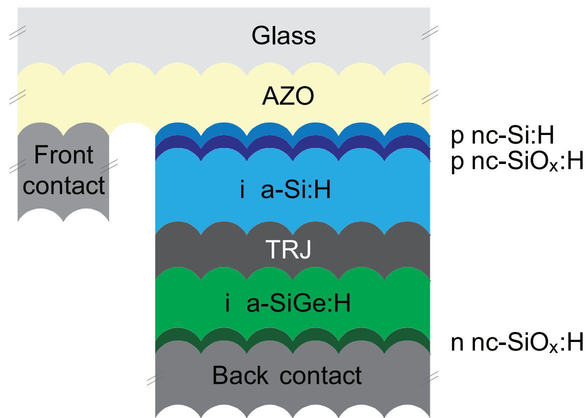

Figure4.9: Schematic structure of the a-Si:H/a-SiGe:H top tandem device. The doped layers in between the intrinsic layers are indicated with TRJ and vary in structure

For the a-Si:H/a-SiGe:H tandem device, five different TRJs were manufactured. The baseline is depositing one cell on top of the other without making an effort to enhance tunnelling (named A+B). The other compositions and their performance are shown in table 4.6. The choice for adding a highly doped nc-SiO$_x$:H n-layer creates better alignment of the conduction and valence bands and provides more trap states where recombination can take place. The function of the p-type nc-Si:H layer is to provide a good ohmic contact with the TCO and to provide a seed to catalyse the growth of the nanocrystal structure in the nc-SiO$_x$:H p-layer. These nanocrystals determine the conductive behaviour of the material and do not immediately grow in with a certain crystalline fraction, but gradually grow in an amorphous matrix with increasing material

crystallinity as the layer grows. It is observed in nc-SiO$_x$ that it needs approximately 20 nm for growing crystallites to meet and to consider the material nanocrystalline [67]. A seed layer is a thin layer that provides a small crystalline fraction on which the nanocrystals can continue to grow. This reduces the required thickness to form a sufficient crystalline material which otherwise thicker than the total p-layer thickness. In this structure, the p-type nc-Si:H layer is not connected to a TCO and the n-type nc-SiO$_x$:H can act as seed for the p-type nc-SiO$_x$:H. Because neither functions are required and for the sake of structure simplicity, this nc-Si:H p-layer was removed in some samples. The last major consideration in the TRJ structure is decreasing the nc-SiO$_x$:H n-layer to reduce parasitic absorption and increase light in-coupling in the bottom subcell.

The target thickness of the intrinsic layer in the a-SiGe:H bottom cell was aimed to be 120 nm, but turned out to be around 200 nm. This is due to the aforementioned maintenance of the processing tool and resulted in a much higher deposition rate. As a consequence the presented electrical performance of the a-SiGe:H subcell is artificially low and its optical response too large for wavelengths >700 nm. The presented values are obtained by averaging the highest performing five dots in terms of V_{OC}, rather than in term of conversion efficiency. This is chosen because efficiency is heavily influenced by current matching, which was not the focus of these experiments. J_{SC} and $J_{SC,sum}$ were included to give an impression about the degree of 'native' current matching and the total generated current density. Moreover, heavily current mismatched cells can exhibit artificially high fill factors due to an upper limit in photo-generated current. Presented J_{SC} values are those of the current limiting subcell of the best performing single cell. The efficiency, as measured during $J-V$ sweep, is scaled with this J_{SC}. The main three variations in structure consist of decreasing the a-Si:H top cell n-layer, adding a higher doped n layer by doubling the phosphine flow rate and removing the a-SiGe:H bottom cell nc-Si:H p-layer.

Table4.6: The thicknesses of various layers used as TRJ in the a-Si:H/a-SiGe:H tandem device and their respective performance. Unique variations are indicated with a bold typeface.

Name	A+B	Thin n	n$^+$	n$^+$, no p	No p
n-type nc-SiO$_x$:H	50 nm	**25 nm**	50 nm	50 nm	50 nm
n$^+$-type nc-SiO$_x$:H	-	-	**5 nm**	**5 nm**	-
p-type nc-Si:H	2 nm	2 nm	2 nm	**-**	**-**
p-type nc-SiO$_x$:H	16 nm	16 nm	16 nm	16 nm	16 nm
V_{OC} (V)	1.46	1.46	1.47	1.46	1.46
J_{SC} (mA cm^{-2})	7.11	7.41	7.68	7.04	6.85
$J_{SC,sum}$ (mA cm^{-2})	15.4	15.6	16.1	15.4	15.3
FF (-)	0.49	0.48	0.48	0.40	0.38
η (%)	5.63	5.75	6.53	4.70	3.87

Considering the values for V_{OC} of the SJ devices as presented in table 4.5, the loss in terms of voltage of all TRJs lie between $\Delta V_{OC} = 58-67$ mV, which is on the better side of the reported efficiencies of mostly similar TRJs [68]. Relatively low values for J_{SC}, in comparison to those of the SJs, are because of the large spectral overlap between the two subcells. Furthermore, the obtained values for FF are sub-optimal. The high deposition rate of the a-SiGe:H subcell has created a more defective layer that is less conductive and has more pathways for leakage currents with respect to an a-Si:H/a-SiGe:H tandem with a lower deposition rate for the a-SiGe:H subcell. This lead to higher R_s and lower R_{sh} by approximately 20% and 40%, respectively, for tandems with nearly identical structure.

While some groups reported good TRJs between n- and p-type SiO$_x$:H, the performed measurements show that the thin nc-Si:H p-layer seems essential to keep the fill factor high [64, 39]. The n$^+$ layer also appears beneficial for the TRJ. Figure 4.10 shows the simulated band diagram of the TRJ between the a-Si:H and a-SiGe:H intrinsic layers. It must be noted that, for visual purposes, the doping levels have been increased and the a minimum layer thickness of 10 nm is maintained. Furthermore, the graded layers in the a-SiGe:H subcell are assumed constant.

It can be seen that high doping concentrations make electrons drift towards the p/n interface. Thin, highly doped layers provide an energy well in which the charge carriers be trapped in a space region closer to the tunnel junction at an energy level closer to the Fermi level. The low activation energy of p-type nc-Si:H, $E_a \approx 50$ meV, provides better band alignment and a better trap for holes generated in the a-SiGe:H intrinsic layer compared to that of p-type nc-SiO$_x$:H, with $E_a \approx 220$ meV. The difference in activation energy

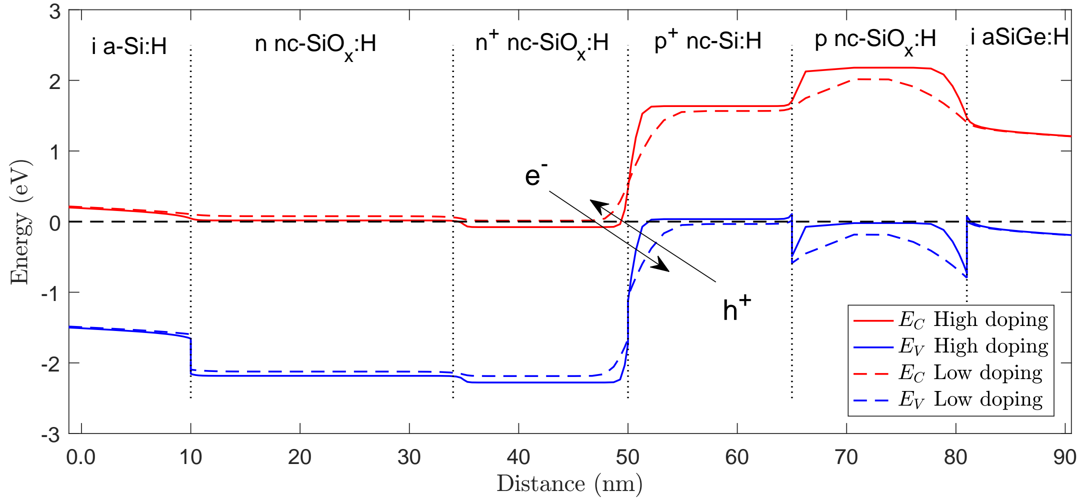

Figure4.10: An simulated energy band diagram of a TRJ in an a-Si:H/a-SiGe:H tandem device with high and lower doping levels. The Fermi level is the reference at 0 eV

and bandgap of the p^+-type nc-Si:H with respect to the p-type nc-SiO_x:H is what causes the sharp band edges at both p-type nc-SiO_x:H interfaces. These sharp edges form potential barriers also require a tunnelling event to cross and inhibit hole flow towards the tunnel junction and decreasing FF. The tradeoff between parasitic absorption and band alignment becomes apparent for p-type nc-Si:H and p-type nc-SiO_x:H.

The influence of doping concentration is also made visible in figure 4.10. Lower doping concentration decreases band bending, and increases the separation of holes and electrons at the junctions in terms of both energy and distance. Enhancing the doping concentration also decreases the barrier width in p-type nc-SiO_x:H and facilitate hole flow. The i a-SiGe:H in figure 4.10 is not graded. The bandgap profiling in this layer increases the material's bandgap which effectively lowers the potential barrier with at the p/i interface.

Figure 4.11 shows the EQE and reflection of three tandem devices named A+B, Thin n and n^+. Reducing the thickness of the nc-SiO_x:H n-layer to 25 nm seems to benefit the light in-coupling in the a-SiGe:H subcell at only a small expense of that of the a-Si:H top cell, resulting in an overall increase of collected charge carriers. An even larger improvement is seen when adding a 5 nm nc-SiO_x:H between the 50 nm n-type nc-SiO_x:H layer and the 2 nm p-type nc-Si:H layer. The better tunnelling conditions provided by the highly doped layer allows more charge collection with roughly the same absorption as the tandem with thinner n-layer. To further investigate, three additional tandems were processed, all incorporating the thin n^+ nc-SiO_x:H layer, with varying n-layer thickness of 15 nm, 25 nm and 35 nm. The external parameters are shown in table 4.7.

Table4.7: The external parameters of a-Si:H/a-SiGe:H tandem devices with varying top cell n-type SiO_x:H layer and constant 5 nm n^+-type SiO_x:H layer as TRJ. This cell was processed in a different batch with a 200 nm, instead of 120 nm, intrinsic a-SiGe:H layer.

Top cell n-layer thickness	V_{OC} (V)	J_{SC} (mA cm^{-2})	$J_{SC,sum}$ (mA cm^{-2})	FF (-)	η (%)
50 nm*	1.466	7.68	16.08	0.48	5.4
35 nm	1.465	6.55	15.01	0.49	4.7
25 nm	1.474	7.32	15.57	0.55	5.9
15 nm	1.456	6.94	15.23	0.52	5.3

A n-type SiO_x:H layer thickness of 25 nm yield the best results for V_{OC} and FF. The 15 nm layer is likely too thin for adequate crystal growth, inhibiting conductivity, FF and charge collection. The 35 nm layer shows low charge collection and low FF. Over all dots, only two seemed to be on par with the rest of batch, while the rest under performed with an average $FF = 0.36$. It seems likely that the low performance is due to an external effect because of the magnitude and inconsistency of the performance drop with respect to the small change in structure. Contamination and/or improperly prepared AZO may give rise to shunts and/or

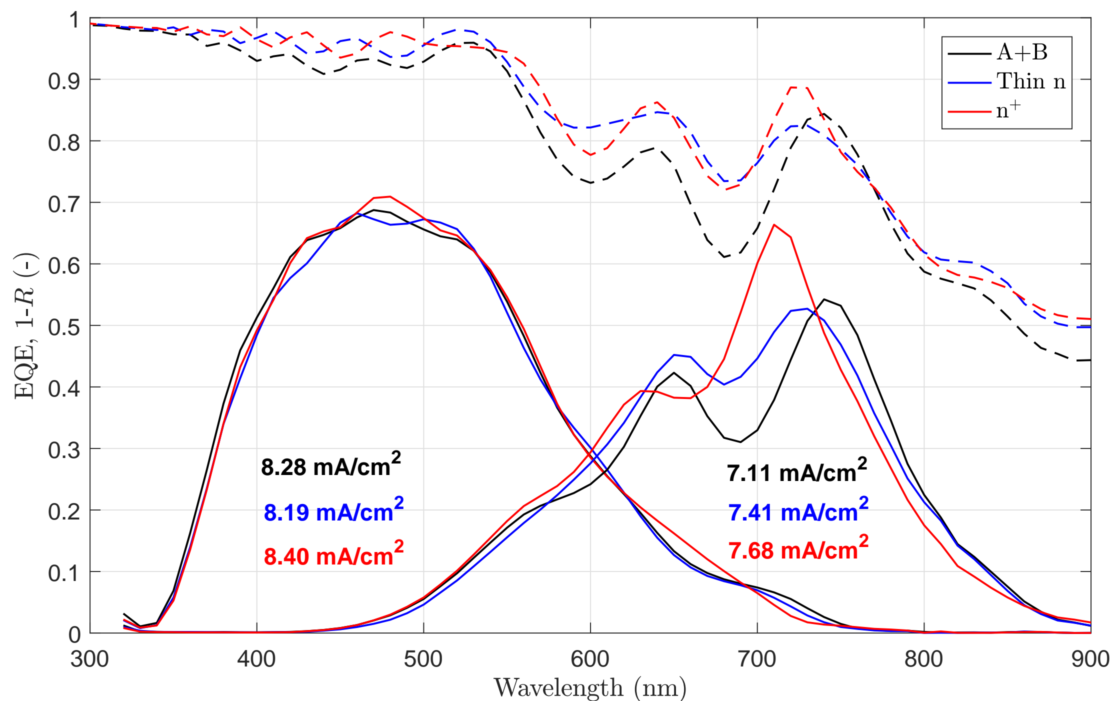

Figure4.11: The EQE and 1-R graphs of a-Si:H/a-SiGe:H tandem solar cells with 50 nm nc-SiO$_x$:H n-layer (A+B), 25 nm nc-SiO$_x$:H n-layer (Thin n) and 50 nm nc-SiO$_x$:H n-layer plus and added 5 nm nc-SiO$_x$:H n$^+$-layer (n$^+$)

low conductivity of the TCO, respectively.

Figure 4.12 compares the EQE and reflectance of the tandem with 15 nm, 25 nm and 35 nm thick n-layer. The current generated in the top cell for all tandems is very similar, but slightly less for the cell with 25 nm n-layer, while it shows significant improvement in the current generation of the bottom cell. Decreasing the thickness of the top cell n-layer reduces parasitic absorption as well as reduces the light reflected back into the top cell. Non-absorbed photons, typically with an energy close to the bandgap of a-Si:H, initially reflected off the thicker n-layer now reach the a-SiGe:H, where they can be absorbed and collected. Decreasing the n-layer thickness too much leads to further decrease in the top cell and more reflection because of interference, which keeps the current production low in the bottom cell. The shift in spectral response of a tandem with 200 nm a-SiGe:H and 120 nm intrinsic layer becomes clear when comparing EQE from figure 4.12 with that shown in figure 4.11.

Although the 35 nm thick n-layer could not be ruled out to outperform the 25 nm n-layer electrically, but based on the small number of working dots and the data from the 50 nm nc-SiO$_x$:H n-layer, the 25 nm nc-SiO$_x$:H is most likely to exhibit the best performance.

The 50 nm reference from the previous batch shows only improved performance in terms of J_{SC} with respect to the 25 nm n-layer thickness. The thickness of the intrinsic a-SiGe:H layer was tuned in a new batch to optimise the tradeoff between absorption and electrical properties, resulting in an intrinsic layer thickness of 120 nm. This decrease in thickness causes a larger mismatch in generated current, with respect to the 200 nm absorber, increasing V_{OC} and FF at the expense of J_{SC} and η low.

Based on the findings presented above, it is expected for the 3J device to have the highest performance when the TRJ of the top and middle subcells consists of 25 nm n nc-SiO$_x$:H, 5 nm n$^+$ nc-SiO$_x$:H with 2 nm p nc-Si:H and 16 nm p nc-SiO$_x$:H.

4.4.2. a-SiGe:H/nc-Si:H bottom tandem device

The Bottom tandem device is comprised of an a-SiGe:H top cell and a nc-Si:H bottom cell. These cells will function as middle and bottom cell, respectively, in the final 3J device and their interface will form the second TRJ in the 3J structure. The general structure of this bottom tandem, along with what is considered as TRJ is shown in figure 4.13. The difference with the SJ structures as presented in section 4.3, is that the i a-SiGe:H absorber layer thickness is increased to 200 nm. This value is chosen because these experiments were per-

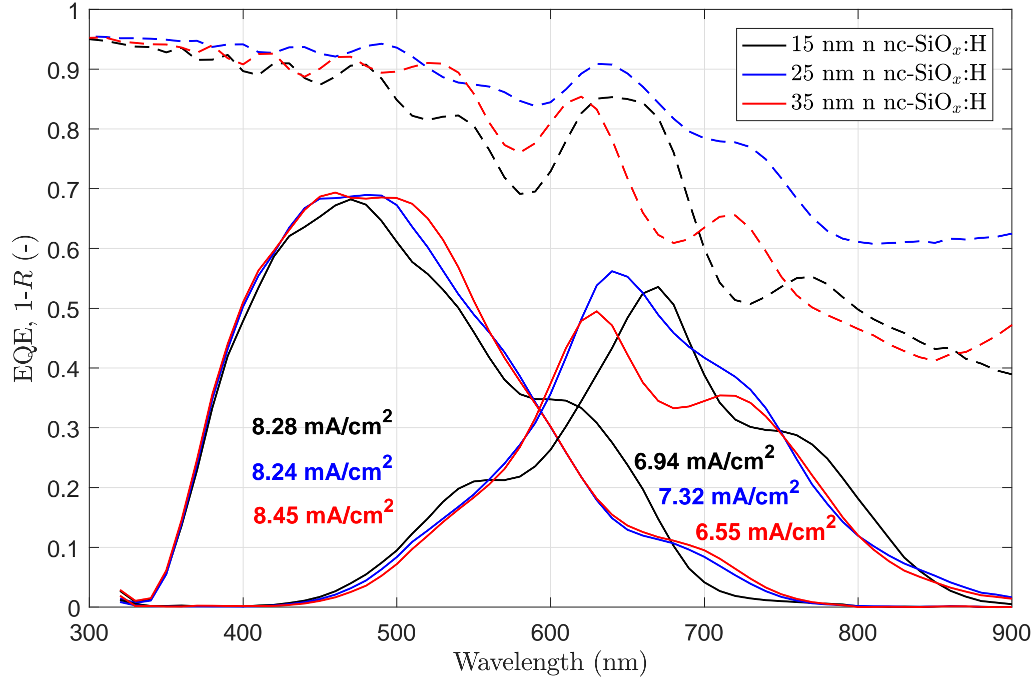

Figure4.12: The EQE's and 1-R of the a-Si:H/a-SiGe:H tandem solar with 15 nm, 25 nm and 35 nm as thickness of the nc-SiO$_x$:H n-layer

formed prior to a-SiGe:H thickness series experiments. The graded nc-SiO$_x$:H n-layer is kept at a constant thickness of approximately 12.5 nm. The n-type nc-SiO$_x$:H layer and p-type nc-Si:H were varied in thickness or removed, while some samples included an additional n nc-Si:H, n$^+$ nc-SiO$_x$:H or n a-Si:H. As explained in the section (4.4.1), most adaptations were made in the n-layer as this layer provides a better starting point for experimentation.

Initially, four a-SiGe:H/nc-Si:H tandem devices were processed, to which, two were later added and have a 120 nm a-SiGe:H intrinsic layer. The two tandem devices from a different batch are separated by a vertical line and were processed after re-calibration of the SiGe:H material. Again a baseline TRJ was fabricated by sequentially depositing the SJ devices without putting additional effort in the TRJ (named A+B). One consideration was by increasing the doping concentration of the n-type nc-SiO$_x$:H layer and decreasing its thickness slightly to increase drift of electrons to the interface and provide trap states that facilitate recombination (n$^+$). Another proposed structure uses a n nc-SiO$_x$:H/p nc-SiO$_x$:H TRJ (SiO$_x$), which is reported to provide a good tunnel in literature junction as well as simplify the device structure. The last TRJ of the initial set has a n nc-Si:H/p nc-Si:H TRJ that, with low activation energies can provide good band alignment (nc-Si). From the second set the p-type nc-Si:H was removed and the thickness of the nc-SiO$_x$:H n-layer was increased to enhance charge collection and crystalline fraction at the n/p interface (SiO$_x$ -2). The last TRJ structure (n$^+$-2) adds a 5 nm nc-SiO$_x$:H n$^+$-layer to the structure to further enhance band alignment, the electric field and recombination due to the induced trap states. The exact structure of the TRJs along with their respective performances are shown in table 4.8. The presented values are selected on the best five performing dots, again, in terms of V_{OC}.

The performance of all tandems in terms of V_{OC} is very similar and have a maximum deviation of only 12 mV within the same batch. The jump in V_{OC} of the second set with respect to the first can attributed to the a-SiGe:H SJ performance, which has dropped by approximately 20 mV for cells with the same structure as used in their respective tandem devices and that were processed around the same time. The loss in V_{OC} by the TRJ with respect to the SJs is in the range of 18-30 mV for the first batch and 46-56 mV for the second batch. As a reference, a TRJ with the same structure as SiO$_x$:H in table 4.8 was reported to suffer a 45 mV loss in V_{OC} [68]. Despite the artificially low value for TRJ voltage loss, because of the underperforming a-SiGe:H SJ on AZO, it still gives sufficient TRJ performance and a good starting point.

In contrast to the TRJ experiments for the top tandem, the p-type nc-Si:H layer appeared detrimental to the FF in the TRJ experiments for the bottom tandem. The p-type nc-Si:H acts as a seed layer for the p-type

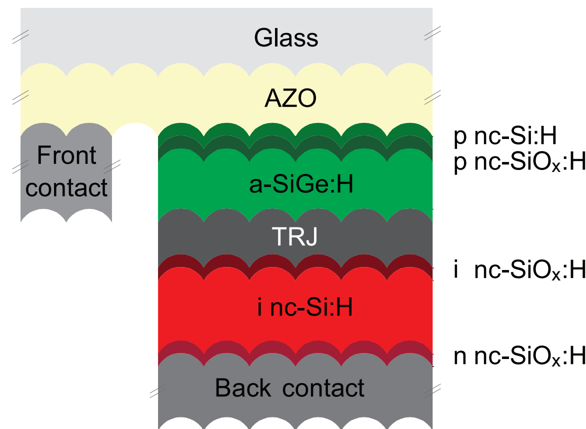

Figure4.13: Schematic structure of the a-SiGe:H/nc-Si:H bottom tandem device. The doped layers in between the intrinsic layers are indicated with TRJ and vary in structure

Table4.8: The thicknesses of various layers used as TRJ in the a-SiGe:H/nc-Si:H tandem device and their performance. Two right-most solar cells were processed in a separate batch. Notable deviations in structure are indicated with a bold typeface as a guide to the eye

Name	A+B	n^+	SiO_x	nc-Si	SiO_x-2	n^+-2
n nc-SiO_x:H (graded)	12.5 nm	12.5 nm	12.5 nm	12.5 nm	25 nm	25 nm
n nc-SiO_x:H	12.5 nm	12.5 nm	**22.5 nm**	12.5 nm	25 nm	25 nm
n^+ nc-SiO_x:H	-	**10 nm**	-	-	-	**5 nm**
n nc-Si:H	-	-	-	**10 nm**	-	-
p nc-Si:H	2 nm	-	-	2 nm	-	-
p nc-SiO_x:H	16 nm	16 nm	16 nm	16 nm	16 nm	16 nm
V_{OC} (V)	1.14	1.13	1.14	1.13	1.11	1.10
J_{SC} (mA cm^{-2})	11.0	10.1	10.2	11.0	7.3	9.96
$J_{SC,sum}$ (mA cm^{-2})	22.9	21.2	22.2	22.8	18.3	22.6
FF (-)	0.61	0.65	0.65	0.63	0.70	0.69
η (%)	7.63	7.35	7.62	7.78	5.62	7.56

nc-SiO_x:H for SJ operation. In the top tandem 50 nm of n-type nc-SiO_x:H can be used as seed layer whereas it has only 25 nm n-type nc-SiO_x:H to use as a seed in the bottom tandem. If more crystallinity is desired, it is expected to be needed more in the bottom tandem device. Although alternate effects that cause the p-type nc-Si:H layer to negatively affect the material's crystallinity can not be ruled out, it is expected that the thicker n-layers in both samples without a nc-Si:H p-layer enhance carrier collection from the a-SiGe:H subcell.

The higher FF of the second set with respect to the first is likely due to the reduction of thickness defective a-SiGe:H material that led to a reduction of R_s and an increase of R_{sh}. A secondary effect is that the two latter cells have a lower J_{SC} because of the larger current mismatch which also keeps the value for FF high. The EQE and reflectance of the nc-Si and n^+ -2 tandem devices are shown in figure 4.14.

The red graphs show the EQE of the tandem device with nc-Si:H n- and p-type as TRJ and shows that the two subcells have a very close match in current generation. While unintentional, the mismatch in generated current is only 0.9 mA cm^2. This means that an a-Si:H top cell stacked on this tandem device will absorb most of the light of the a-SiGe:H subcell, while the nc-Si:H bottom cell barely has any additional competition in light absorption with respect to the a-SiGe:H subcell. This predicts a large drop in generated current in the a-SiGe:H subcell, but a minimal drop in generated current of the nc-Si:H subcell. The n^+ tandem from the second set shows larger collection of charge carriers in the top cell, which is possibly due to a the better charge collection of the thicker n-layer and could further be enhanced by the stronger electric field over the intrinsic layer by the highly doped n-layer. The increase in reflection at a wavelength of approximately 700 nm is also attributed to the thicker n-layer [69]. The slight increase in charge collection of the nc-Si:H subcell in

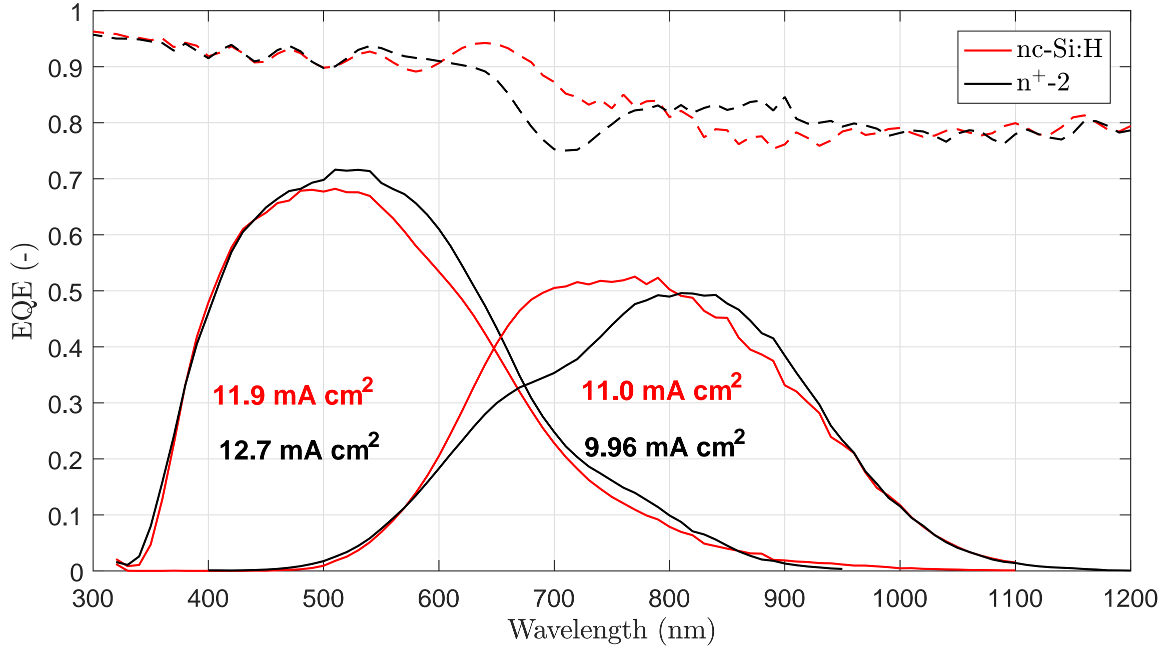

Figure4.14: The EQE and 1-R of the a-SiGe:H/nc-Si:H tandem device with n-type nc-Si:H and n^+-type nc-SiO_x:H as TRJ from the second batch

the infrared range is due to the 200 nm increase in intrinsic layer thickness.

Based on the findings presented above, it is expected for the 3J device to have the highest performance when the TRJ of the top and middle subcells consists of 50 nm n SiO_x:H, of which the first half has graded oxygen content, 5 nm n^+ nc-SiO_x:H and 16 nm p nc-SiO_x:H. Among the experiments performed, this structure provides the best starting point for current matching in the final 3J device without compromising in terms of V_{OC} and FF.

4.5. Triple junction device

The focus during the manufacturing of the 3J devices is on light management. By changing the absorber layer thickness of different subcells, it's current generation can be tuned and that of the cells below it. Another used technique is using an intermediate reflective layer to redistribute light from a lower, into the current limiting subcell. A schematic of the baseline device structure is shown in figure 4.15.

The 3J structure is deposited on the AZO superstrate with respective absorber layer thicknesses of 200 nm, 120 nm and 3000 nm for the a-Si:H, a-SiGe:H and nc-Si:H subcells, respectively. The top a-Si:H cell has a 25 nm n-type nc-SiO_x:H and the TRJ with the middle cell consists of 5 nm n^+-type nc-SiO_x:H and 2 nm p-type nc-Si:H. The TRJ between the middle and bottom subcells consists of 50 nm n-type nc-SiO_x:H, of which the first half has graded oxygen content, and 16 nm p-type SiO_x:H. Despite providing good experimental results from the bottom tandem series, the thin, n^+ nc-SiO_x:H layer in between the regular a-SiGe:H and nc-Si:H structures showed a decrease in fill factor with. The difference in the tandem experiment is that the a-SiGe:H subcell is now the current limiting cell, and is effectively forward biased by the non-recombinated charge carriers at the TRJ. Although not completely understood. It is suspected that the interplay in enhanced electric field by the nc-SiO_x:H n^+-layer and defects that enhance leakage current is tipped to the latter, reducing it's shunt resistance.

A series of 3J devices was manufactured with varying intrinsic layer thicknesses of all subcells. The results in performance are shown in figure 4.16. Different markers and color signify a variation of thickness of certain subcells. All error bars are positioned at $\pm 1\ \sigma$ from the average over the best 5 dots per stripe. The J_{SC} was determined by the EQE measurement of the best cell which is used to scale the errors and η accordingly.

Nearly all 3J devices are able to generate a V_{OC} of 1.90 V with a maximum V_{OC} = 1.96 V. Based on the SJ performance on AZO, this signifies a drop of ΔV_{OC} = 63 mV, which is only a minor drop, even when accounting for the artificially low value for V_{OC} of the a-SiGe:H subcell on AZO, as losses of appriximately ΔV = 50 mV per junction are not uncommon [68]. The V_{OC} is shown to drop as a function of absorber thickness. More

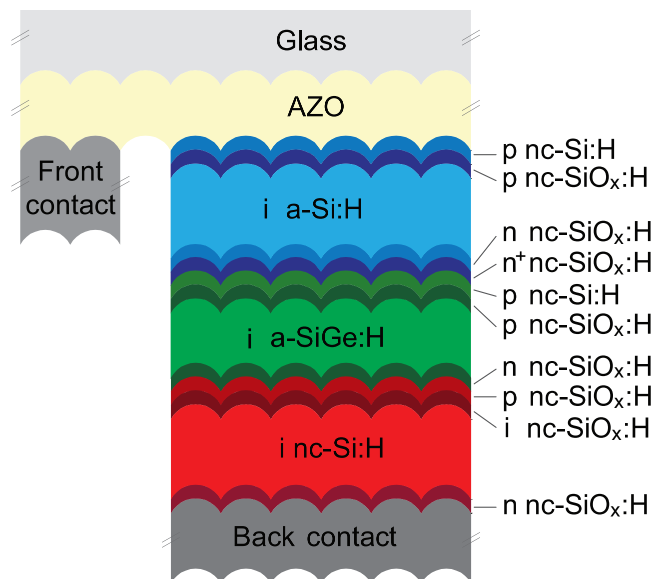

Figure4.15: Schematic structure of the most common used configuration of the a-Si:H/a-SiGe:H/nc-Si:H triple junction device

defective material leads to increased J_0 and increase of series resistance, which is reflected in the decline of FF. The lower generated current in the 3J device compared to the SJ or tandem devices acts as a cap for the generated current which decreases the slope of the $J-V$ curve and effectively leads to a higher shunt resistance and therefore higher FF. Most cells show a $J_{SC} \approx 5.5$ mA cm^{-2}. Typically the middle cell is the current limiting because the top cell receives the full spectrum and filters out a part for the bottom two cells, while bottom cell benefits the most of the back reflector, which leaves the middle cell with the smallest fraction of light to generate current with. Variations in cell structure that increase current generation in the middle cell will therefore directly affect J_{SC} and η. Reducing the intrinsic layer thickness of the top a-Si:H cell to 175 nm shows the most gain in J_{SC}. Decreasing the layer too much resulted in very few working dots that resulted in the large statistical error. It was observed in multiple samples that intrinsic layer thickness ≤150 nm in either V_{OC}, J_{SC} or FF. The nature of this performance drop is to be further investigated as the devices with thicker a-Si:H absorber layers did not exhibit low performance as consistently. Moreover, other research within this group has successfully produced a-Si:H solar cells with intrinsic layer thickness as thin as 85 nm [68].

The large error margins for the 200 nm a-Si:H cell is caused by a misalignment of the shadow mask while processing the back contacts. This effectively increased the active area of some cells, which is used to calculate the J_{SC} in the $J-V$ sweep measurements, which is usesd to determine the statistical error. Increasing the middle cell thickness only gives a slight increase in current generation. This is due to the tradeoff in shift in the EQE as well as introducing more defects add recombination centres, as explained in section 4.1.1. The 120 nm a-SiGe:H cell was expected to continue this trend, but this cell was processed in a different batch that exhibited better overall performance. The much higher FF shows that this material likely suffers less from recombination which allows its J_{SC} to exceed that of the thicker a-SiGe:H intrinsic layers. As the nc-Si:H subcell was not observed to be current limiting, the added thickness is not beneficiary for 3J performance and only increases the series resistance. The cells denoted with 120 nm a-SiGe:H and 3000 nm nc-Si:H, are the same cell. As previously mentioned, this sample showed good performance and causes it to outperform the 2800 nm nc-Si:H cell despite the 200 nm thicker intrinsic layer.

The EQE of 3J with intrinsic layer thicknesses of 200 nm/120 nm/3000 nm for respective a-Si:H/a-SiGe:H/nc-Si:H subcells is shown in figure 4.17. The a-Si:H top cell only loses 2.5 mA cm^{-2} compared to its single-junction performance due to the lack of back reflector. With a drop of 7.7 mA cm^{-2}, the a-SiGe:H subcell loses over half of its original J_{SC} because of the high spectral overlap between that of the a-SiGe:H and a-Si:H subcells. In the tandem cells the a-SiGe:H subcell achieved 7.68 mA cm^{-2}, showing that ≈2 mA cm^{-2} is lost due to a lack in back reflection. Despite a drop of 15.6 mA cm^{-2} in J_{SC}, with respect to its SJ performance, the nc-Si:H subcell still generates the most current. The top and bottom cells show a good match, but the middle cell is throttling the total output current of the device. The sum of the EQE of all three subcells shows a large

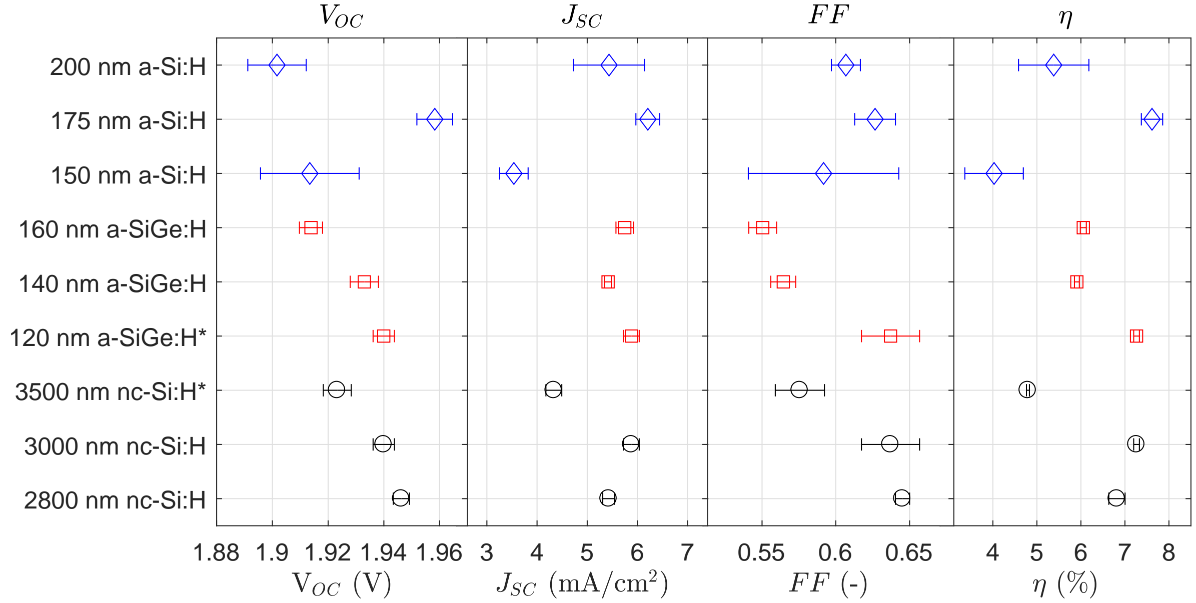

Figure4.16: Triple junction performance as function of absorber layer thickness. The default thickness of the a-Si:H, a-SiGe:H and nc-Si:H subcells are 200 nm, 120 nm, 3000 nm, respectively. The asterisk (*) denotes that a cell was processed in a different batch with respect to those in the same series.

dip between $\lambda = 550 - 600$ nm, which coincides with a dip in the 1-R graph. It shows that optical effects, like light interference and limited transmittance of the TCO, hamper the current collection in the middle cell. High performance TCO's like ITO and IOH could reduce the reflection of light in this wavelength range, but as both TCO's incorporate indium, using these TCO's would defeat the purpose of a 3J device based on earth abundant materials.

To achieve a higher current density in the middle cell, the thickness of the nc-SiO$_x$:H n-layer of the a-SiGe:H was varied. Other experiments were adding a p-type nc-Si:H layer between the middle and bottom subcells to increase the contrast in refractive index, and thus reflection. Lastly, a 3J was deposited on an Asahi VU superstrate, which has a texture with smaller feature sizes that scatters light more effectively for thin absorber layers.

Table4.9: The external parameters and current generated in each separate subcell for 3J devices with various reflective layers

Reflection layer	V_{OC} (V)	$J_{SC,top}$ (mA cm^{-2})	$J_{SC,mid}$ (mA cm^{-2})	$J_{SC,bot}$ (mA cm^{-2})	FF (-)	η (%)
Reference	1.94	8.18	5.88	8.46	0.64	7.26
100 nm n nc-SiO$_x$:H	1.87	8.23	4.83	8.93	0.55	4.97
125 nm n nc-SiO$_x$:H	1.91	7.79	4.43	9.61	0.51	4.34
5 nm p nc-Si:H (AZO)	1.87	8.23	5.46	8.47	0.57	5.63
5 nm p nc-Si:H (Asahi)	1.92	9.25	6.59	7.23	0.60	7.11

Table 4.9 shows the external parameters as well as the total generated current in various 3J devices with different reflective layers. The cell, of which the EQE is shown above, is taken as reference. This cell has, three layers in between the intrinsic layers of the middle and bottom cell. A 50 nm, half-graded, n nc-SiO$_x$:H layer, a 16 nm p SiO$_x$:H layer and 5 nm i nc-SiO$_x$:H. The n-type SiO$_x$:H layer is increased by 50 nm and 75 nm and results in a total respective n-layer thickness of 100 nm and 125 nm for the second and third entry of table 4.9. The fourth and fifth entries both have the same structure as the reference but with an added 5 nm p nc-Si:H in between both nc-SiO$_x$:H layers. This layer provided good results in the tandem series and can provide a large refractive index contrast to enhance reflection. The difference between the last two samples in the table is that the cells are either deposited on the Corning glass with AZO or on Asahi VU superstrates.

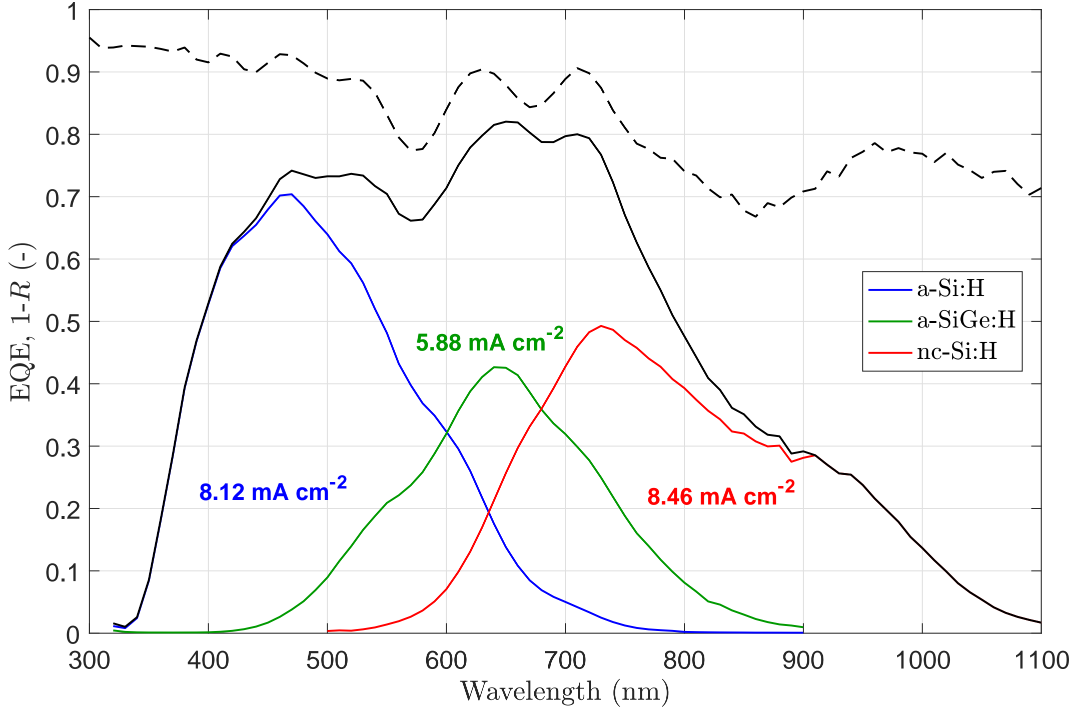

Figure4.17: EQE of an a-Si:H/a-SiGe:H/nc-Si:H 3J device with intrinsic layer thicknesses of 200 nm/120 nm/3000 nm, respectively.

Increasing n-type nc-SiO$_x$:H layer seems to have an adverse effect on current generation in the middle cell. In fact, the current generated in the bottom cell increases as well as the total generated current of the cell. Even more so than increasing the nc-Si:H intrinsic layer by 500 nm. For increasing n-layer thickness of 50 nm/100 nm/125 nm, the Bragg wavelength, λ_B, is calculated to be approximately 450 nm/910 nm/1130 nm, by using equation 2.8 and the refractive index of n-type nc-SiO$_x$:H, $n = 2.27$. This shows that with changing n-layer thickness, the wavelength at which pronounced reflection occurs shifts to longer wavelengths, which are increasingly less absorbed by the middle cell. The values mentioned above are calculated using the refractive index of n-type nc-SiO$_x$:H at a single wavelength $\lambda = 900$ nm. This approximation seems reasonable despite the wavelength dependency of n because its values stay within the relative small range of $n = 2.0-2.6$ for a wavelength range of $\lambda = 300-1200$ nm. Although this can explain the trade in current generation of the middle and bottom cell, it predicts a decrease of total current generation because the reflected light of higher wavelengths does not reach the bottom cell and is not absorbed by the top and middle cells. The graphs of figure 4.18 show the reflectance graphs of the 3J devices with 50 nm, 100 nm and 125 nm thickness of n-type nc-SiO$_x$:H. Aside from the n-layer in between the middle and bottom subcells, all devices have identical structures with absorber layer thicknesses of 200 nm, 120 nm and 3000 nm for the a-Si:H, a-SiGe:H and nc-Si:H subcells, respectively. The graph shows higher reflectance for the 100 nm and 125 nm n-layer around those wavelengths. For the 50 nm thick n-layer, no additional reflection is observed, because light of this wavelength is already absorbed by the top and middle subcells. The deviation in measured and calculated λ_B can be attributed to the n-type nc-SiO$_x$:H layer, that has a graded refractive index and does not provide an interface, as well as the disregarded wavelength dependency and any uncertainties in the measured values for n.

The total reflection is shown to stay approximately constant for all samples. The sample with 125 nm n-layer has less reflection in the 800-950 nm range, while larger reflection in the 1000-1200 nm range. The higher absorption of the nc-Si:H in this regime additional to the in larger spectral photon flux cause for a larger generated current in this subcell.

The reflection of light of perpendicular incidence between p-type and n-type nc-SiO$_x$:H is calculated using the respective values for $n = 2.67$ and $n = 2.27$ for $\lambda = 900$ nm and the Fresnel equation (2.7). The small relative difference in refractive index, but high absolute value result in a reflection of 0.66% for perpendicular incidence. Adding the p-type nc-Si:H layer with $n = 3.67$ at $\lambda = 900$ nm, gives a reflection of 5.6% and 2.5% at the n/p and p/p interfaces, respectively. Despite the theoretical reflection, the current generated by

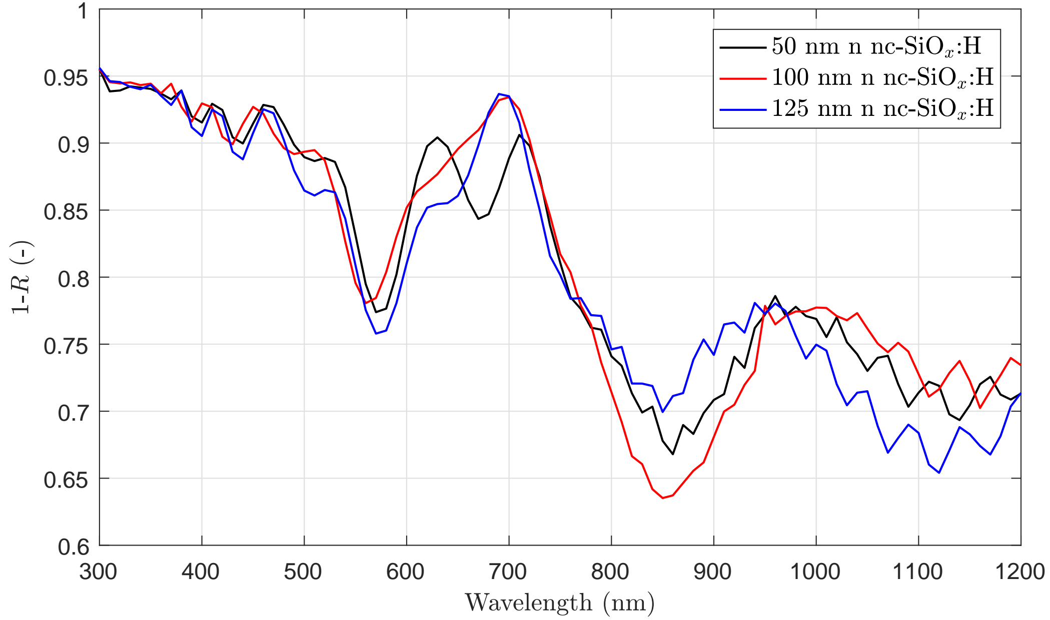

Figure4.18: The measured 1-R graphs of 3J devices with 50 nm, 100 nm and 125 nm n-type nc-SiO$_x$:H layer thickness

the sample with p-type nc-Si:H layer on AZO did not increase with respect to the reference. In fact, all external parameters show lower values. This may be due to a inhomogeneous deposition temperature. The samples on the thin Corning plus AZO and thicker Asahi superstrates were processed simultaneously in the same holder. The difference in thickness between both superstrates can result in a small surface contact area, and thus, heat conduction between the thin sample and the sample holder. Moreover, the V_{OC} and FF of the 3J on Asahi are higher than those of the device on AZO superstrate. The small feature size of the texture on the Asahi VU glass leads to collisions in the growth of nc-Si:H that leaves vertical filaments in the structure that reduce the V_{OC} and FF of the nc-Si:H cell with respect to that on an AZO superstrate [51]. The 3J on the Asahi superstrate indeed shows enhanced current generation in the top and middle cells at the expense of the bottom cell as can be seen in figure 4.19.

Despite the lower total current generation, the generated current by the subcells in this sample is better distributed, which gives this cell the third highest conversion efficiency of all 3J devices produced in this work. The light is scattered very incoherently, which gives the light long path lengths through the top two subcells and limits the interference in the absorption range of the middle cell, which allows it to absorb more light.

From the presented results, the best reported cell has intrinsic layer thicknesses of 175 nm/120 nm/3000 nm for the a-Si:H/a-SiGe:H/nc-Si:H subcells, respectively. No additional reflective layers were found to outperform the 50 nm n-type SiO$_x$:H layer, native to the a-SiGe:H subcell. The Asahi VU superstrate was found to have good light scattering performance in the absorption range of the middle cell, which resulted in the best current matched cell despite lower performance in terms of FF, V_{OC} and total generated current.

4.5.1. Solar-to-fuels efficiency

The $J-V$ curves of the three best 3J devices are plotted, in figure 4.20, against the $J-V$ characteristics of an IrO$_x$ counter electrode for the oxygen evolution reaction. IrO$_x$ is an electrode commonly used for water splitting. The $J-V$ curve of the counter electrode is determined versus RHE. The dashed line includes a total overpotential of 0.1 V. Half of which accounts for ohmic losses in the electric circuit and the other half accounts for the required overpotential of a high performance electrode to catalyse the hydrogen evolution reaction, like platinum or nickel-molybdenum, which is assumed independent of current density [70, 71]. The intersection of the curves gives the operational point for a water splitting reaction, which can be used to calculate the corresponding η_{STF}. To include CO_2 reduction and provide a more general η_{STF} is less straightforward as E^0 and J_{ph} heavily depend on the used electrode and the reaction products. The solar cell $J-V$ curves are obtained by averaging the sweeps of the best five dots per stripe and scaling the current density down with an EQE measurement of the best dot.

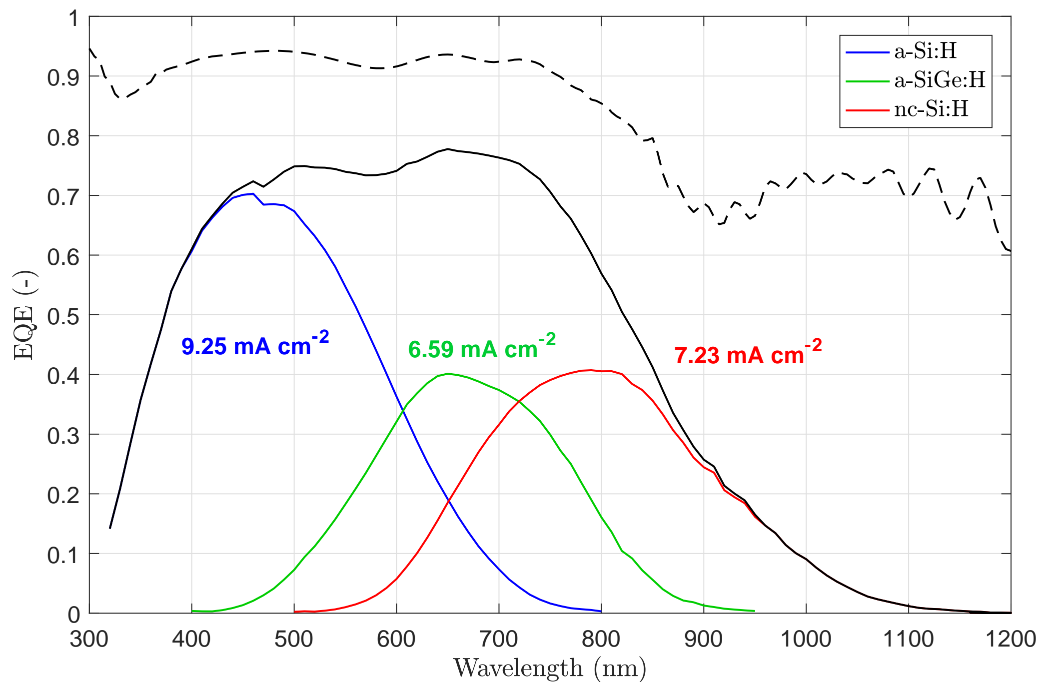

Figure4.19: EQE of an a-Si:H/a-SiGe:H/nc-Si:H 3J device on an Asahi VU superstrate with a p-type nc-Si:H intermediate reflective layer between the middle and bottom subcells

The MPPs of all three devices lie very close together and are located at a lower voltage than the operational voltage. The operational current density, J_{ph}, is used to calculate η_{STF}. Table 4.10 provides an overview of the external parameters of the three solar cells, J_{ph}, and the calculated η_{STF} for hydrogen production using equation 2.17 and $E^0_{H_2} = 1.23$ V.

Table4.10: The external parameters, operational current density and solar-to-fuel efficiency of the best performing 3J devices including 0.1 V overpotential. The thickness of the a-Si:H subcell is indicated in brackets. The respective thickness of the a-SiGe:H and nc-Si:H intrinsic layers are 120 nm and 3μm for all samples

Cell	V_{OC} (V)	J_{SC} (mA cm^{-2})	FF (-)	η (%)	J_{mpp} (mA cm^{-2})	J_{ph} (mA cm^{-2})	η_{STF} (%)
Reference (200)	1.94	5.88	0.64	7.26	4.69	3.93	4.83
a-Si:H (175)	1.96	6.21	0.63	7.63	4.99	3.97	4.88
Asahi (200)	1.92	6.22	0.60	7.15	4.80	3.68	4.53

Because the operating point is so close to the MPP, the solar cell with the highest conversion efficiency also has the most efficient production of hydrogen, reaching $\eta_{STF} = 4.88\%$, assuming the same ratio in surface area of the solar cell and electrode. The $J-V$ curve of the device with a 175 nm thick a-Si:H intrinsic layer almost completely encompasses that of the other two solar cells. Its J_{SC} is only slightly lower than that of the solar cell on the Asahi superstrate. The estimated η_{STF} for hydrogen production can increase to 5.87% if the device were to be perfectly current matched, while maintaining its other external parameters. This corresponds to a J_{ph} of 4.77 mA cm^{-2}. A $\eta_{STF} = 6.2\%$ was achieved in previous work using an a-Si:H/nc-Si:H/HIT stack, which has a slightly lower V_{OC} of 1.93 V, but outperforms the 3J of this work in terms of current density, with $J_{ph} = 8.5$ mA cm^{-2} [47].

The CO_2 reduction reaction with the lowest electrochemical potential is that of methane, with $E^0 = -0.24$ V. Assuming this can be reduced with an electrode with similar $J-V$ characteristics, the η_{STF} can reach 2.4% when producing both hydrogen and methane, assuming the methane evolution electrode requires the same potential as the high-performance hydrogen evolution electrode. At this point the operational voltage is 1.9 V,

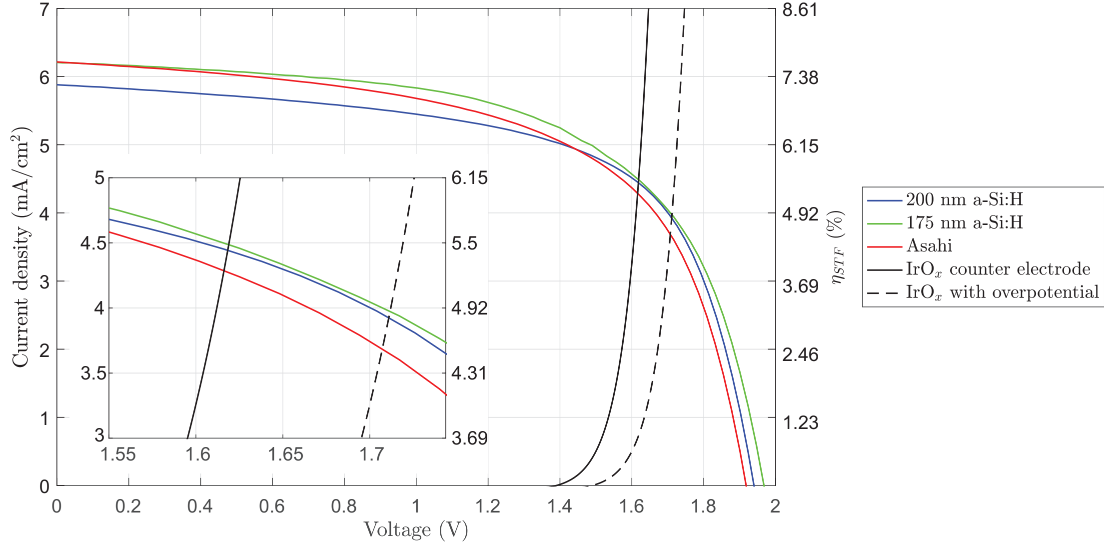

Figure4.20: The $J-V$ characteristics of the best three 3J devices and that of an IrO_x counter electrode for the hydrogen evolution reaction with- and without 0.1 V overpotential. The inlay gives a zoomed view of the operational points of the 3J devices

which is very close to the cell V_{OC}.

To give an estimation of the degraded 3J performance, the single-junction degradation is used. The degraded V_{OC} is the sum of V_{OC}'s of the degraded subcells, while the TRJ voltage loss is kept constant. The reported degradation in V_{OC} of a-Si:H cells is limited to 3%, which corresponds to a $\Delta V_{OC,Si}$ = 26 mV [35]. The light soaking results are taken for the a-SiGe:H subcell, which corresponds to $\Delta V_{OC,SiGe}$ = 60 mV. The degradation of the nc-Si:H subcell is neglected, which gives the total degraded ΔV_{OC} = 86 mV or -4.4% with respect to 1.96 V initial V_{OC}. Because the a-SiGe:H subcell is the current limiting cell, it's J_{SC} determines that of the 3J device. A degradation of -8.6% of a J_{SC} results in ΔJ_{SC} = 0.53 mA cm$^-$2. The new operational point for the IrO_x counter electode is at J_{ph} = 3.14 mA cm$^-$2 and results in a η_{STF} =3.86% for hydrogen production. When methane is produced with an electrode overpotential similar to that of Pt for the hydrogen evolution reaction, the operational point drops to J_{ph}=0.67 mA cm$^-$2 and corresponds to an η_{STF}=0.97%. This estimation neglects degradation in FF. A degraded 3J device based on the structure presented in this work will most likely be ably to sustain a water splitting reaction. CO_2 reduction reactions producing methane will likely have negligible efficiency and will not be able to produce hydrocarbons with electrochemical potentials in excess of 0.3 V.

A very high V_{OC} is essential to obtain higher margins for deterioration of the solar cell and a more gradual course of η_{STF} when the generated voltage by the device degrades, because it operates in a more horizontal regime of the $J-V$ curve. Lastly, a higher operational voltage will give the possibility to generate more different carbon-based species as well as providing more flexible electrode compatibility. This last part is important for long-term operation, because some electrodes are unstable in the environment that provides lower overpotentials. Higher operational voltage of the solar cell allows the reaction to take place in a chemically stable environment at the expense of electrical performance. This is a large advantage of the incorporation of a CO_2 reduction reaction, because part of the overpotential may be used to produce species with higher electrochemical potential, which increases η_{STF}. For water splitting alone, larger overpotentials only provide more margins for degradation of the system.

An identical structured, but with an additional a-Si:H subcell quadruple junction (4J) thin-film solar cell was developed in this group which achieved a V_{OC} = 2.776 V, J_{SC} = 3.52 mA cm^{-2} and FF=0.74 [68]. An alternative structure for a high performance 4J was obtained with a-SiO_x:H/a-Si:H/nc-Si:H/nc-Si:H subcells and achieved V_{OC}=2.82 V and a J_{SC} =5.49 mA cm^{-2} and FF = 0.74 [68]. The voltage of these cells is much larger than what is required for water splitting alone. Increasing the possible produced species, results in potentially higher η_{STF} because of higher electrochemical potential. The large overpotential also creates margin for degradation as well as choice of electrodes.

5

Conclusion and recommendations

The most important findings of this work are summarised in the first section. The last section gives recommendations based on these findings.

5.1. Conclusion

The goal of this thesis is to investigate the feasibility of an a-Si:H/a-SiGe:H/nc-Si:H triple junction device to function as power source in a practical water splitting, CO_2 reduction device. As a first step towards this goal, an effort was made to optimise the, within this group, relatively unknown a-SiGe:H subcell. It is found that the electrical performance of the defective a-SiGe:H material is highly dependant on the intrinsic layer thickness and the deposition rate. Thicker intrinsic layers decrease V_{OC} and FF. The J_{SC} was observed to increase up to an intrinsic layer thickness of 160 nm due to more absorption red and infrared light. Increasing the thickness further provides limited increase in infrared response, while blue response deteriorates due to the limited lifetime and mobility of charge carriers in a-SiGe:H. An intrinsic layer thickness of 120 nm is deemed to provide the best combination of reduction of spectral overlap and high V_{OC} and FF for the proposed 3J device. Decreasing the deposition rate results in higher material quality, but has little practical use.

An effort was made to enhance the solar cell external parameters by varying the thickness of the graded parts of the intrinsic layer as well as adding buffer layers. Despite minor improvements on all fronts in an initial experiment that including a 5 nm a-Si:H p/i buffer, no definitive optimal structure was found in a more extensive study. The results of the performed experiments show that, within the scope of this thesis, the reproducibility is insufficient to make definitive conclusions about an ideal configuration of buffer layers and graded layers using the in-house materials and tools. However, it is not expected that the full potential of the a-SiGe:H material has been unlocked, and there is a strong belief that a-Si:H buffer layers at the p/i and/or i/n interface as well as varying the thickness of the graded intrinsic layers can increase the solar cells performance. Further research is required to obtain this configuration and to push the performance a-SiGe:H solar cells, which is essential to improve multi-junction performance based on an a-SiGe:H subcell.

To assess the long term stability of such a 3J device, the a-SiGe:H subcell was submitted to light soaking. The a-SiGe:H material showed large degradation after 1000h of light soaking due to the SW effect. A relative decline in V_{OC} and J_{SC} of approximately 9% was observed, while the largest degradation occurred in the FF, which showed a relative decrease of 20%. This degradation leads to a total relative deterioration in conversion efficiency of -34%.

The best performing p-i-n a-SiGe:H solar cell was processed with an intrinsic layer thickness of 80 nm with V_{OC} =719 mV, J_{SC} =17.2 mA cm^{-2}, FF = 0.63 and η =7.85%. This performance could not be maintained and multi-junction devices were constructed with a-SiGe:H SJ performance of approximately V_{OC} =660 mV, J_{SC} =17.4 mA cm^{-2}, FF = 0.56 and η =6.4% for an intrinsic layer thickness of 120 nm.

Various combinations of layers were processed to find the optimal structure to facilitate tunnelling at the interface of two subcells in two tandem devices. For the top tandem, consisting of an a-Si:H top cell and an a-SiGe:H bottom cell, the best TRJ was found to consist of a thin, 25 nm n-type nc-SiO$_x$:H layer and 5 nm highly doped n$^+$-type nc-SiO$_x$:H with the 2 nm p-type nc-Si:H and 16 nm p-type nc-SiO$_x$:H layers native to the a-SiGe:H subcell. The highly doped n$^+$-type nc-SiO$_x$:H enhances the electric field, which causes electrons to drift near the n/p interface, has low activation energy and provides trap states that facilitate tunnelling. This

TRJ resulted in a V_{OC} = 1.47 V, FF of 0.55, which corresponds to a loss in TRJ of ΔV_{OC}=50 mV, which is on par compared to literature. It should be noted that the p-type nc-Si:H layer appears to be crucial in keeping the FF high in this top tandem device, due to its lower activation energy and thus, better band alignment. The 25 nm n-type nc-SiO_x:H was seen to have the highest light in-coupling in the a-SiGe:H bottom cell. Due to the high spectral overlap between both subcells, the J_{SC} is limited to 7.32 mA cm^{-2}.

The best TRJ for the bottom tandem, consisting of an a-SiGe:H top cell and nc-Si:H bottom cell, was found to be a combination of 25 nm graded n-type nc-SiO_x:H, 25 nm n-type nc-SiO_x:H, 5 nm n^+-type nc-SiO_x:H and 16 nm p-type nc-SiO_x:H. A tandem device with this TRJ achieved a V_{OC} of 1.10 V and a FF of 0.69. Again the loss in V_{OC} due to the TRJ is similar compared to literature with a ΔV_{OC}=56 mV. While the p-type nc-Si:H seems essential to maintain a high FF in the top tandem, in the bottom tandem it appears to cause an adverse effect and diminish FF. This phenomenon is not associated with material growth because of the thick n-layer in the top tandem that can act as a seed layer, but the better current collection due to the thicker n-layers. The 50 nm thick nc-SiO_x:H n-layer of the a-SiGe:H subcell showed to enhance collection for wavelengths of 500-700 nm, while increasing reflection in the 650-700 nm wavelength range at the expense of absorption in the nc-Si:H subcell. Although this caused a larger current mismatch in the bottom tandem device, it gives more margin for the 3J structure, where much of the light for the a-SiGe:H subcell is filtered by the a-Si:H subcell. The J_{SC} of this structure is 9.96 mA cm^{-2}, which is limited by the nc-Si:H bottom cell.

An a-Si:H/a-SiGe:H/nc-Si:H 3J device was fabricated using the results from the tandem experiments. The TRJ structure between middle and bottom subcells showed several difficulties during processing. Therefore the structure without the thin, highly doped n-layer was adopted. The intrinsic layer thicknesses of all subcells was varied in attempt to provide adequate current matching. The a-SiGe:H subcell is current limiting as it receives a filtered spectrum and does not have the benefit of a back reflector. It was found that respective intrinsic layer thicknesses of 175 nm, 120 nm and 3000 nm for the a-Si:H, a-SiGe:H and nc-Si:H subcells obtained the best current match and therefore the highest conversion efficiency. This cell achieved V_{OC} =1.96 V, J_{SC}=6.21 mA cm^{-2}, FF=0.63 and η =7.63%. The generated current density for the individual cells in this 3J device is 8.18 mA cm^{-2}, 5.88 mA cm^{-2} and 8.46 mA cm^{-2} for the top, middle and bottom cells, respectively.

In an effort to decrease the mismatch in generated current between the subcells, the a-SiGe:H n-layer was increased in thickness and a nc-Si:H p-layer was introduced between the middle and bottom cell. This last structure was deposited on both an AZO and Asahi superstrate. Increase in the n-layer thickness decreased reflection in a wavelength range of 800-950 nm, where the absorption of the nc-Si:H subcell is high, towards higher wavelengths, 950-1200 nm where the cell absorbs less. However, these wavelength ranges too high for the a-SiGe:H subcell to absorb.

The rough texture of the Asahi superstrate scatters light very efficiently, enhancing the generated current in the top- and middle subcells, which increased J_{SC} with respect to that of similar structures on the AZO superstrate. It also shows diminished V_{OC} and FF due to defective filaments in the nc-Si:H layer caused by the small roughness of the texture.

The best 3J device is expected to obtain an η_{STF} of 4.88% for a water splitting reaction with an Pt or NiMo electrode and an IrO_x counter electrode, while accounting for ohmic losses. The η_{STF} for a CO_2 reduction reaction strongly depends on the used electrodes and the pH of the environment in which the reaction takes place. Various carbon-based species may be produced in a CO_2 reduction reaction which require different operating voltage due to the difference of electrochemical potential. When assuming similar operation conditions as in the water splitting reaction, an η_{STF} of 2.4% should be possible for producing both hydrogen and methane. Producing carbon species with higher electrochemical potential with the performance as reported in this work seems impossible as the operating voltage exceeds the device V_{OC}.

Using the results of the light-soaking experiment, an estimation of stable η_{STF} for the 3J device can be given. It is determined that η_{STF}=3.86% for a hydrogen producing reaction after 1000h of light soaking could be achieved, which corresponds to a relative decline of 21%.

5.2. Recommendations

The a-SiGe:H subcell is the current limiting subcell of the 3J device. Improving the material quality of the a-SiGe:H along with tuned thicknesses for buffer layers and graded layers should be able to increase the SJ J_{SC} by at least 2 mA cm^{-2} to match reported valued of current generation by other studies using a-SiGe:H with the same bandgap [39]. It is believed that a decreasing the RF power density, increasing operating pressure and varying the hydrogen dilution ratio, while maintaining and optical bandgap of approxomately 1.4 eV can provide the required quality to fabricate high-perfomance 3J devices. Improving material quality not only

enhances overall J_{SC} but will also allow the a-SiGe:H subcell to be made thicker without compromising V_{OC} and FF. Intrinsic layer thickness of at least 200 nm should be possible for the a-SiGe:H subcell, which can reduce spectral overlap with the a-Si:H top cell, increase the current match in 3J device and thus, enhance its conversion efficiency and potential η_{STF}.

Intermediate reflective layers between the middle and bottom cell have high potential to enhance light in-coupling in the middle cell. Increasing the oxygen content in n-type nc-SiO_x:H increases its bandgap and lowers its refractive index. A distributed Bragg reflector uses multiple layers with tweaked refractive index and thickness to create constructive interference of light of a certain wavelength and enhance reflection with each successive layer. Parasitic absorption is not likely to pose a problem in the middle/bottom subcell interface as the top and middle cell will have asorbed the photons larger than the nc-SiO_x:H bandgap.

Enhancing reflection at the interface of the middle and bottom subcell decreases the light in-coupling in the bottom cell. At 3 μm, the current generated by the nc-Si:H was observed to approximately match that of the top cell with approximately J_{SC}=8.5 mA cm^{-2}, which provides sufficient margin to increase light in-coupling in the middle cell at the expense of the bottom cell. If the bottom cell does becomes current limiting due to very effective intermediate reflective layers, the thickness of the nc-Si:H can further increase to 3.5 μm on untextured surfaces without compromising electrical performance [47], and can likely be further increased to 4 μm on an AZO superstrate because of the surface texture.

Is is further suggested that re-calibrating the a-Si:H SJ will increase its V_{OC}, and that of the 3J by up to 150 mV. The EQE is also expected to achieve >0.8 at its maximum value. This will allow the a-Si:H subcell to be made thinner which can enhance FF.

Electrically, the TRJs may be improved by incorporating p^+-doped layers to further enhance the band alignment, increase the drift of charge carriers towards the p/n interface and to provide more trap states that enhance tunnelling by the dopant induced defects. When using p^+-type films, it is important that low activation energy is not hampered by detrimental film growth by the large boron concentration. To provide both good tunnelling and transparency, it is important for the p-type nc-SiO_x:H to have a high optical bandgap and low activation energy. Lower activation energy also reduces energy barriers that form with the adjacent intrinsic layer. This also holds true for an adjacent p-type nc-Si:H layer, if there is any.

It is found that 3J devices provide a good starting point for the conversion of solar- to chemical energy. But to have flexibility in the variety of potentially produced species in a CO_2 reduction device, the solar cell needs to attain higher voltage. For monolithic devices this is achieved by increasing the number of junctions. An a-SiO_x:H cell can be added as new top cell to enhance V_{OC} by more than 1 V. If stability is favoured, the triple junction structure can be processed on a SHJ cell. This can enhance V_{OC} by more than 0.6 V and will provide more stability than the a-SiO_x:H subcell and has already proven its worth with high performance V_{OC}=2.8 V and J_{SC}=6.2 mA cm^{-2} for an a-Si:H/a-Si:H/nc-Si:H/c-Si 4J stack [72]. Due to the high light absorption at long wavelengths, the additional SHJ subcell is likely to pose less problematic in current matching than an a-SiO_x:H subcell as this will have to compete with the spectral response of the a-Si:H and a-SiGe:H subcells. An alternative without a-SiGe:H is an a-SiO_x:H/a-Si:H/nc-Si:H/nc-Si:H cell that already achieved an impressive V_{OC} of 2.82 V and a J_{SC} =5.49 mA cm^{-2} with FF = 0.74[69]. Lastly, nc-SiGe:H is expected, like nc-Si:H, to show low LID and can have a tuneable bandgap between 0.67-1.11 eV [69]. This junction will have the potential to add to the V_{OC}, while not having to compete over light absorption with other subcells. Adding junctions should be done with consideration. Further complicating the structure of a device can cause more losses than gains if done improperly.

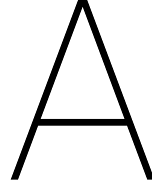

P-type window layer

In the standard single-junction structure, a 2 nm thin nc-Si:H p-layer is used as ohmic contact with the TCO and as seed for crystal growth of the thicker, 16 nm nc-SiO$_x$:H p-layer. High a-SiGe:H SJ performance was achieved by incorporating a dual silicon carbide (SiC) layer with high and and low bandgap of 1.97 eV and 1.91 eV, respectively [39]. The step in bandgap enhances the collection of holes because the energy barrier between the i a-SiGe:H material and the p-layer decreases. This method is expected to show similar results for a double p-layer nc-SiO$_x$:H with high and low bandgap. Moreover, in nc-SiO$_x$:H the higher bandgap is achieved by increasing the oxygen content and as consequence, decreases the refractive index, thus reducing reflection.

Four different combination of dual p-layer structures were fabricated using a thick 200 nm a-SiGe:H intrinsic layer and the standard, half-graded 50 nm nc-SiO$_x$:H n-layer, which are presented in A.1 along with their respective performance.

TableA.1: The external parameters of an a-SiGe:H single-junction solar cell with different configuration of double p-layer. The top p-layer makes contact with the TCO and is kept at 4 nm thickness. The bottom p-layer is adjacent to the intrinsic layer and kept at 8 nm thickness. The letter in brackets denotes high (H) or low (L) bandgap

Name	Top p-layer	Bottom p-layer	V_{OC} (mV)	J_{SC} (mA cm^{-2})	FF (-)	η (%)
Ref	nc-Si:H	nc-SiO$_x$:H (H)	657	17.35	0.50	5.73
H/L	nc-SiO$_x$:H (H)	nc-SiO$_x$:H (L)	636	18.75	0.40	4.78
L/H	nc-SiO$_x$:H (L)	nc-SiO$_x$:H (H)	660	12.29	0.48	3.89
Rev	nc-SiO$_x$:H (H)	nc-Si:H	633	16.78	0.48	5.11

The J_{SC} of the H/L structure shows an improvement with respect to the reference. This might partially be explained by the increase in thickness of the p-type nc-Si:H layer. The 2 nm layer was increased to 4 nm and the nc-SiO$_x$:H was reduced from 16 nm to 8 nm to match the structures as proposed by [39]. It does, however, lose in V_{OC} and FF which keeps the efficiency low. All values for FF are lower than the reference. It is suspected that this is due to the lack of crystallinity in the nc-SiO$_x$:H layers. It is observed for nc-SiO$_x$:H to grow 20 nm before reaching the nanocrystalline phase [67]. Lack of crystallinity throttles the transverse conductivity of the material, resulting in high activation energy and high series resistance. The L/H structure shows a drastic decrease of J_{SC} with respect to the H/L structure. This is not in correspondence with the $J-V$ sweeps of all the dots, which showed an increase in J_{SC} for most dots. The presented J_{SC} values are determined by EQE and several dots were measured and unable to reproduce the values for $J-V$. This seems like a measurement fluke rather than a serious, but the difference is impossible to tell without further testing. The Rev sample has a 4 nm nc-SiO$_x$:H layer and a thicker 8 nm nc-Si:H layer. This cell has diminished performance in all respects due to parasitic absorption and a lack of seed layer for the nc-SiO$_x$:H layer. figure A.1 shows the EQE's of the samples with their corresponding 1-R graph.

The reflectance graph shows near identical reflection, and thus absorption for wavelengths up to 600 nm. A slight increase in blue response is observed for H/L and Rev. This is mainly due to refractive index grading. The origin of variation in EQE is therefore mostly electrical by nature. The H/L sample does provide the best

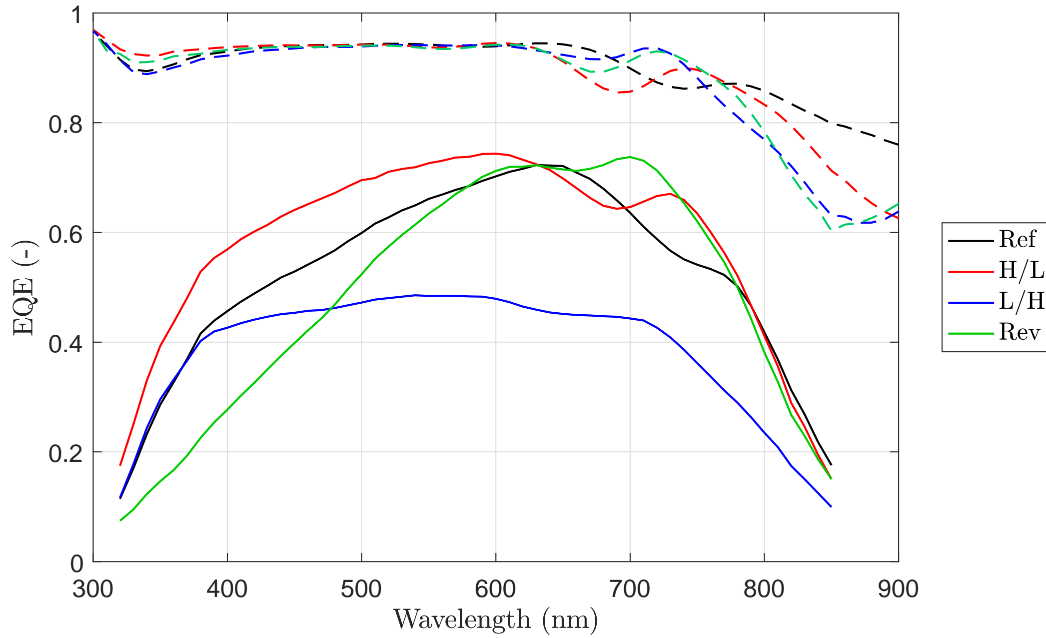

FigureA.1: The EQE of four different p-layer structures along with their respective 1-R

charge collection overall. The lack of crystallinity does not seem very detrimental to the charge collection of H/L sample, while the Ref sample likely suffers from parasitic absorption in the nc-Si:H layer which is surpassed by the Rev sample, which has both high parasitic absorption and a low crystalline fraction of the nc-SiO$_x$:H material.

The a-SiGe:H cell structure is optimized for an approximately 18 nm thick p-layer. All presented samples have only 12 nm, which could hamper the electric field and therefore, charge collection. Nonetheless, it is evident that there is a possible gain to be made in blue response. This has yet to be tested for a-Si:H subcells in multi-junction structures. For now, the tradeoff in blue response versus electrical performance is beneficial for cell performance. The precise quantity of parasitic absorption in the thin nc-Si:H p-layer has also yet to be determined. One suggestion is to experiment with the current structure by combining a thin p-type nc-Si:H layer with the double, H/L, nc-SiO$_x$:H p-layer with thicknesses of 2 nm, 4 nm and 12 nm, respectively. An additional experiment could have linear decreasing oxygen content to provide a better refractive index grading and charge collection.

Bibliography

[1] BP. BP Statistical Review of World Energy June 2017. Technical Report 66, BP, June 2017.

[2] United Nations. PARIS AGREEMENT. Treaty, December 2015.

[3] Valentin Muenzel, I Mareels, Julian de Hoog, Arun Vishwanath, Shivkumar Kalyanaraman, and Andrew Gort. Pv generation and demand mismatch: Evaluating the potential of residential storage. In *Innovative Smart Grid Technologies Conference (ISGT), 2015 IEEE Power & Energy Society*, pages 1–5. IEEE, 2015.

[4] Peter Kareiva, Sean Watts, Robert McDonald, and Tim Boucher. Domesticated Nature: Shaping Landscapes and Ecosystems for Human Welfare. *Science*, 316(5833):1866, June 2007.

[5] Holly P. Jones and Oswald J. Schmitz. Rapid Recovery of Damaged Ecosystems. *PLoS ONE*, 4(5):e5653, May 2009.

[6] Jonathan A. Foley, Ruth DeFries, Gregory P. Asner, Carol Barford, Gordon Bonan, Stephen R. Carpenter, F. Stuart Chapin, Michael T. Coe, Gretchen C. Daily, Holly K. Gibbs, Joseph H. Helkowski, Tracey Holloway, Erica A. Howard, Christopher J. Kucharik, Chad Monfreda, Jonathan A. Patz, I. Colin Prentice, Navin Ramankutty, and Peter K. Snyder. Global Consequences of Land Use. *Science*, 309(5734):570–574, 2005.

[7] Nicholas Stern. The economics of climate change. *The American Economic Review*, 98(2):1–37, 2008.

[8] Saurabh Mahapatra. Lowest-Ever Solar Price Bid (2.42¢/kWh) Dropped In Abu Dhabi By JinkoSolar & Marubeni Score, September 2016.

[9] U.S. Energy Information Administration U.S. Energy Information Adminis. Annual Energy Outlook 2017. Technical report, January 2017.

[10] A. Zuttel, A. Remhof, A. Borgschulte, and O. Friedrichs. Hydrogen: the future energy carrier. *Philosophical Transactions of the Royal Society A: Mathematical, Physical and Engineering Sciences*, 368(1923):3329–3342, July 2010.

[11] Dawn Santoianni. BU-808b: What Causes Li-ion to Die? Battery University.

[12] J. A. Turner. Sustainable Hydrogen Production. *Science*, 305(5686):972–974, August 2004.

[13] Bert Metz and Intergovernmental Panel on Climate Change, editors. *IPCC special report on carbon dioxide capture and storage*. Cambridge University Press, for the Intergovernmental Panel on Climate Change, Cambridge, 2005. OCLC: ocm64949778.

[14] Hairen Tan, Etienne Moulin, Fai Tong Si, Jan-Willem Schüttauf, Michael Stuckelberger, Olindo Isabella, Franz-Josef Haug, Christophe Ballif, Miro Zeman, and Arno H. M. Smets. Highly transparent modulated surface textured front electrodes for high-efficiency multijunction thin-film silicon solar cells: Highly transparent MST front electrodes for multijunction TF-Si solar cells. *Progress in Photovoltaics: Research and Applications*, 23(8):949–963, August 2015.

[15] A Smets. Solar energy; solar solutions presentation, 2016.

[16] Peter Würfel. *Wiley: Physics of Solar Cells: From Basic Principles to Advanced Concepts, 2nd Edition - Peter Würfel*.

[17] Solar Spectral Irradiance: Air Mass 1.5.

[18] A. Smets, K. Jäger, O. Isabella, M. Zeman, and R. van Swaaij. *Solar Energy: The Physics and Engineering of Photovoltaic Conversion, Technologies and Systems*. UIT Cambridge, 2016.

[19] Kunta Yoshikawa, Hayato Kawasaki, Wataru Yoshida, Toru Irie, Katsunori Konishi, Kunihiro Nakano, Toshihiko Uto, Daisuke Adachi, Masanori Kanematsu, Hisashi Uzu, and Kenji Yamamoto. Silicon heterojunction solar cell with interdigitated back contacts for a photoconversion efficiency over 26%. *Nature Energy*, 2:17032, March 2017.

[20] Armin Richter, Martin Hermle, and Stefan Glunz. Reassessment of the Limiting Efficiency for Crystalline Silicon Solar Cells. *IEEE Journal of Photovoltaics*, 3:1184–1191, 2013.

[21] Brandi Casey. Crystalline vs Thin Film Solar Panels.

[22] Martin A. Green, Yoshihiro Hishikawa, Wilhelm Warta, Ewan D. Dunlop, Dean H. Levi, Jochen Hohl-Ebinger, and Anita W.H. Ho-Baillie. Solar cell efficiency tables (version 50). *Progress in Photovoltaics: Research and Applications*, 25(7):668–676, July 2017.

[23] L Houben. Plasmaabscheidung von mikrokristallinem Silizium: Merkmale der Mikrostruktur und deren Deutung im Sinne von Wachstumsvorgängen. (3735), 2000.

[24] New world record for solar cell efficiency at 46% - Fraunhofer ISE, 2014.

[25] Ihsanul Afdi Yunaz, Akira Yamada, and Makoto Konagai. Theoretical Analysis of Amorphous Silicon Alloy Based Triple Junction Solar Cells. *Japanese Journal of Applied Physics*, 46(No. 47):L1152–L1154, November 2007.

[26] Fai Tong Si, Olindo Isabella, and Miro Zeman. Thin-film amorphous silicon germanium solar cells with p- and n-type hydrogenated silicon oxide layers. *Solar Energy Materials and Solar Cells*, 163:9–14, April 2017.

[27] Do Yun Kim, Erwin Guijt, Fai Tong Si, Rudi Santbergen, Jakub Holovský, Olindo Isabella, René A.C.M.M. van Swaaij, and Miro Zeman. Fabrication of double- and triple-junction solar cells with hydrogenated amorphous silicon oxide (a-SiOx:H) top cell. *Solar Energy Materials and Solar Cells*, 141:148–153, October 2015.

[28] Andres Cuevas. The Recombination Parameter J0. *Energy Procedia*, 55:53 – 62, January 2014.

[29] Bofei Liu, Lisha Bai, Xiaodan Zhang, Changchun Wei, Qian Huang, Jian Sun, Huizhi Ren, Guofu Hou, and Ying Zhao. Fill factor improvement in PIN type hydrogenated amorphous silicon germanium thin film solar cells: Omnipotent N type c-SiOx:H layer. *Solar Energy Materials and Solar Cells*, 140:450–456, September 2015.

[30] Omid Shekoofa and Jian Wang. Multi-diode modeling of multi-junction solar cells. pages 1164–1168. IEEE, May 2015.

[31] Optoelectronics Labratory - Iran University of Science & Technology - Nanoptronics Research Center.

[32] D. L. Staebler and C. R. Wronski. Reversible conductivity changes in discharge-produced amorphous Si. *Applied Physics Letters*, 31:292–294, August 1977.

[33] Howard M. Branz. Hydrogen collision model: Quantitative description of metastability in amorphous silicon. *Phys. Rev. B*, 59:5498–5512, Feb 1999.

[34] Andrzej Kolodziej. Staebler-Wronski effect in amorphous silicon and its alloys. *Opto-electronics Review*, 12:21–32, 2004.

[35] Subhendu Guha, Jeffrey Yang, Arindam Banerjee, Baojie Yan, and Kenneth Lord. High quality amorphous silicon materials and cells grown with hydrogen dilution. *Solar Energy Materials and Solar Cells*, 78(1-4):329–347, July 2003.

[36] X. Xu, J. Yang, and S. Guha. On the lack of correlation between film properties and solar cell performance of amorphous silicongermanium alloys. *Applied Physics Letters*, 62(12):1399–1401, March 1993.

[37] J. Meier, R. Flückiger, H. Keppner, and A. Shah. Complete microcrystalline pin solar cellcrystalline or amorphous cell behavior? *Applied Physics Letters*, 65(7):860–862, 1994.

[38] J. Yang, A. Banerjee, and S. Guha. Triple-junction amorphous silicon alloy solar cell with 14.6% initial and 13.0% stable conversion efficiencies. *Applied Physics Letters*, 70(22):2975–2977, 1997.

[39] Soohyun Kim, Jin-Won Chung, Hyun Lee, Jinhee Park, Younho Heo, and Heon-Min Lee. Remarkable progress in thin-film silicon solar cells using high-efficiency triple-junction technology. *Solar Energy Materials and Solar Cells*, 119(Supplement C):26 – 35, 2013.

[40] Maria Jitaru. *Electrochemical carbon dioxide reduction - Fundamental and applied topics*, volume 42. January 2007.

[41] Xiaoxia Chang, Tuo Wang, Peng Zhang, Yijia Wei, Jiubing Zhao, and Jinlong Gong. Stable Aqueous Photoelectrochemical CO2 Reduction by a Cu2o Dark Cathode with Improved Selectivity for Carbonaceous Products. *Angewandte Chemie International Edition*, 55(31):8840–8845, July 2016.

[42] S. Licht, B. Wang, S. Mukerji, T. Soga, M. Umeno, and H. Tributsch. Efficient Solar Water Splitting, Exemplified by RuO2-Catalyzed AlGaAs/Si Photoelectrolysis. *The Journal of Physical Chemistry B*, 104(38):8920–8924, 2000.

[43] Jan-Willem Schüttauf, Miguel A. Modestino, Enrico Chinello, David Lambelet, Antonio Delfino, Didier Dominé, Antonin Faes, Matthieu Despeisse, Julien Bailat, Demetri Psaltis, Christophe Moser, and Christophe Ballif. Solar-to-Hydrogen Production at 14.2% Efficiency with Silicon Photovoltaics and Earth-Abundant Electrocatalysts. *Journal of The Electrochemical Society*, 163(10):F1177–F1181, January 2016.

[44] Marcel Schreier, Florent Héroguel, Ludmilla Steier, Shahzada Ahmad, Jeremy S. Luterbacher, Matthew T. Mayer, Jingshan Luo, and Michael Grätzel. Solar conversion of CO2 to CO using Earth-abundant electrocatalysts prepared by atomic layer modification of CuO. *Nature Energy*, 2:17087, June 2017.

[45] Gurudayal, James Bullock, David F. Sranko, Clarissa M. Towle, Yanwei Lum, Mark Hettick, M. C. Scott, Ali Javey, and Joel Ager. Efficient solar-driven electrochemical CO2 reduction to hydrocarbons and oxygenates. *Energy Environ. Sci.*, 10(10):2222–2230, 2017.

[46] M Falkenberg. A multi junction solar cell for water splitting development of an a-si:h/nc-si:h/shj triple junction solar cell, 2016.

[47] M Stam. Improving a silicon based triple junction cell for solar water splitting, 2017.

[48] H Tan. *Materials and Light Management for High-Efficiency Thin-Film Silicon Solar Cells.* 2015. OCLC: 6893878764.

[49] D Kim, E Guijt, RACMM van Swaaij, and M Zeman. Development of a-siox:h solar cells with very high vocŒff product. *Progress in Photovoltaics: research and applications*, 23(6):671–684, 2015. Harvest Published online 3-12-2014.

[50] Guangtao Yang, René A. C. M. M. van Swaaij, Olindo Isabella, and Miro Zeman. A novel way of texturing glass for microcrystalline silicon thin film solar cells application: Texturing glass for microcrystalline silicon thin film solar cells. *Progress in Photovoltaics: Research and Applications*, 23(10):1283–1290, October 2015.

[51] P Babal. *Doped nanocrystalline silicon oxide for use as (intermediate) reflecting layers in thin-film silicon solar cells.* 2014. OCLC: 6893918753.

[52] G Papakonstantinou. Investigation and optimization of the front metal contact of silicon heterojunction solar cells, 2014.

[53] Aditya Chaudhary. Development of four-terminal mechanically-stacked solar cells utilising hydrogenated amorphous silicon oxide (a-siox:h) and crystalline silicon cells, 2017.

[54] Yoo Jin Lee, Jin Koog Shin, and Koeng Su Lim. Thin Film Silicon Solar Cells on ZnO/SnO. volume 1, pages 11–14. ECS, 2006.

[55] Qi Hua Fan, Changyong Chen, Xianbo Liao, Xianbi Xiang, Shibin Zhang, William Ingler, Nirupama Adiga, Zhihua Hu, Xinmin Cao, Wenhui Du, and Xunming Deng. High efficiency silicongermanium thin film solar cells using graded absorber layer. *Solar Energy Materials and Solar Cells*, 94:1300–1302, July 2010.

[56] S. Guha, X. Xu, J. Yang, and A. Banerjee. High deposition rate amorphous siliconbased multijunction solar cell. *Applied Physics Letters*, 66(5):595–597, January 1995.

[57] JL Andújar, E Bertran, A Canillas, C Roch, and JL Morenza. Influence of pressure and radio frequency power on deposition rate and structural properties of hydrogenated amorphous silicon thin films prepared by plasma deposition. *Journal of Vacuum Science & Technology A: Vacuum, Surfaces, and Films*, 9(4):2216–2221, 1991.

[58] Duy Phong Pham, Sangho Kim, Jinjoo Park, Anh Huy Tuan Le, Jaehyun Cho, and Junsin Yi. Improvement in carrier collection at the i/n interface of graded narrow-gap hydrogenated amorphous silicon germanium solar cells. *Journal of Alloys and Compounds*, 724:400–405, November 2017.

[59] R.A.C.M.M. van Swaaij, M. Zeman, S. Arnoult, and J.W. Metselaar. Performance dependence on grading width of a-SiGe:H component solar cells. pages 869–872. IEEE, 2000.

[60] D Lundszien, F Finger, and H Wagner. A-si: H buffer in a-sige: H solar cells. *Solar energy materials and solar cells*, 74(1):365–372, 2002.

[61] Jan-Willem Schüttauf, Bjoern Niesen, Linus Löfgren, Maximilien Bonnet-Eymard, Michael Stuckelberger, Simon Hänni, Mathieu Boccard, Grégory Bugnon, Matthieu Despeisse, Franz-Josef Haug, Fanny Meillaud, and Christophe Ballif. Amorphous silicongermanium for triple and quadruple junction thin-film silicon based solar cells. *Solar Energy Materials and Solar Cells*, 133:163–169, February 2015.

[62] Taweewat Krajangsang, Sorapong Inthisang, Adrien Dousse, Apichan Moollakorn, Aswin Hongsingthong, Songkiate Kittisontirak, Perawut Chinnavornrungsee, Amornrat Limmanee, Jaran Sritharathikhun, and Kobsak Sriprapha. Band gap profiles of intrinsic amorphous silicon germanium films and their application to amorphous silicon germanium heterojunction solar cells. *Optical Materials*, 51:245–249, January 2016.

[63] M. Stutzmann, W. B. Jackson, and C. C. Tsai. Light-induced metastable defects in hydrogenated amorphous silicon: A systematic study. *Phys. Rev. B*, 32:23–47, Jul 1985.

[64] Baojie Yan, Guozhen Yue, Laura Sivec, Jeffrey Yang, Subhendu Guha, and Chun-Sheng Jiang. Innovative dual function nc-SiOx:H layer leading to a >16% efficient multi-junction thin-film silicon solar cell. *Applied Physics Letters - APPL PHYS LETT*, 99, 2011.

[65] Hairen Tan, Pavel Babal, Miro Zeman, and Arno H. M. Smets. Wide bandgap p-type nanocrystalline silicon oxide as window layer for high performance thin-film silicon multi-junction solar cells. *Solar Energy Materials and Solar Cells*, 132(Supplement C):597–605, January 2015.

[66] Guangtao Yang, René A. C. M. M. van Swaaij, Olindo Isabella, and Miro Zeman. A novel way of texturing glass for microcrystalline silicon thin film solar cells application. *Progress in Photovoltaics: Research and Applications*, 23(10):1283–1290, 2015. PIP-14-067.R1.

[67] Andrea Tomasi, Bertrand Paviet-Salomon, Quentin Jeangros, Jan Haschke, Gabriel Christmann, Loris Barraud, Antoine Descoeudres, Johannes Peter Seif, Sylvain Nicolay, Matthieu Despeisse, Stefaan De Wolf, and Christophe Ballif. Simple processing of back-contacted silicon heterojunction solar cells using selective-area crystalline growth. *Nature Energy*, 2:17062, April 2017.

[68] Fai Tong Si, Olindo Isabella, Hairen Tan, and Miro Zeman. Quadruple-Junction Thin-Film Silicon Solar Cells Using Four Different Absorber Materials. *Solar RRL*, 1(3-4):1700036, April 2017.

[69] F.T. Si. Quadruple-Junctions Thin-film Silicon-Based Solar Cells. Technical report, Delft University of Technology, 2017. DOI: 10.4233/uuid:36b80a78-ffd2-4a3d-a6b3-9bbc188b255e.

[70] Meenesh R. Singh, Kimberly Papadantonakis, Chengxiang Xiang, and Nathan S. Lewis. An electrochemical engineering assessment of the operational conditions and constraints for solar-driven water-splitting systems at near-neutral ph. *Energy and Environmental Science*, 8(9):2760–2767, 9 2015.

[71] Charles C. L. McCrory, Suho Jung, Ivonne M. Ferrer, Shawn M. Chatman, Jonas C. Peters, and Thomas F. Jaramillo. Benchmarking Hydrogen Evolving Reaction and Oxygen Evolving Reaction Electrocatalysts for Solar Water Splitting Devices. *Journal of the American Chemical Society*, 137(13):4347–4357, 2015.

[72] Félix Urbain, Vladimir Smirnov, Jan-Philipp Becker, Andreas Lambertz, Florent Yang, Jürgen Ziegler, Bernhard Kaiser, Wolfram Jaegermann, Uwe Rau, and Friedhelm Finger. Multijunction Si photocathodes with tunable photovoltages from 2.0 V to 2.8 V for light induced water splitting. *Energy & Environmental Science*, 9:145–154, 2015.